

**MULTICOLOUR PHOTOMETRIC
MONITORING OF ACTIVE
GEOSTATIONARY SATELLITES:
INVESTIGATING THE EFFECTS OF
THE SPACE ENVIRONMENT**

**SURVEILLANCE PHOTOMÉTRIQUE
MULTI-COULEUR DE SATELLITES
GÉOSTATIONNAIRES: ÉTUDE SUR
LES EFFETS DE L'ENVIRONNEMENT
SPATIAL**

A Thesis Submitted to the Division of Graduate Studies
of the Royal Military College of Canada
by

Jason Shaw, CD, B.Sc.

Lieutenant

In Partial Fulfillment of the Requirements for the Degree of
Master of Science in Physics

April, 2016

© This thesis may be used within the Department of National Defence
but copyright for open publication remains the property of the author.

To my wife Maigan and my son Jacob. Thank you.

Acknowledgements

First, I would like to thank my supervisor Major Don Bédard and co-supervisor Dr. Gregg Wade. Their guidance made it possible to explore a topic that was both challenging and interesting.

Next, I wish to acknowledge the members of the Space Surveillance Research Laboratory at RMCC. Throughout my thesis this group was a constant source of ideas and advice.

I would also like to thank the Department of Mechanical and Aeronautical Engineering at RMCC. It would have been much more difficult, if not impossible, to collect the data for this thesis without the use of their facilities at Point Frederick.

Finally, a debt of gratitude is owed to my wife Maigan. Your enduring support, particularly during the last six years, has made it possible for me to chase my dreams.

Abstract

Shaw, Jason. MSc. Royal Military College of Canada, April 2016. *Multicolour photometric monitoring of active geostationary satellites: Investigating the effects of the space environment*. Supervised by Maj. Donald Bédard and co-supervised by Dr. Gregg A. Wade.

Multicolour broadband photometry has been used extensively to characterize artificial Earth-orbiting satellites, but relatively few studies have been dedicated to measuring the effects of the space environment on the spectral reflectance of satellite materials. The studies that have been undertaken mainly focused on inactive unstabilized satellites which resulted in an unknown, and constantly changing, illumination and observational geometry. As a consequence, it was very difficult to determine which satellite surfaces and materials were reflecting sunlight to the sensor when a measurement was taken. To address this shortcoming, an observational experiment was conducted using active geostationary (GEO) satellites with a fixed attitude, and thus known illumination and observational geometries. The aim of this experiment was to assess whether multicolour broadband photometry could be used to measure the effects of the space environment on the spectral reflectance of these satellites. Multicolour photometric measurements were taken, during 16 nights between late June and late October 2015, of five similar active GEO satellites with different launch dates (Galaxy-3C (2002), Spaceway-1 (2005), Spaceway-3 (2007), DirecTV-10 (2007), and DirecTV-12(2009)). From these measurements, light curves and time-resolved colour indices were generated. The results suggested that older satellites had an increased spectral reflectance at longer wavelengths. This was consistently observed in the R-I colour index. In the process of conducting this experiment, it was found that the light curves of identical GEO satellites shared some similarities, but differed in structure and magnitude. In addition, a modeled specular reflection analysis technique was developed to support the aim of the thesis. These results indicated that it is possible to constrain the physical origin of many of the

observed light curve features. Overall, this work contributes to the field of space situational awareness by expanding the current capabilities of multicolour broadband photometry to measure the effects of the space environment on the spectral reflectance of satellite materials.

Keywords: Multicolour broadband photometry, geostationary satellite, GEO satellite, light curves, colour indices, space situational awareness

Résumé

La photométrie couleur à large bande a été grandement utilisée pour caractériser satellites artificiels en orbite terrestre, mais relativement peu d'études ont été consacrées à la mesure des effets de l'environnement spatial sur la réflectance spectrale des matériaux retrouvées à la surface de satellites. Les études qui ont été entreprises avaient principalement pour objectifs d'étudier des satellites inactifs non-stabilisés ayant pour conséquence que la géométrie d'illumination et d'observation était variable et inconnue. Donc, il n'était pas possible de conclure quelles surfaces des satellites réfléchissaient la lumière solaire au télescope. Afin de contrer ce problème, une expérience observationnelle fut mise sur pied dans laquelle les sujets étaient tous des satellites géostationnaires (GÉO) ayant une orientation stable et donc une géométrie d'illumination et d'observation connue. Le but de cette expérience était de déterminer si la photométrie couleur à large bande pouvait être utilisée pour étudier les effets de l'environnement spatial sur la réflectance spectrale des GÉO qui ont une orientation fixe avec une géométrie d'illumination et d'observation. Lors de 16 nuits entre les mois de juin et octobre 2015, des mesures de photométrie couleur ont été prises de cinq satellites GÉO actifs ayant des plateformes semblables mais qui ont été placés en orbite terrestre à différentes dates (Galaxy-3C (2002), Spaceway-1 (2005), Spaceway-3 (2007), DirecTV-10 (2007), and DirecTV-12(2009)). À partir de ces mesures, des courbes photométriques et des indices de couleurs furent créés. L'analyse de l'indice de couleur R-I indique que les satellites ayant passé le plus de temps en orbite terrestre démontrent une augmentation de leur réflectance spectrale dans les longueurs d'onde plus longue. L'analyse des courbes photométriques a par ailleurs montrée que les satellites GÉO ayant une plateforme semblable ont des signatures photométriques similaires hors avec des différences dans leur structure et intensité. De plus, pour mieux comprendre les résultats, un modèle de la réflexion spéculaire fut élaboré. Ce modèle fut utilisé afin de contraindre l'origine de certains traits observés sur les courbes photométriques. En général, le travail présenté dans ce document contribue au domaine de la

connaissance de la situation spatiale en élargissant le spectre d'information pouvant être recueillie de la photométrie couleur afin de mesurer les effets de l'environnement spatial sur la réflectance spectrale de satellites.

Mots clés: Photométrie couleur, satellite géostationnaire, satellite GÉO, courbe photométrique, indice de couleur, connaissance de la situation spatiale

Contents

Acknowledgements	iii
Abstract	iv
Résumé	vi
List of Tables	xi
List of Acronyms	xv
1 Introduction	1
1.1 Background	1
1.1.1 Geostationary Satellites	3
1.1.2 Illumination and Observational Geometry	6
1.1.3 Principles of Reflectance	8
Reflection Components	8
Bidirectional Reflectance Distribution Function	9
1.1.4 Satellite Characterization using Photometry	12
1.1.5 Space Weathering	14
Atomic Oxygen	14
Plasma	15
Radiation	15
Outgassing and Contamination	16
1.2 Aim of the Masters Thesis	17
1.3 Thesis Outline	17
2 Literature Survey	19
2.1 Measuring Exposure to the Space Environment	19
2.1.1 Summary	24
2.2 Illumination and Observational Geometry	24

2.2.1	Summary	31
2.3	Light Curve Analysis	31
2.3.1	Summary of Light Curve Analysis	37
2.4	Summary of Contribution to this Research	38
3	Experimental Setup and Procedures	39
3.1	Experimental Objectives	39
3.2	Equipment Description	40
3.2.1	Telescope	40
3.2.2	CCD Detector	40
3.3	Experimental Subjects	43
3.4	Data Collection Procedures	47
3.4.1	Daily Planning and Location	47
3.4.2	Bias, Dark, and Flat Field Images	48
3.4.3	Standard Star Exposures	49
3.4.4	Satellite Exposures	50
4	Data Reduction Procedures	52
4.1	Image Pre-Processing	52
4.2	Magnitude Extraction	54
4.3	Photometric Standard Stars	56
4.4	Colour Indices	57
4.5	Error Analysis	59
4.5.1	Instrumental Magnitude Uncertainty	59
4.5.2	Combined Uncertainty	60
5	Seasonal Light Curve Variations and Specular Reflection Analysis	61
5.1	Seasonal Light Curve Variations	62
Spaceway-1 and Spaceway-3: Boeing 702-HP Type A	68
DirecTV-10 and DirecTV-12: Boeing 702-HP Type C	68
Galaxy-3C: Boeing 702-HP Type B	68	
5.2	Specular Reflection Analysis	69
5.2.1	June - August Vector Projection Analysis	74
5.2.2	October Vector Projection Analysis	78
Late June to early August Vector Projection Results	81
Late October Vector Projection Results	84	
5.3	Summary of Seasonal Light Curve and Reflection Vector Analysis	85
6	Colour Index Variations and Analysis	86

6.1	Seasonal Colour Index Variations	87
	Spaceway-1 and Spaceway-3	91
	Galaxy-3C	92
	DirecTV-10 and DirecTV-12	93
6.2	Colour Index Analysis during +Z Body and Solar Array Features	94
	Solar array colour indices	98
	+Z body surface colour indices	98
6.3	Summary of Colour Index Results	100
7	Conclusion	102
7.1	Summary of Conclusions	103
	7.1.1 Seasonal Light Curve Variations of Identical Satellites .	103
	7.1.2 Identification of Specular Reflections	104
	7.1.3 Measuring the Effects of the Space Environment with Broadband Photometry	105
7.2	Recommendations for Future Work	106
	Bibliography	108
	Appendices	111
	A Standard Stars	112
	B Uncertainty	114
	C Curriculum Vitae	116

List of Tables

1.1	Parameters of common orbits.	3
2.1	Colour indices of spacecraft material samples [21].	26
2.2	Observed satellites, bus type, and orbital longitude [8].	33
3.1	Pixel scale and FWHM for increasing pixel binning schemes.	43
3.2	Properties of the observed satellites.	44
4.1	Example exposure and elapsed times.	58
B.1	Average SNR and photometric uncertainty.	114
B.2	Nightly zero points and uncertainty.	115
B.3	Average colour index uncertainties.	115

List of Figures

1.1	Light curves for GEO satellites with uncontrolled and controlled attitudes.	2
1.2	Artist renditions of Geostationary satellites [11].	5
1.3	Simplified diagram of the satellite illumination and observational geometries.	6
1.4	Satellite-centered coordinate system used to describe the position of the Sun and observer.	7
1.5	Azimuth and elevation angles to the Sun and observer within the satellite-centered coordinate system.	7
1.6	Phase angle (α) in the satellite-centered coordinate system.	8
1.7	Illustration of specular, specular-diffuse, and diffuse reflections [12].	9
1.8	Geometry of the BRDF [13].	10
1.9	Lightcurve of an active GEO satellite.	12
1.10	Passbands of the Johnson-Cousins photometric system [15].	13
1.11	Simplified block diagram of multicolour broadband photometry.	14
1.12	Space weathering damage to the Hubble Space Telescope [16].	15
1.13	Pre-flight and post-flight photographs of NASA's Optical Properties Monitor experiment [16].	16
2.1	Diagram of data collection procedures [19].	20
2.2	Spectral BRDF for aluminum and reflective white paint samples, normalized to unity at 550 nm and taken at $\theta_i=\theta_r=30^\circ$ [19].	21
2.3	Z, Y, J, H, and K-band transmittance functions and atmospheric windows in the NIR regime [20].	22
2.4	Mean values of the J-K and H-K colour indices as a function of launch date [20].	23
2.5	Solar corrected photometric B-R vs. B-V colour indices for 14 laboratory material samples [21].	25
2.6	Model of IDSCP satellite [23].	27

2.7	B-V and B-R colour indices for IDCSP satellites and laboratory solar cell samples [23].	28
2.8	Normalized broadband BRDF and colour indices for TJPV solar cell, aluminum mirror, and reflective white paint [24].	30
2.9	Observed magnitude as a function of phase angle for two Canonical class GEO satellites [25].	32
2.10	V-band light curves for Echostar-17 and Anik-G1 [8].	34
2.11	I-band lightcurves for Galaxy-15 in November 2010 [3].	35
2.12	Galaxy-15 faint glint feature as a function of the phase angle bisector in the body and solar array reference frames [3].	37
3.1	Quantum efficiency for the QSI-690ws CCD camera [27].	41
3.2	Illustration of CCD pixel binning schemes.	42
3.3	Galaxy-3C [11].	44
3.4	Spaceway-1 and Spaceway-3 [11].	45
3.5	DirecTV-10 and DirecTV-12 [11].	46
3.6	Experimental setup at RMCC Kingston.	47
3.7	Example of a twilight flat raw image.	50
3.8	Screen capture of the data monitoring script.	51
4.1	Histogram of the master bias image used for data reduction.	53
4.2	Sample dark image.	53
4.3	Master flat image used during data reduction.	54
4.4	Aperture and background sky annulus used for data reduction.	55
4.5	Nightly zero points for all bands.	57
4.6	Raw and interpolated data points for all bands.	59
5.1	Raw images of Group A and Group B satellites.	62
5.2	Seasonal V-band light curves for Spaceway-3.	63
5.3	Seasonal V-band light curves for Spaceway-1.	64
5.4	Seasonal light curves for Galaxy-3C.	65
5.5	Seasonal light curves for DirecTV-10.	66
5.6	Seasonal V-band light curves for DirecTV-12.	67
5.7	Seasonal Sun azimuth and elevation angles.	70
5.8	Surface normal vectors for the Sun-tracking solar arrays and satellite +Z body surface on 8 August 2015.	71
5.9	Solar array and +Z body specular reflection vectors on 8 August 2015.	72
5.10	Diagram of the +Z body surface reflection and vector projection.	73
5.11	Solar array and +Z body surface reflection vectors on 8 August 2015.	74

5.12	Solar panel and +Z body surface vector projections for Spaceway-3 between late June and early August 2015.	75
5.13	Solar panel and +Z body surface vector projections for Spaceway-1 between early July and early August 2015.	76
5.14	Solar panel and +Z body surface vector projections for Galaxy-3C between late June and early August 2015.	77
5.15	Solar array and +Z body surface reflection vectors in October. . .	78
5.16	Solar panel and +Z body surface vector projections for Spaceway-3 and Spaceway-1 in late October 2015.	79
5.17	Solar panel and +Z body surface vector projections for DirecTV-10 and DirecTV-12 in late October 2015.	80
5.18	Solar array and +Z body surface vector projections for Galaxy-3C in late October 2015.	81
5.19	Spaceway-1 and Spaceway-3 main bus structure [11].	82
5.20	Coverage footprints for Spaceway-1 and Spaceway-3 [30].	83
5.21	Galaxy-3C main bus structure [11].	84
6.1	Seasonal colour indices for Spaceway-3. Average colour index uncertainties between 0.015 and 0.098.	87
6.2	Seasonal colour indices for Spaceway-1. Average colour index uncertainties between 0.026 and 0.101.	88
6.3	Seasonal colour indices for Galaxy-3C. Average colour index uncertainties between 0.015 and 0.098.	89
6.4	Colour indices for DirecTV-10 and DirecTV-12 in late October 2015. Average colour index uncertainties between 0.026 and 0.083.	90
6.5	Colour indices +Z body and solar array features.	95
6.6	Spaceway-3, Galaxy-3C, Spaceway-1, DirecTV-10, and DirecTV-12's light curves in late-October with solar array reflections indicated.	96
6.7	Spaceway-3 and Spaceway-1's light curves between late June and early August with +Z body surface reflections indicated.	97
6.8	Mean values of the seasonal R-I colour indices for DirecTV-10, DirecTV-12, Spaceway-3, and Galaxy-3C.	99

List of Acronyms

ADU	analog-to-digital unit
BRDF	bidirectional reflectance distribution function
CCD	charge-coupled device
FOV	field of view
FWHM	full width at half maximum
GEO	geostationary orbit
GTO	geostationary transfer orbit
IDCSP	Initial Defense Communications Satellite Program
IRAF	Image Reduction and Analysis Facility
LEO	low Earth orbit
MEO	medium Earth orbit
MLI	multi-layer insulation
MSM	minutes since midnight
NIR	near-infrared
NOAO	National Optical Astronomy Observatory

PCHIP Piecewise Cubic Hermite Interpolating Polynomial

QE quantum efficiency

RMCC Royal Military College of Canada

RSO resident space object

SED spectral energy distribution

SNR signal-to-noise ratio

SSA space situational awareness

STK Systems Tool Kit

TASAT Time-Domain Analysis and Simulation for Advanced Tracking

TJPV triple-junction photovoltaic

TLE two-line element set

UTC coordinated universal time

UV ultraviolet

1 Introduction

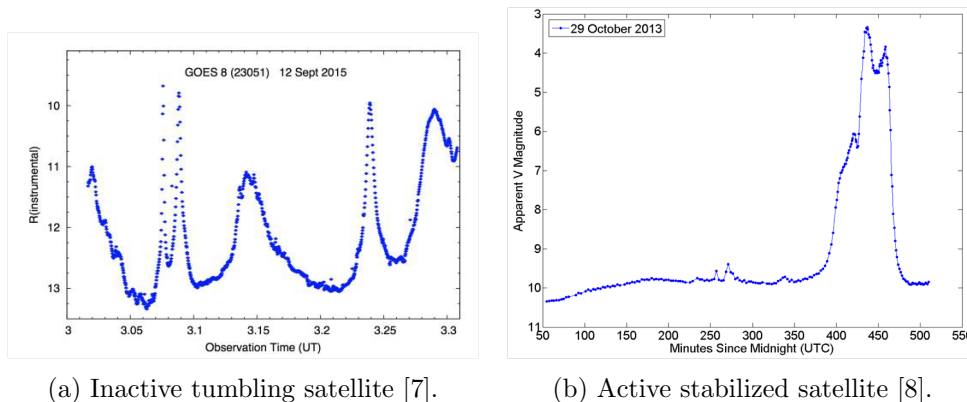
1.1 Background

Space offers a unique vantage point for a variety of military, commercial, and scientific missions. Sensors operating in this environment have the advantage of global coverage, repeating ground tracks, and unrestricted overflight. Due to these advantages, space has been used extensively since the late 1950s which has resulted in more than 17,000 objects being actively tracked by the United States Space Surveillance Network [1]. These objects include active and non-active satellites, spent rocket bodies, and other small debris. Many of the active satellites provide services upon which our modern society depends. Thus, verifying that they are operating nominally is an important component of space mission operations and space situational awareness (SSA).

Monitoring satellite health and operation is typically conducted using telemetry data. However, there are times when this is not possible. In April 2010, the communications satellite Galaxy-15 experienced a failure leaving its operators unable to monitor its health or control its systems by the conventional means of receiving telemetry and uplinking commands [2]. As a result, the satellite began to drift from its assigned orbit causing potential problems to nearby satellites. During this period, ground-based observers used time-resolved photometry to determine that some of the satellite's subsystems were operable [3]. The photometric data indicated that the satellite was maintaining a stable attitude which implied that, as a minimum, the power and attitude control subsystems were operating. Ultimately, communications were re-established and normal operations were resumed. This is an example of the utility of photometry within the context of SSA.

Photometry has been used for many decades in the field of observational astronomy. Its fundamental purpose is to measure the quantity of electromagnetic radiation, known as flux, received from a celestial object [4]. Multicolour broadband photometry measures this flux in several wide wavelength bands. For astronomical purposes, it is used to gain information about an object’s energy output, size, temperature, and other physical properties [5]. Photometry has also been used extensively within the SSA community. Satellite characterization and material identification have been two of the main efforts [3, 6].

Figure 1.1 shows an example of a satellite characterization technique. Both images show the observed brightness as a function of time. These are known as light curves and they are generated from photometric measurements obtained with a telescope and detector. Figure 1.1a shows a light curve from a GEO satellite whose attitude is not controlled. The rapid variations in brightness, in this case, indicate that the satellite’s attitude control or power subsystems may have failed. Figure 1.1b shows a light curve from an active GEO satellite with a controlled attitude. For several hours, no significant variations in its brightness were observed, which is indicative of a stable attitude. The bright peaks are caused when the Sun reflects from the solar panels or other specularly reflecting surfaces.



(a) Inactive tumbling satellite [7].

(b) Active stabilized satellite [8].

Figure 1.1: Light curves for GEO satellites with uncontrolled and controlled attitudes.

Artificial satellites operate in an environment where they are constantly exposed to remnants of the neutral atmosphere, space debris, plasma, and radiation [9]. It is beneficial to understand the effects of the space environment

on satellite materials from both engineering and SSA perspectives. Measuring and quantifying these effects could lead to the design and use of materials better suited for the space environment. More applicable to SSA, the capability to measure and quantify these effects could be used for satellite characterization purposes.

The remainder of this chapter discusses the fundamentals of the topics presented in this thesis. Initially, satellite orbits and hardware configurations are discussed along with the illumination and observational geometries. The fundamentals of reflectance and photometry are then discussed. Finally, the aim and outline of the thesis are presented.

1.1.1 Geostationary Satellites

The term artificial Earth-orbiting satellite, subsequently referred to as satellite, refers to a human-made object that has been placed in space, typically into a predefined orbit, for a specific mission. There are several orbital regimes in which the majority of satellites operate. Table 1.1 shows the parameters of the most common orbits. Low-Earth orbit (LEO) and medium-Earth orbit (MEO) are well suited to remote sensing and navigation missions due to their altitudes. A geosynchronous orbit has a much higher altitude and is commonly used by large communications satellites. A unique geosynchronous orbit, called geostationary (GEO), occurs when the position of a satellite remains fixed when viewed from a point on the surface of the Earth. This means that antennas and other ground-based equipment remain fixed and do not need to actively track the satellite.

Orbit	Altitude	Period
Low-Earth Orbit (LEO)	<3,000 km	<150 min
Medium-Earth Orbit (MEO)	3,000 - 35,786 km	150 - 1436 min
Geostationary Orbit (GEO)	35,786 km	1436 min

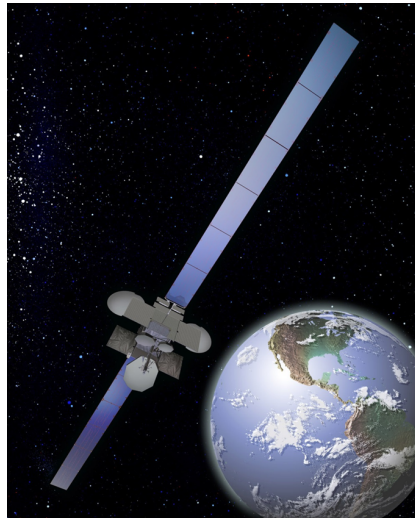
Table 1.1: Parameters of common orbits.

GEO satellites are ideal subjects for ground-based observational experiments for several reasons. As previously mentioned, a GEO satellite's fixed position means that a telescope does not need to actively track the satellite

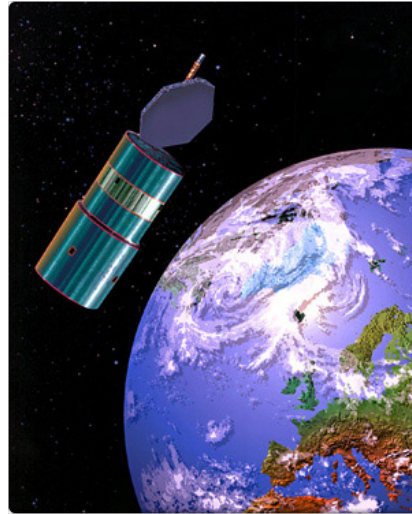
during a night of observations. This greatly simplifies equipment requirements and procedures. Secondly, active GEO satellites maintain a stable and known attitude which results in a predictable illumination and observational geometry. Finally, GEO satellites have a repeating illumination geometry which is caused by the seasonal changes in the Sun's position. The predictable and repeatable illumination and observational geometry makes it possible to compare experimental data collected over multiple years from different locations.

The mission, and high altitude, of GEO satellites usually results in a large payload with demanding power requirements. The power subsystem is typically comprised of large solar arrays. They are attached to a central structure, known as the satellite bus, which houses the primary payload and all supporting subsystems. Most modern GEO satellites are built using a variant of a pre-existing satellite bus that has been customized for that specific mission.

GEO satellites are constructed from many different materials. Solar arrays are commonly triple-junction photovoltaic cells (TJPV cells) constructed from a compound such as Gallium-Arsenide [10]. The bus structure is wrapped in a polyimide-based thermal insulation, known as multi-layer insulation (MLI). While many of the bus's external coatings and surfaces perform thermal control functions, there are also external elements of the payload. These elements consist of mission-dependent antennas and sensors. Figure 1.2 shows an artist's conception of four different GEO satellites to illustrate the different designs and possible configurations.



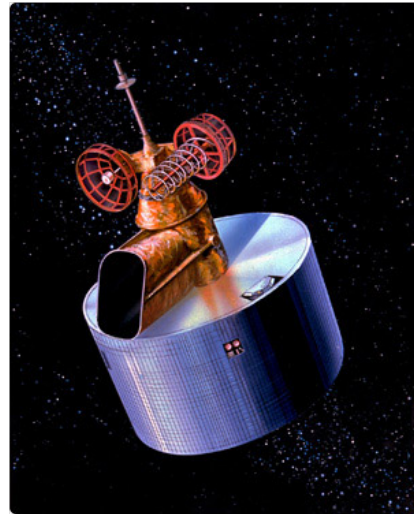
(a) Galaxy-3C (2002).



(b) Astra-2D (1989).



(c) TDRS-H (2000).



(d) GMS-1 (1977).

Figure 1.2: Artist renditions of Geostationary satellites [11].

Figure 1.2a shows a variant of the popular Boeing 702-HP bus, known as a box-wing configuration. Figure 1.2b shows the Boeing 736 bus. Power is generated from the solar cells that cover the cylindrical-shaped body. This bus was popular in the 1970s and 1980s but increasing power demands rendered it obsolete. Figures 1.2c and 1.2d show additional GEO satellite buses that illustrate the diversity of bus and payload configurations.

1.1.2 Illumination and Observational Geometry

Much of the discussion in this thesis will be dedicated to the analysis of illumination and observational geometry. As such, a definition of all elements of this geometry is necessary. Figure 1.3 shows the simplified satellite illumination and observational geometry. The position of a GEO satellite remains fixed relative to an Earth-based observer. The nightly and seasonal changes in the Sun's position result in a constantly changing satellite illumination geometry. The angle between the Sun and observer, as measured at the satellite, is known as the phase angle (α). It will be discussed in further detail in this section.

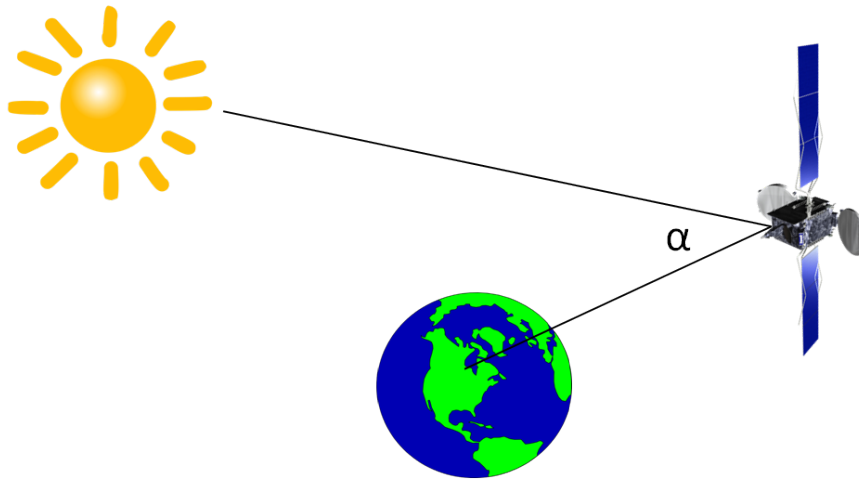


Figure 1.3: Simplified diagram of the satellite illumination and observational geometries.

A satellite-centered coordinate system will be used to describe the position of the Sun and observer. This type of system, which is commonly used in the SSA field, allows for an easy interpretation of the illumination and observational geometry. Figure 1.4 shows the fundamental plane and principal axes of the satellite-centered coordinate system. The +X is in the direction of the satellite's velocity, +Z points to the center of the Earth, and +Y completes the right-handed coordinate system. The Sun, Earth, and position vectors are also shown for reference.

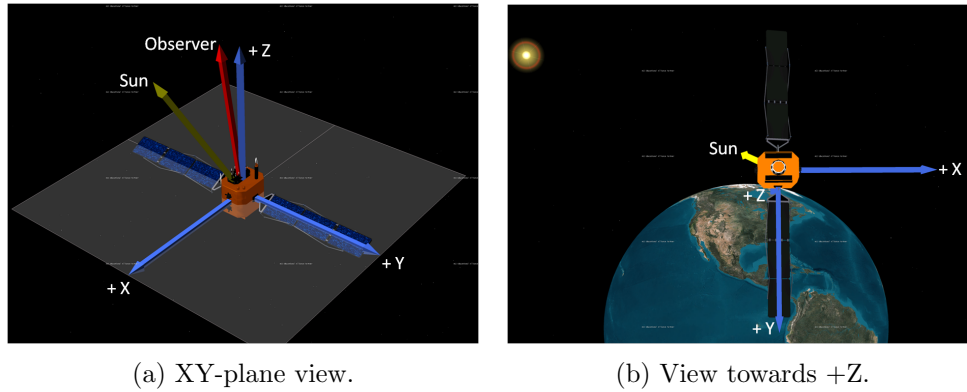


Figure 1.4: Satellite-centered coordinate system used to describe the position of the Sun and observer.

Spherical coordinates are used to describe the position of the Sun and observer relative to the satellite. Figure 1.5 shows the four angles used to describe the position of the Sun and observer. The Sun and observer azimuth angles (θ_{sun} and θ_{obs}) are measured from the +X direction while the Sun and observer elevation angles (ϕ_{sun} and ϕ_{obs}) are measured from the +Z direction. The elevation angles have positive values in the spring and summer and negative values in the fall and winter. For a GEO satellite, θ_{obs} and ϕ_{obs} remain fixed and θ_{sun} and ϕ_{sun} vary.

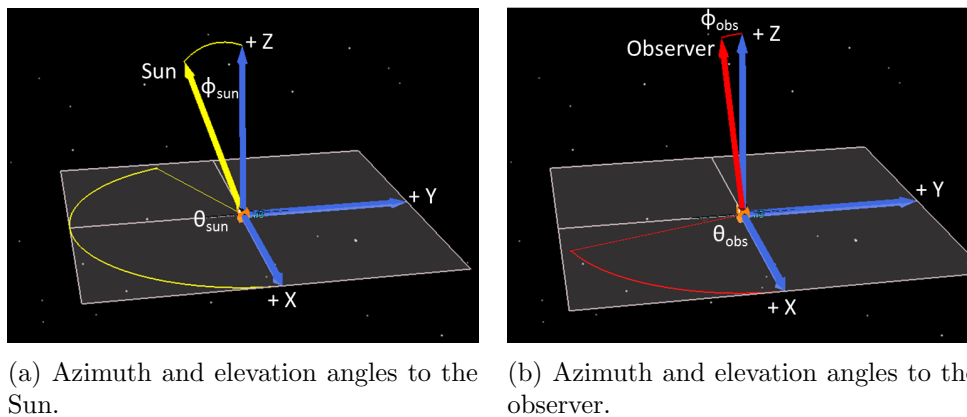


Figure 1.5: Azimuth and elevation angles to the Sun and observer within the satellite-centered coordinate system.

Although the phase angle measures the angular displacement between two position vectors, it can also be signed to indicate the Sun's position. The phase angle is negative when $0^\circ < \theta_{sun} \leq 90^\circ$ and positive when $90^\circ < \theta_{sun} \leq 180^\circ$. Essentially, during the beginning of the night the phase angle is negative. When the Sun crosses the satellite's YZ-plane the phase angle becomes positive.

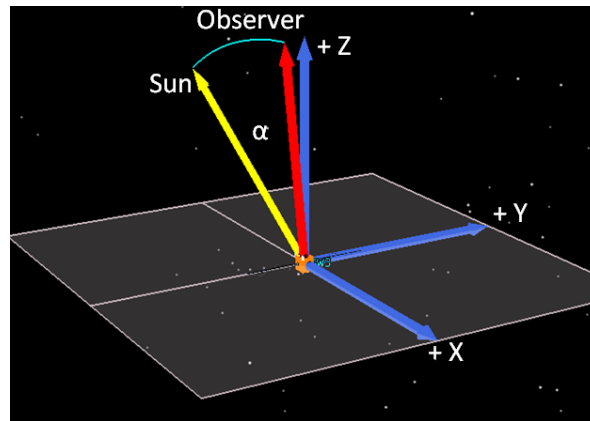


Figure 1.6: Phase angle (α) in the satellite-centered coordinate system.

1.1.3 Principles of Reflectance

Initially, this section presents the concept of specular and diffuse reflections to illustrate the relationship between a material's surface roughness and its reflective properties. The bidirectional reflectance distribution function (BRDF) is then presented to show how illumination and observational geometry, and the wavelength of the illuminating light, affect the measured reflectance.

Reflection Components

When sunlight is incident upon any satellite material it is either absorbed, transmitted, or reflected. The properties of the material determine how the incident light is reflected. A smooth material, such as solar cells, produce a specular reflection where the angle of reflection is equal to the angle of incidence. As the surface roughness increases, the specular beam widens and spreads into a specular-diffuse reflection. If the surface roughness further increases then a diffuse reflection occurs. To illustrate this, Figure 1.7 shows specular, specular-diffuse, and diffuse reflections.

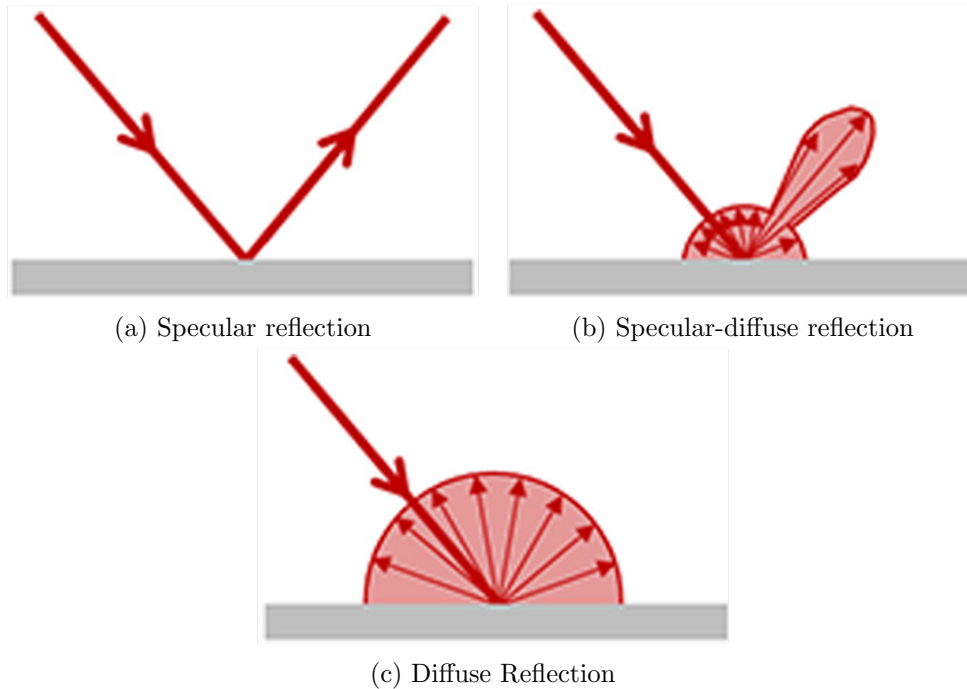


Figure 1.7: Illustration of specular, specular-diffuse, and diffuse reflections [12].

Bidirectional Reflectance Distribution Function

Here, it will be shown that photometric measurements of satellites, which are in fact measurements of spectral reflectance, depend on illumination and observational geometry, and the wavelength being considered. To quantify this dependence, the BRDF is introduced [13]. Figure 1.8 shows the components of the BRDF where the incident light arrives from a direction defined by the angles θ_i and ϕ_i and the reflected light leaves the surface, dA , from a direction defined by θ_r and ϕ_r . The incident and reflected light are contained within the solid angles $d\omega_i$ and $d\omega_r$. To include wavelength dependence the spectral BRDF is used.

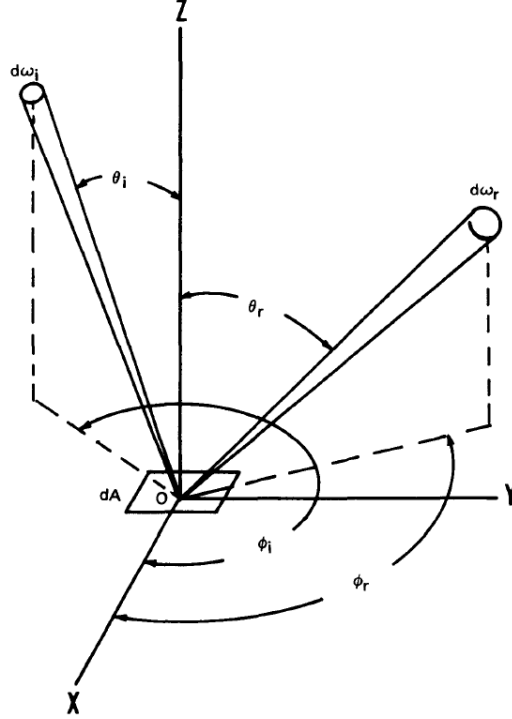


Figure 1.8: Geometry of the BRDF [13].

Before presenting the mathematical definition of the BRDF it is necessary to define the quantities upon which it depends. Irradiance (E) is the radiant flux (Φ) rate incident upon a surface (dA). Irradiance is expressed as:

$$E = \frac{d\Phi}{dA} \quad [Wm^{-2}] \quad (1.1)$$

In order for the BRDF to include directional information radiance (L) is also used. It is expressed as:

$$L = \frac{d\Phi}{\cos\theta \cdot d\omega \cdot dA} \quad [Wm^{-2}sr^{-1}] \quad (1.2)$$

Generally, the spectral BRDF is defined mathematically as:

$$f_r(\theta_i, \phi_i; \theta_r, \phi_r; \lambda) = f_r(\theta_i, \phi_i; \theta_r, \phi_r) f_r(\lambda) \quad (1.3)$$

where $f_r(\lambda)$ is the dimensionless relative spectral BRDF. Equation 1.3 is valid only if there is no interaction between the wavelength and geometrical dependencies. Finally, to include radiance, Equation 1.3 is rewritten as:

$$f_r(\theta_i, \phi_i; \theta_r, \phi_r; \lambda) = \frac{dL_r(\theta_i, \phi_i; \theta_r, \phi_r; E_i; \lambda)}{L_i(\theta_i, \phi_i; \lambda) \cos \theta_i d\omega_i} \quad [sr^{-1}] \quad (1.4)$$

The reflectance (ρ) is the ratio of reflected to incident flux. This dimensionless quantity is written as:

$$\rho = \frac{d\Phi_r}{d\Phi_i} \quad (1.5)$$

Furthermore, $d\Phi_r$ and $d\Phi_i$ can be expressed as:

$$d\Phi_r = dA \int_{\omega_r} L_r(\theta_r, \phi_r) \cos \theta_r d\omega_r \quad [W] \quad (1.6)$$

and

$$d\Phi_i = dA \int_{\omega_i} L_i(\theta_i, \phi_i) \cos \theta_i d\omega_i \quad [W] \quad (1.7)$$

Solving Equation 1.4 for L_i and substituting it into Equation 1.6 yields:

$$d\Phi_r = dA \int_{\omega_r} \int_{\omega_i} f_r(\theta_i, \phi_i; \theta_r, \phi_r; \lambda) L_i(\theta_i, \phi_i) \cos \theta_r \cos \theta_i d\omega_i d\omega_r \quad [W] \quad (1.8)$$

and as a final step, Equations 1.8 and 1.7 are substituted into Equation 1.5. The reflectance can then be expressed as:

$$\rho(\theta_i, \phi_i; \theta_r, \phi_r; \lambda) = \frac{\int_{\omega_r} \int_{\omega_i} f_r(\theta_i, \phi_i; \theta_r, \phi_r; \lambda) L_i(\theta_i, \phi_i) \cos \theta_r \cos \theta_i d\omega_i d\omega_r}{\int_{\omega_i} L_i(\theta_i, \phi_i) \cos(\theta_i) d\omega_i} \quad (1.9)$$

If it is assumed that the incident radiation is uniform and isotropic then L_i becomes constant and is brought outside the integral, thereby canceling. The result is known as the biconical reflectance and it is expressed mathematically as:

$$\rho(\theta_i, \phi_i; \theta_r, \phi_r; \lambda) = \frac{1}{\cos \theta_i d\omega_i} \int_{\omega_r} \int_{\omega_i} f_r(\theta_i, \phi_i; \theta_r, \phi_r; \lambda) \cos \theta_r \cos \theta_i d\omega_i d\omega_r \quad (1.10)$$

Biconical reflectance is the quantity that is actually measured when performing photometry on satellites and, from Equation 1.10, we see that it depends on geometry and wavelength.

1.1.4 Satellite Characterization using Photometry

Photometry is the measurement of flux to determine an object's brightness. For GEO satellites, a single photometric measurement is the sum of the reflections from individual satellite surfaces, which are an unresolved point source of light. The incident flux is integrated and converted to a magnitude, which is the difference in brightness between two objects. A magnitude difference of 5 indicates a difference in brightness of 100 [4]. An object's magnitude is expressed with the following mathematical expression:

$$m_1 = -2.5 \log \left(\frac{F_1}{F_2} \right) + m_2 \quad (1.11)$$

where, m_1 is the magnitude of the object of interest, F_1 and F_2 are the object and reference flux, and m_2 is the reference magnitude. The reference can be selected so that m_1 conforms to a standard system. For example, the Johnson system uses measurements from several main sequence stars to calculate m_2 and F_2 [14].

One common technique using photometry is to observe a satellite for several hours while taking regular measurements. The satellite's time-resolved magnitude, or light curve, is obtained from these measurements. Figure 1.9 shows a lightcurve of an active GEO satellite. Each satellite's lightcurve is unique as it is a function of both the satellite's configuration and materials, and the illumination and observational geometry.

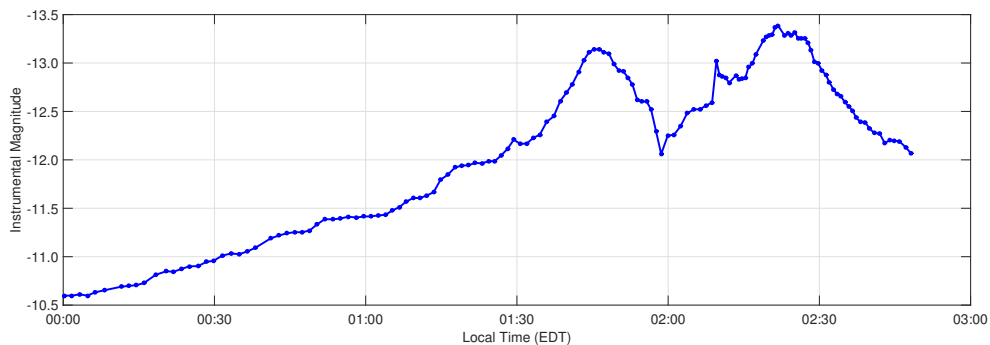


Figure 1.9: Lightcurve of an active GEO satellite.

Multicolour broadband photometry divides the visible regime into several passbands defined by a specific photometric system. The widely-used Johnson-Cousins system uses passbands between 65 - 160 nm wide [4]. Figure 1.10 shows transmittance functions of the Johnson-Cousins photometric system. The passbands are identified as Blue (B), Visible (V), Red (Rc), and Infrared (Ic) [4]. A photometric system is implemented through the use of filters with transmittance windows at the desired passband. Multicolour broadband photometry can yield additional information through the use of colour indices, which are the ratios of measured flux in each band. From Equation 1.11, the ratio of measured flux is equivalent to the difference in magnitudes. For example, the B-V, B-Rc, B-Ic, V-Rc, V-Ic, and Rc-Ic colour indices can be produced with the Johnson-Cousins photometric system.

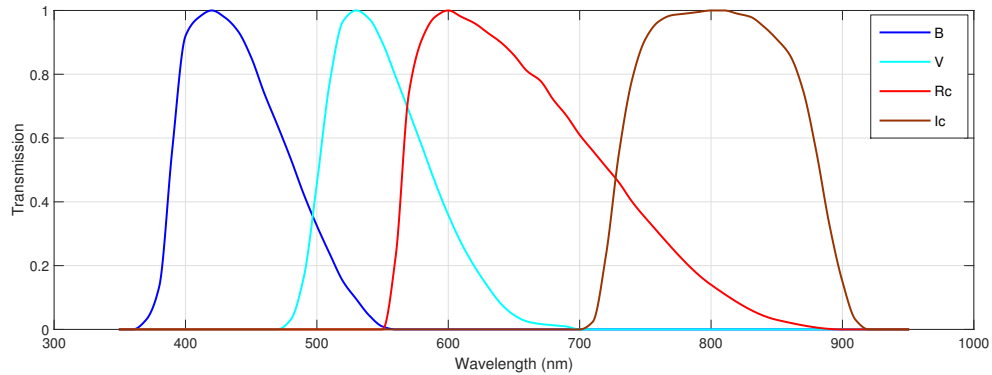


Figure 1.10: Passbands of the Johnson-Cousins photometric system [15].

Figure 1.11 shows a simplified diagram of a multicolour broadband photometry experimental setup. At the beginning of observations, the satellites of interest are acquired within the telescope's field of view (FOV) and focused onto the charge-coupled device (CCD) detector. Images are typically taken while cycling through the optical filters, which only allow wavelengths within their passband through to the CCD detector. Although photometry has been used extensively to characterize, there are still many opportunities to expand its utility.

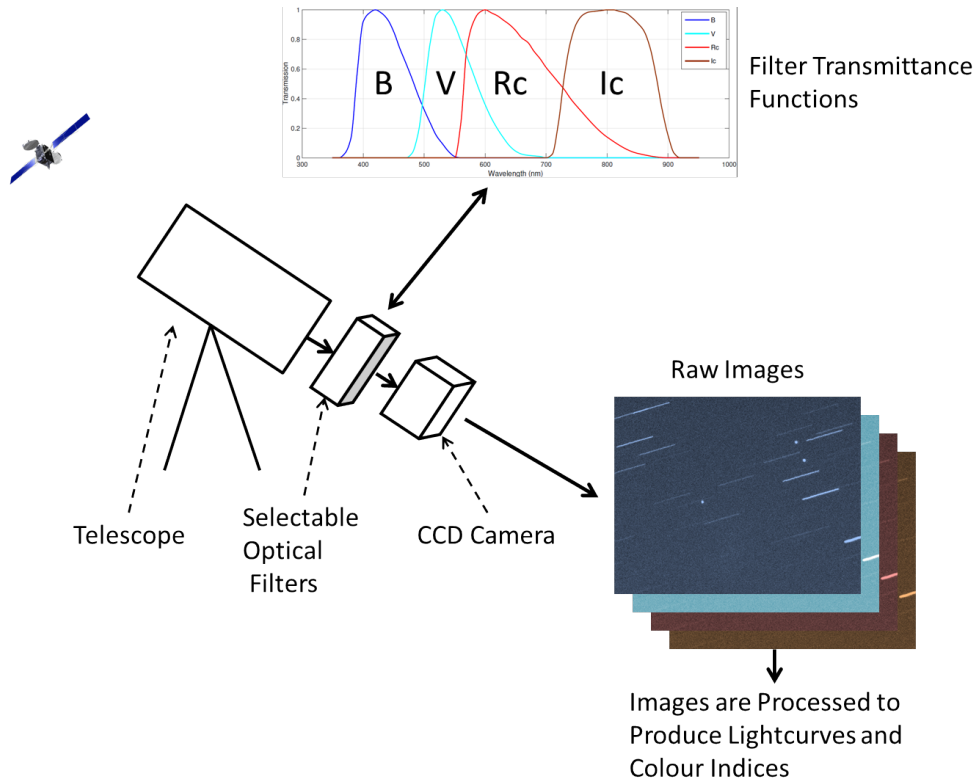


Figure 1.11: Simplified block diagram of multicolour broadband photometry.

1.1.5 Space Weathering

Satellites are subject to several interactions while in the space environment that can affect their reflective properties. This process is known as space weathering. The various causes of space weathering, such as atomic oxygen, plasma, radiation, and outgassing, are discussed in this section.

Atomic Oxygen

Material erosion by atomic oxygen is mostly a concern for spacecraft in LEO because of the high oxygen flux and orbital velocities occurring below 800 km [9]. A GEO satellite is exposed to this environment immediately after LEO insertion and during the GEO transfer orbit (GTO), which lasts several days. Atomic oxygen is a concern despite the short period that a GEO satellite spends in LEO. As Hastings *et al.* discuss, several Shuttle missions have

conducted experiments in which polyimide film samples have been found to measurably erode after several days in LEO [9]. Kapton, and other polyimide films, are used on the exterior of many satellites for thermal control purposes [10]. During their brief time in GTO, a GEO satellite's solar arrays are not fully deployed which means that the thermal insulation on the main bus structure is affected most by atomic oxygen. Figure 1.12 shows an example of the damage that can result from long-term exposure to atomic oxygen.



Figure 1.12: Space weathering damage to the Hubble Space Telescope [16].

Plasma

The plasma environment in GEO consists of high-energy charged particles which create a current flow on the spacecraft's surfaces. Current flow imbalances cause a buildup of charge creating a difference in potential of several thousand volts [9]. This causes arcing which is an additional cause of surface erosion.

Radiation

Ultraviolet (UV) and charged particle radiation are two additional causes of space weathering. Spacecraft operating in any orbit are subject to UV radiation from the Sun. It has been observed that materials exposed to the Sun's UV radiation for many months become darkened in appearance [16]. To illustrate the effects of UV radiation, Figure 1.13 shows pre-flight and post-flight photographs of NASA's Optical Properties Monitor experiment after nine months at the MIR space station. The effects of UV radiation on the outer Beta Cloth layer of the MLI blanket are the most visible. In addition

to the optical changes, it was found that the exposure to UV radiation had changed the material's solar absorbance which affected its insulating properties [17].

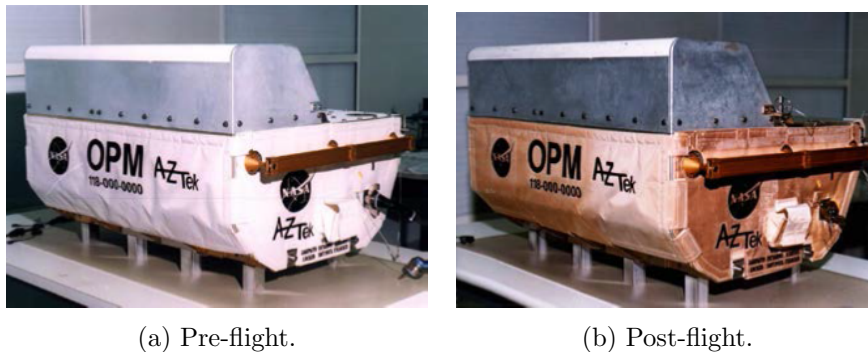


Figure 1.13: Pre-flight and post-flight photographs of NASA's Optical Properties Monitor experiment [16].

Charged particle radiation originates from galactic cosmic rays, solar proton events, and radiation belts [16]. It is the most severe in LEO while in the South Atlantic Anomaly, which is a region of increased radiation flux. Charged particle radiation contributes less to the space weathering of GEO satellites than other interactions discussed here.

Outgassing and Contamination

Outgassing occurs when the near-vacuum of space causes materials to release contaminants. These molecules are then deposited on nearby surfaces which affects their optical properties [16]. There have been several instances where outgassing has had a significant impact on a satellite's operating life. Between 1999 and 2001 five satellites with variants of the Boeing 702 bus were launched with mirrored solar concentrators attached to the solar arrays [18]. It was discovered soon after launch that outgassing from the concentrators was contaminating the solar arrays which reduced their power output. In addition, the deposited material also altered the optical properties of the solar arrays.

The interactions discussed here affect the reflective properties of the various satellite surfaces. Measuring these changes provides an additional method of satellite characterization.

1.2 Aim of the Masters Thesis

The aim of this thesis is to use multicolour broadband photometry to measure the changes in reflectance of multiple active GEO satellites caused by exposure to the space environment. In addition, there are two precursors to achieving this aim. First, it is necessary to show that identical GEO satellites can consistently exhibit similar seasonal light curve and colour index variations and that it is possible to constrain the physical source responsible for the observed light curve features. Accomplishing these precursors gives confidence that measurements for similar materials are being compared for multiple satellites.

The main effort of this thesis was a satellite observation campaign that was conducted from summer solstice through autumnal equinox. During this period, five GEO satellites were observed multiple times. Satellites with similar, or identical, bus types and different launch dates were concurrently observed. This approach allowed for direct measurements of the changes in the reflectance caused by exposure to the space environment. Repeatedly observing the same satellites also allowed the seasonal light curve and colour index variations to be observed.

1.3 Thesis Outline

This thesis is presented in the following manner:

Chapter 2 provides a literature survey that focuses on the previous work done in areas relevant to this thesis. The results from laboratory and observational experiments are discussed here.

Chapter 3 describes the experiment. The experimental setup, subject selection, and data collection procedures are described in detail in this chapter.

Chapter 4 describes, in detail, the data reduction procedures and their associated uncertainties. The instrumental magnitude extraction, apparent magnitude calibration, and colour index generation are described in this chapter.

Chapter 5 shows the seasonal light curve variations for all observed satellites. A modeled analysis is also conducted to constrain the physical origin

responsible for the observed features.

Chapter 6 shows the seasonal variations of the colour indices for all observed satellites.

Chapter 7 concludes this thesis with a summary of key findings, and recommendations for future work.

2 Literature Survey

This chapter presents a summary of the relevant work done in the field of satellite characterization. The first section presents experiments that have either focused on measuring the effects of exposure to the space environment or have concluded that it may be possible based on the results from laboratory-based experiments. The second section presents experiments that highlight the importance of illumination and observational geometry. The third section presents relevant work that has focused on the analysis of light curves and their specific features. The work that is presented here provides an insight into the feasibility of this thesis. It also highlights the factors that must be given consideration while designing the experiment to achieve its aim. Finally, the conclusion of this chapter summarizes the contributions of the work presented in this thesis.

2.1 Measuring Exposure to the Space Environment

In 2015, Bédard *et al.* conducted an experiment that characterized common spacecraft materials in a laboratory environment [19]. Two of their objectives were to measure the optical spectral scattering characteristics of spacecraft materials and to study how the reflected spectral energy distribution (SED) was affected by changing illumination and observational geometry. Of primary interest to this thesis was the relationship between a material's surface roughness and measured SED.

The experimental setup consisted of a goniometer, to precisely control the illumination and observational geometries, a spectrometer with a wavelength range between 190 and 1150 nm, and a collimated light source to simulate solar illumination. Only in-plane illumination and observational geometries were possible with this experimental setup. The four different types of materials

studied in this experiment were TJPV solar cells, aluminum panels, reflective white paint, and aluminum coated polyimide film, which is used as the outer layer of MLI blankets.

Initially, all measurements were taken with the collimated light source at a fixed incident angle (θ_i) and the detector positioned at a reflection angle (θ_r) where $\theta_i = \theta_r$. As shown in Figure 2.1, the position of the detector was then varied by $\Delta\theta_r$ until no reflected signal was received. The data products consisted of spectral BRDFs, broadband BRDFs, and colour indices.

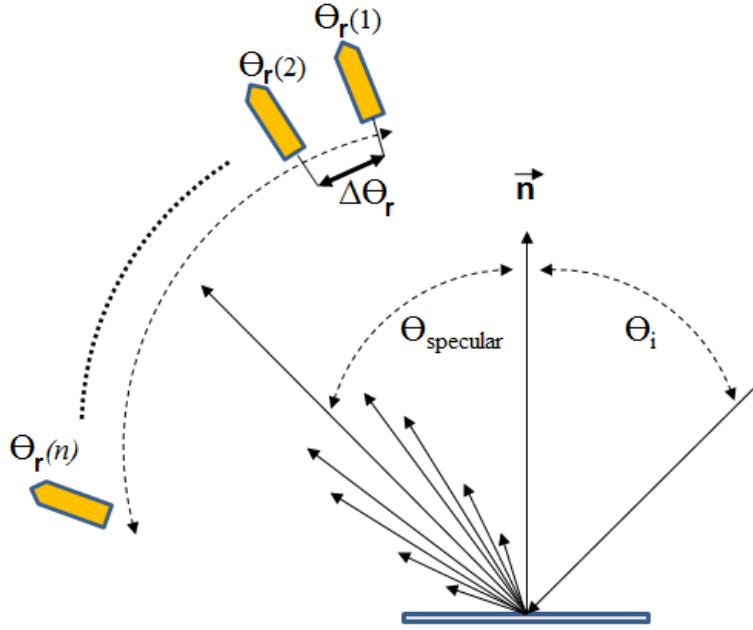


Figure 2.1: Diagram of data collection procedures [19].

Overall, the results indicated that reflected SED varies as a function illumination and observational geometry. These results will be discussed in more detail in the next section of this chapter. More applicable to the ability to measure exposure to the space environment, the results indicated that materials with a greater surface roughness had an increased reflectance at longer wavelengths. To illustrate this, Figure 2.2 shows the spectral BRDFs for the aluminum panel and white paint samples, where σ is the measured surface roughness. The increased spectral slope of the rougher materials can clearly be seen. This is caused when the roughness of the surface features are much

smaller than the longer wavelengths. The authors note that because the surface roughness of a material is likely to increase due to the effects of space weathering, the relationship between surface roughness and the reflected SED could possibly be used to measure the exposure of materials to the space environment.

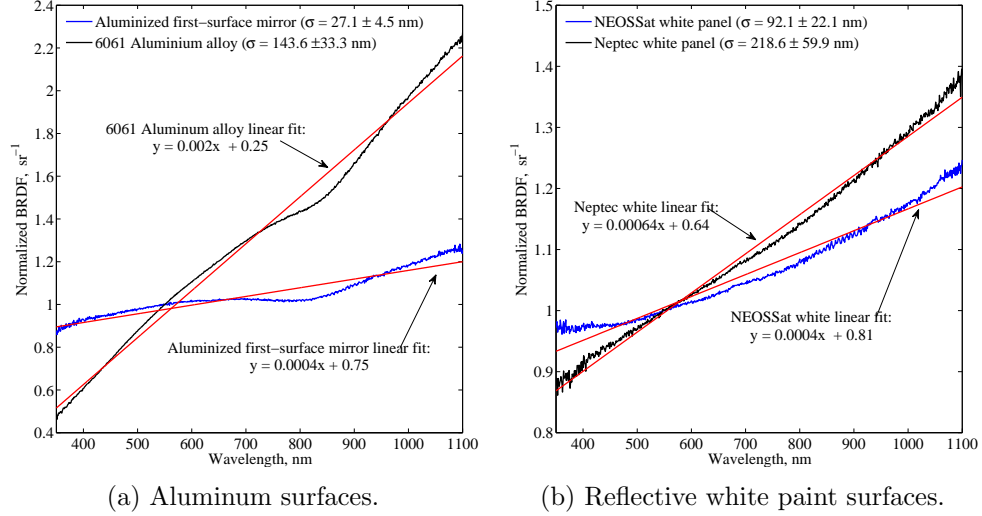


Figure 2.2: Spectral BRDF for aluminum and reflective white paint samples, normalized to unity at 550 nm and taken at $\theta_i = \theta_r = 30^\circ$ [19].

In 2015 Frith *et al.* conducted an experiment designed to measure the changes to a satellite’s reflectance while in GEO [20]. The objective of the experiment was to study the effects of the space environment on the reflectance of solar arrays as a function of time by observing identical satellites with a range of launch dates. Their colour indices were then used to measure the effects of the space environment.

All photometric measurements were taken in the near-infrared (NIR) regime between 0.9 and 2.4 μm using the United Kingston Infrared Telescope and Wide Field 2048 \times 2048 pixel camera. Measurements were taken in the Z, Y, J, H, and K NIR wavelength bands using filters. To illustrate these wavelength bands, Figure 2.3 shows the filter transmittance functions and atmospheric windows in the NIR regime. The NIR regime was selected for this experiment because previous studies had shown an increased reflectance at longer wave-

2.1. Measuring Exposure to the Space Environment

lengths, or "reddening", which allowed them to observe smaller objects and reduce exposure times.

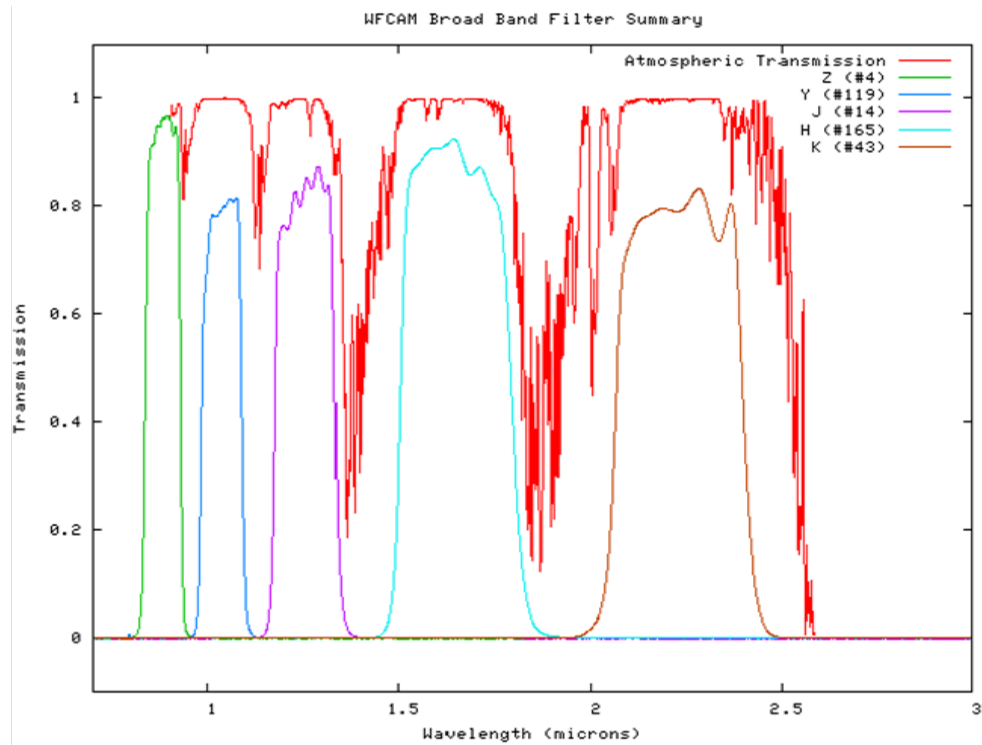


Figure 2.3: Z, Y, J, H, and K-band transmittance functions and atmospheric windows in the NIR regime [20].

In November 2014, NIR photometric measurements were taken of seven non-active GEO satellites built using the Boeing 376 bus. This bus was cylindrical-shaped and most surfaces were covered with solar cells. It was commonly used for communications missions from the late-1970s to early-2000s. The seven satellites selected for the experiment had launch dates between 1980 and 2002. The measurements were used to produce J-K and H-K colour indices and the mean value of each colour index measurement, for each satellite, was calculated and then compared for satellites with different launch dates.

Figure 2.4 shows the mean values of the J-K and H-K colour indices for the seven observed satellites as a function of their launch date. A larger value for a colour index indicates a greater relative brightness at longer wavelengths and the error bars represent the standard deviation of each nightly colour

2.1. Measuring Exposure to the Space Environment

index population. There are several instances where the results showed that the older satellites had a greater reflectance at longer wavelengths. Specifically, SBS-1, Telstar-3A, Anik-D2, MORELOS-2, and APSTAR-1's mean H-K colour index decreased as a function of their launch date. The same decreasing trend was observed in the J-K colour index for SBS-1, Telstar-3A, and Anik-D2, Palapa-B2, and APSTAR-1. No explanation was provided for the outlying data.

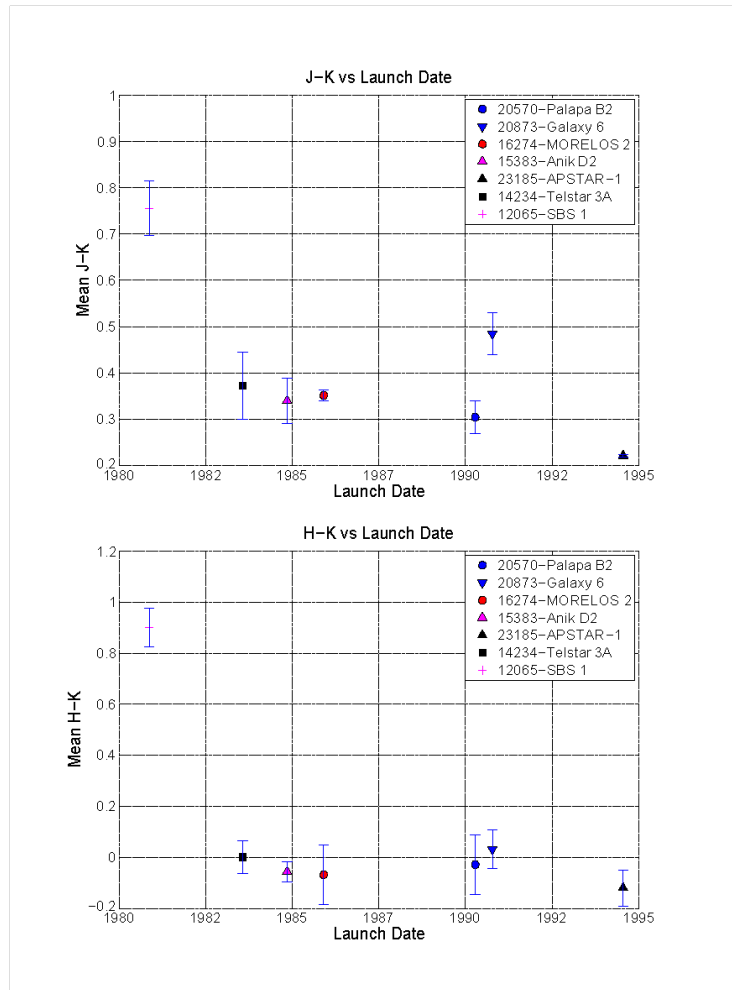


Figure 2.4: Mean values of the J-K and H-K colour indices as a function of launch date [20].

Although in many instances there was a correlation between the satellites'

increased reflectivity at longer wavelengths and their launch date, the large standard deviation values added uncertainty to the results. It is possible that selecting inactive satellites with unknown attitudes and rotational rates led to the large variance seen in the data as the illumination and observational geometries were constantly changing. Despite the uncertainties, these results indicate that it may be possible to measure the effects of exposure to the space environment using similar, but better controlled, experimental techniques.

2.1.1 Summary

The results presented by Bédard *et al.* showed that materials with a greater surface roughness have an increased reflectance at longer wavelengths. Paired with the relationship between space weathering and increased surface roughness, the results indicate that it may be feasible to measure exposure to the space environment with an observational experiment. The results presented by Frith *et al.* also suggested this may be possible. However, the large uncertainties in their results suggested that the experimental techniques must be further refined.

2.2 Illumination and Observational Geometry

Between 2009 and 2010, Cowardin *et al.* characterized several common spacecraft materials in a laboratory environment [21, 22]. The objective of these experiments was to obtain the intrinsic properties of orbital debris in GEO by comparing observational and laboratory results. The laboratory results are relevant as they show the relationship between varying illumination and observational geometry and a material's measured colour indices.

Samples from 20 different materials thought to be representative of the space debris population were selected for this experiment. They consisted of MLI, solar cells, aluminum, and electronics components. The experimental setup was comprised of a Zenon arc lamp to simulate solar illumination, a CCD detector, and Johnson-Cousins filters in the B, V, Rc, and Ic bands. The experimental setup allowed for a variable phase angle and material rotation angle. Each material was rotated through a full 360° in 10° increments at a fixed phase angle of 6° . This experimental setup was designed to simulate the illumination and observational geometries that would be encountered during optical observations of space debris in GEO. Unfortunately, the fixed phase angle limited these geometries.

Measurements of each illuminated material were taken while rotating it at 10° intervals. Three different colour indices (B-V, B-R, and B-I) were calculated for each material by taking the mean value of the measurements at each rotational interval. Figure 2.5 shows the B-R and B-V colour indices for the 14 material samples. A value larger than the Sun's, for either of these colour indices, indicates the reflected light has a greater relative intensity at longer wavelengths. Simply stated, larger values indicate the reflected light is redder than the Sun and smaller values indicate the reflected light is bluer than the Sun. Three of the MLI samples and the JPL solar panel had the most notable results as they were significantly redder than the Sun in both colour indices.

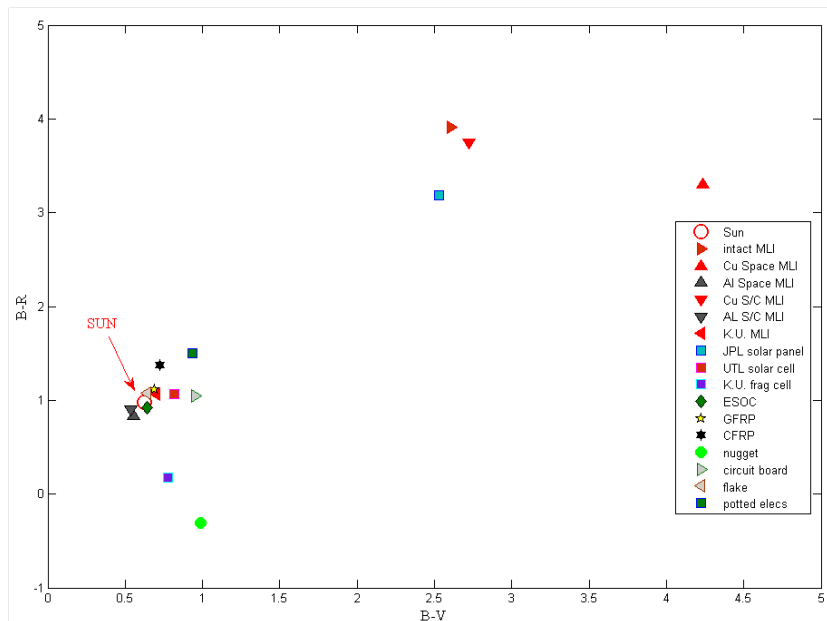


Figure 2.5: Solar corrected photometric B-R vs. B-V colour indices for 14 laboratory material samples [21].

Significant variations in the colour indices were observed when some of the material samples were rotated. This was evident in the variance of the materials' colour indices. Table 2.1 shows the mean values of the B-V and B-R colour indices, and their standard deviations, for three of the space-facing materials that were characterized. The experimental technique used to obtain these data essentially simulated a tumbling object and using the mean value of the colour indices from all illumination and observational geometries resulted

in an inherent loss of information.

Material	B-V	B-R
Intact MLI (space-facing)	2.0 ± 0.8	2.9 ± 1.1
Layer MLI (space-facing Kapton)	3.6 ± 1.0	2.3 ± 1.3
Intact solar cell	0.2 ± 0.2	0.1 ± 0.5

Table 2.1: Colour indices of spacecraft material samples [21].

In 2012, Lederer *et al.* conducted an experiment that characterized GEO satellites and laboratory samples [23]. Broadband photometric measurements of inactive GEO satellites and solar cell samples were taken in the visible regime. Their objective was to evaluate the capabilities of this technique to characterize, and possibly identify, space-based materials. The broadband photometric results are discussed here.

The satellites of interest belonged to the Initial Defense Communications Satellite Program (IDCSP). In the mid 1960s the United States launched 35 of these small satellites into sub-Geosynchronous orbits. They were 26-sided polygons with a diameter of 0.86 m and completely covered in solar cells. Figure 2.6 shows a model of a IDCSP satellite [23]. All satellite measurements were taken with a 0.9 m telescope, Tek 2048 \times 2048 pixel CCD, and Johnson-Cousins B,V,Rc, and Ic photometric filters. The laboratory samples consisted of six modern solar cells, five of which were designed for space applications. A 75 watt Xenon arc lamp was used to simulate solar illumination and an SBIG 1024 \times 1536 pixel CCD with similar filters was used to obtain measurements of the laboratory samples.

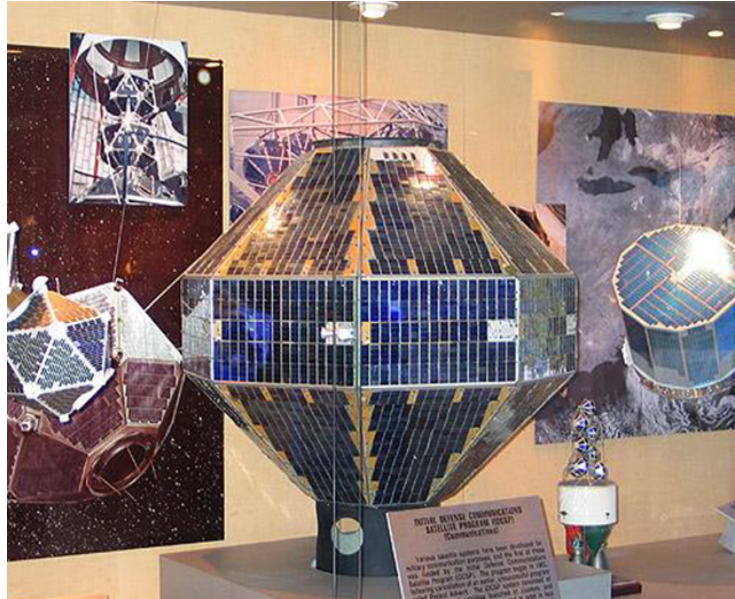


Figure 2.6: Model of IDSCP satellite [23].

Broadband photometric measurements of 18 IDCSP satellites were obtained over four nights in April 2012. Average B-R, B-I, and R-I colour indices were calculated from 10 - 20 sets of images. The colour indices for the laboratory samples were obtained in a similar fashion. Figure 2.7 shows the B-V and B-R colour indices for the IDCSP satellites and solar cell samples. The Sun is shown for reference and the error bars represent the standard deviation of the colour indices obtained from the multiple images.

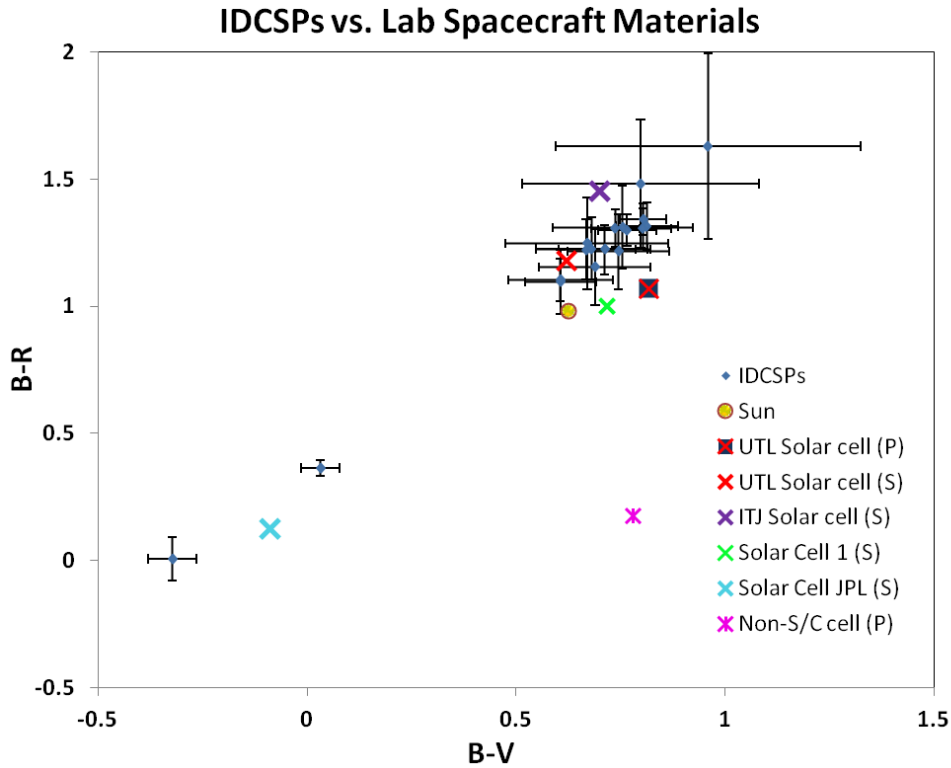


Figure 2.7: B-V and B-R colour indices for IDCSP satellites and laboratory solar cell samples [23].

The authors attributed the large variance observed for some of the satellites to their unstabilized attitude as the satellites' rotational parameters were unknown. Similar to Cowardin *et al.*, using the mean value from measurements obtained at changing, or unknown, illumination and observational geometries resulted in a loss of information and large uncertainties.

The experiments presented thus far in this section have given little consideration to the effects of changing illumination and observational geometry. Consequently, their objectives were only partially met. In 2013 Bédard addressed this with a laboratory experiment to characterize how the measured SED of common spacecraft materials changed as the illumination and observational geometries were varied [24].

The experimental setup and the materials under consideration have been presented in the previous section [19]. This section discusses the relationship between a material's calculated colour indices and illumination and observational geometry. Measurements were taken with θ_i at angles of 10° , 30° , and 60° . Initially, measurements were taken when $\theta_i = \theta_r$ and the detector was then rotated by $\Delta\theta_r$ until no reflected light was detected. The value for $\Delta\theta_r$ varied greatly by material. The data were processed for each material to produce a spectral BRDF, a broadband BRDF, and colour indices. The spectral BRDF used by Bédard included measured quantities and it is rewritten from Equation 1.4 as:

$$f_r(\theta_i, \theta_r, \lambda) = \frac{S_r/t_{exp(r)}}{S_o/t_{exp(o)} \cdot \cos \theta_r \cdot \Delta\omega_s} \quad (2.1)$$

where S_r and S_o are the measured reflected and reference signal, $t_{exp(r)}$ and $t_{exp(o)}$ are the exposure times, and $\Delta\omega_s$ is the solid angle formed from the detector's FOV. Equation 2.1 was integrated over all observed wavelengths to produce the broadband BRDF which was then multiplied by the Johnson-Cousins B, V, Rc transmittance functions to produce the colour bands. The B-V, B-R, and V-R colour indices were then produced.

Broadband BRDFs and colour indices were produced for four types of TJPV cells, an aluminized mirror, an aluminum alloy panel, two types of white panels, and new and degraded MLI samples. Select results are shown here. Figure 2.8 shows the normalized broadband BRDFs and B-V, B-R, and V-R colour indices for the TJPV solar cell, aluminum mirror, and reflective white paint.

2.2. Illumination and Observational Geometry

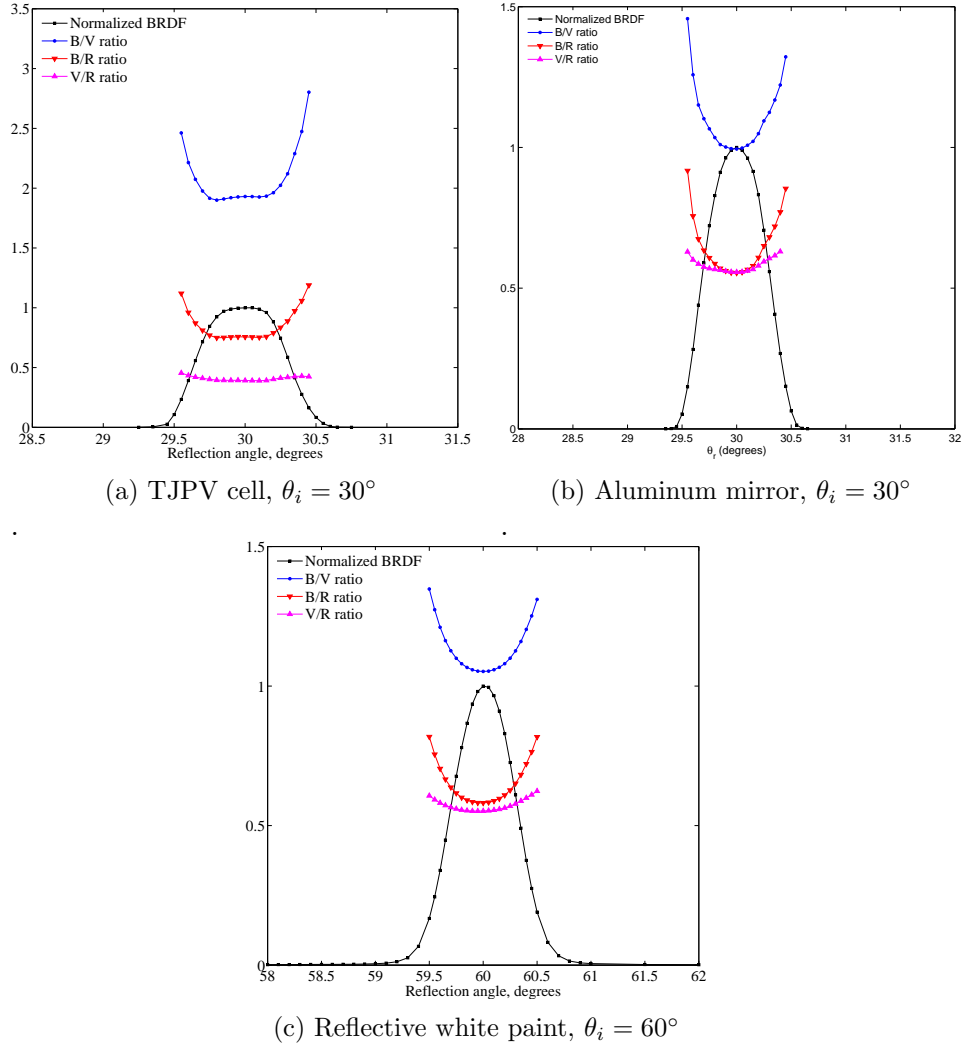


Figure 2.8: Normalized broadband BRDF and colour indices for TJPV solar cell, aluminum mirror, and reflective white paint [24].

These results show two particular points of interest to this thesis. First, the highly specular nature of these three materials can be seen as the FWHM for each broadband BRDF is less than a degree wide. Consequently, the small specular reflection cone means that observing a purely specular reflection is highly dependent on illumination and observational geometry. Secondly, all colour indices for the materials presented here increased as θ_r was varied from

$\theta_{specular}$ which indicates an increased reflectance at longer wavelengths. As a result, any attempt to characterize satellites using their colour indices must give great consideration to the illumination and observational geometries at which the photometric measurements are taken.

2.2.1 Summary

The objective of this section was to show the importance of illumination and observational geometry in the context of measuring the effects of the space environment. The results presented by Cowardin *et al.* and Lederer *et al.* showed that attempting to combine multiple measurements, taken at different illumination and observational geometries, results in a large variance. Bédard's experiment showed that the assumption that a material's SED is invariant, despite changing illumination and observational geometry, is incorrect. Consequently, if the precise illumination and observational geometries are not known when an object's SED is measured then the results have less utility.

2.3 Light Curve Analysis

In 2006, Payne *et al.* published the results from a two year GEO satellite characterization experiment [25]. The objective was to establish a classification system that assigned GEO satellites to a class based on their observed light curve structure. For this experiment the photometric signatures for 36 GEO satellites were obtained. All observed satellites had orbital longitudes placing them over North America and the Pacific Ocean. Data were obtained with a 1 m telescope from the US Naval Observatory's Arizona station. At a minimum, the satellite of interest was observed for approximately one hour on either side of the predicted nightly minimum phase angle. All observed satellites were launched between 1993 and 2004 and had several different bus types and configurations.

From the observed light curves the author defined five classes. They were Canonical, Lockheed Martin A2100, Peculiar, Telstar, and Boeing BSS702C. The Canonical class was the simplest and most common. It featured a single bright peak occurring at, or near, the minimum phase angle. The A2100 class had a more complex non-symmetrical structure with a decrease in observed brightness occurring near the minimum phase angle. The Telstar and BSS702C classes had a fundamental canonical structure with additional secondary peaks. The Peculiar class featured variations in brightness and a lack

of symmetry. From the 36 GEO satellites studied, 17 were Canonical class, 11 were A2100 class, 5 were peculiar class, and 1 was BSS702C class.

Figure 2.9 shows the observed magnitude as a function of phase angle for AMSC-1 (1995) and DirecTV-1R (1999). Both satellites, which have a variant of the Boeing 601 bus, had light curves that were classified as canonical by the authors. Although no dates were given for these observations, the gaps in the data indicate that they occurred near equinox when the satellites were eclipsed by the Earth. Of note, the bright peak for DTV-1R did not occur at the minimum phase angle. The authors attributed this to solar array pointing offsets. However, Figure 2.9 does show that satellites with a similar bus type exhibit similar light curve structures.

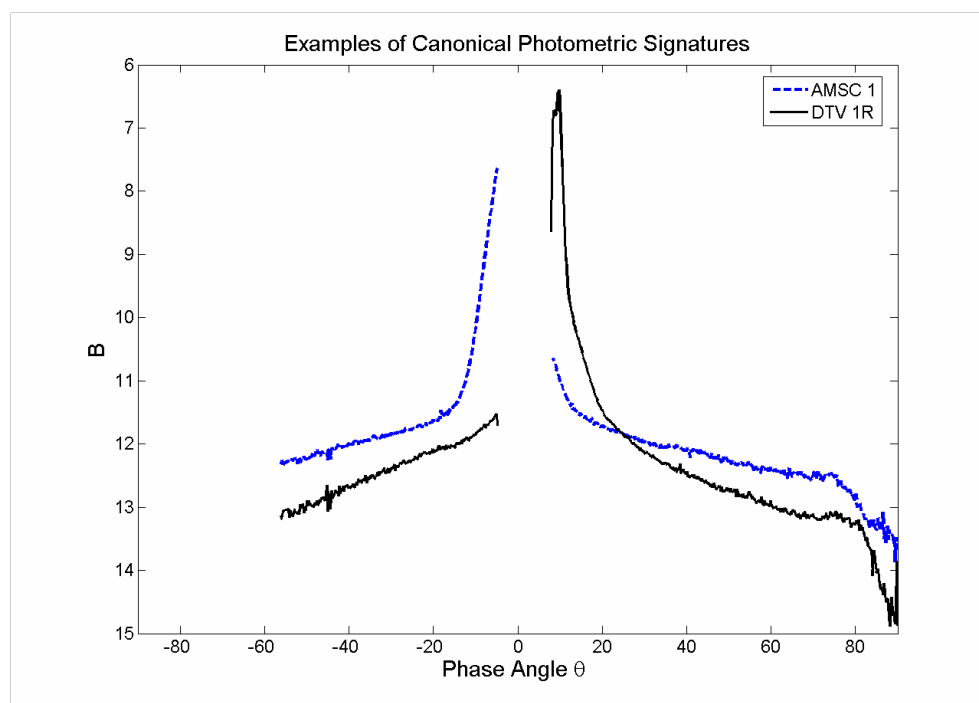


Figure 2.9: Observed magnitude as a function of phase angle for two Canonical class GEO satellites [25].

In this study, the author stated that a satellite's solar arrays are responsible for the brightest observed light curve features but the author does not present a quantitative analysis to support this. There were also instances where identical satellite bus types were assigned different light curve classifications. For

example, Galaxy-11 and Anik-F1 both feature an identical variant of the BSS-702 bus but Galaxy-11 was classified as BSS702C and Anik-F1 was classified as Peculiar. This was possibly because these two satellites were located at orbital longitudes of $55^\circ W$ and $107^\circ W$ which created different illumination and observational geometries. However, this classification technique demonstrated that similar satellite buses can produce predictable and repeatable light curves. This is an implicit requirement for this thesis because it is the basis for comparing photometric measurements for two satellites with similar bus types.

In 2014, Jolley conducted an observational experiment that characterized five active GEO satellites [8]. His primary objective was to evaluate the ability of a small-aperture telescope to accurately obtain photometric measurements. Relevant to this thesis was the light curves that were produced for similar satellite buses located at the same orbital longitude.

All photometric measurements were taken with a 0.36 m Celestron CG-14 telescope and Apogee Alta U42 camera, which has a 2048×2018 pixel CCD. Each night, standard stars were also observed for calibration purposes. Table 2.2 shows the bus type and orbital longitude of the GEO satellites observed for this experiment between July and November 2013.

Satellite	Bus Type	Orbital Longitude
Galaxy-11	BSS702C	$35.5^\circ W$
Intelsat-805	AS-7000	$35.5^\circ W$
Anik-F1	BSS702C	$107.3^\circ W$
Anik-F1R	Eurostar-3000S	$107.3^\circ W$
Anik-G1	LS-1300	$107.3^\circ W$
Echostar-17	LS-1300	$107.1^\circ W$

Table 2.2: Observed satellites, bus type, and orbital longitude [8].

Echostar-17 and Anik-G1 were co-located at an orbital longitude of $107.2^\circ W$ which allowed them to be concurrently observed with nearly identical illumination and observational geometries. Although both satellites had a LS1300 bus, they had different solar array configurations. Figure 2.10 shows the V-band light curves for Echostar-17 and Anik-G1 during October and November 2013. These results show that the light curves are similar in overall structure and peak brightness. However, the time that the single bright peaks were

observed was different. Despite having nearly identical illumination and observational geometries, Anik-G1’s single bright peak was consistently observed approximately 30 minutes later than Echostar-17’s bright peak.

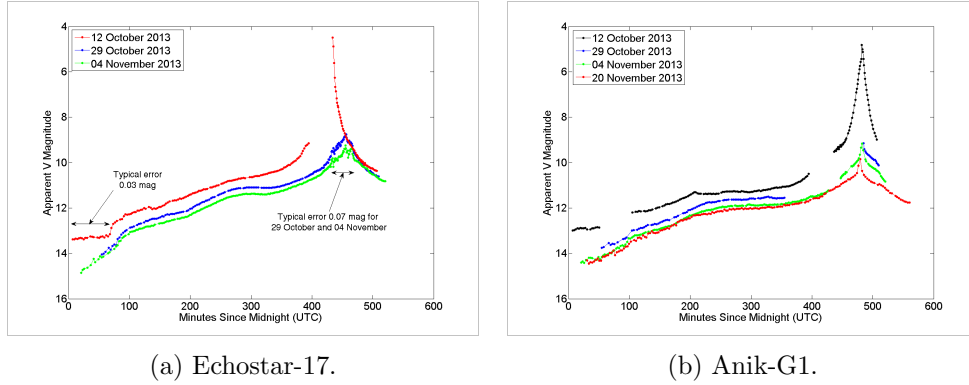


Figure 2.10: V-band light curves for Echostar-17 and Anik-G1 [8].

Jolley’s results confirm that satellites with similar buses exhibit similar light curve features but the time offset between the two satellites’ bright peaks suggests that the solar arrays, or other reflecting surface, may have had different orientations at the time of these observations. Therefore, it is necessary to further investigate the sources of these peaks to ensure that similar materials are being compared.

In 2013 Hall *et al.* conducted an analysis of the faint glints observed for GEO satellites which are generally assumed to originate from a specular surface other than the large solar arrays [3]. Their objective was to develop an analysis technique that demonstrated that these faint glints originated from either the main bus structure or Sun-tracking solar arrays.

Galaxy-15 was the focus of this experiment. In 2010, this satellite experienced a near-critical failure that resulted in a loss of communications and control and, as a result, it began to drift eastward from its original orbital longitude of $133^{\circ}W$. The observations for this experiment occurred during a period when the satellite was known to be in a stable attitude. Photometric measurements were taken using a 0.28 m telescope and Ic-band filter.

Figure 2.11 shows the complete Ic-band measurements of Galaxy-15 in November 2010. For display purposes, an offset of one magnitude was added to each successive night. The faint glint occurring each night at approximately 10.5 UT hours was the focus of this analysis.

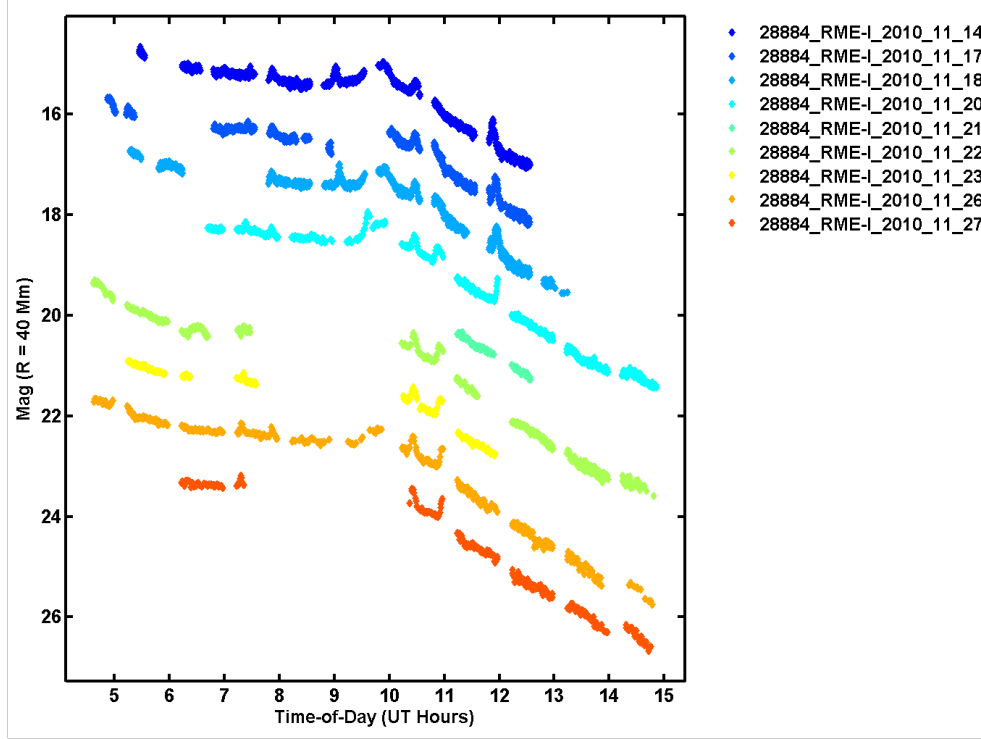


Figure 2.11: I-band lightcurves for Galaxy-15 in November 2010 [3].

Hall *et al.* used vector analysis to explain the source of the faint glints observed at approximately 10.5 UT hours each night. The first vector introduced was the phase angle bisector unit vector, $\hat{\mathbf{b}}(t)$. The phase angle bisector cuts the phase angle into two equal angles. Next, the facet surface normal unit vector, $\hat{\mathbf{n}}(t)$, was introduced. This unit vector is normal to any satellite surface of interest. For example, $\hat{\mathbf{n}}(t)$ can be the surface normal unit vector of the solar arrays or any other surface. $\hat{\mathbf{b}}(t)$ and $\hat{\mathbf{n}}(t)$ both exist in an inertial reference frame. The perfect glint, occurring at t_g , satisfies the following condition:

$$\hat{\mathbf{n}}(t_g) \cdot \hat{\mathbf{b}}(t_g) = 1 \quad (2.2)$$

Hall *et al.* noted that further information can be gained by assuming that a specularly reflecting facet, such as a mirrored body panel, is likely to remain fixed within the satellite body reference frame. A coordinate transformation was used to transform $\hat{\mathbf{b}}(t)$, which exists in an inertial reference frame, to the satellite body reference frame. The resulting vector, $\hat{\mathbf{b}}'(t)$, is the phase angle bisector within the satellite body reference frame. Furthermore, the authors recognized the solar arrays actively track the Sun and do not remain fixed within the satellite body reference frame. Again, a coordinate transformation was used to transform $\hat{\mathbf{b}}(t)$ to the solar array reference frame. This vector, $\hat{\mathbf{b}}''(t)$, is the phase angle bisector within the solar array reference frame.

To complete their analysis the authors plotted the glint feature at 10.5 UT hours as a function of the body and solar array phase angle bisectors. More precisely, the azimuthal component of the phase angle bisector vectors within each of their reference frames were used. Figure 2.12 shows Galaxy-15's faint glint as a function of the azimuthal component of the phase angle bisector. The left pane shows that the glint is consistently associated with a specific phase angle bisector. This indicates that a fixed structural component is responsible for this faint glint. The right pane shows no consistent relationship between the phase angle bisector and the time the faint glint was observed. This indicates that it does not originate from the Sun-tracking solar arrays.

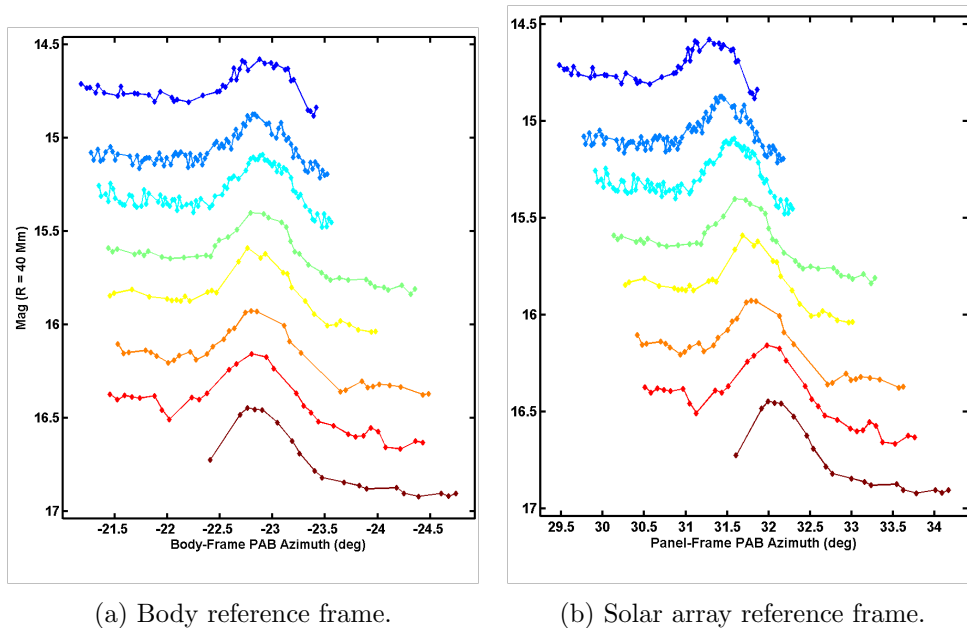


Figure 2.12: Galaxy-15 faint glint feature as a function of the phase angle bisector in the body and solar array reference frames [3].

This experiment showed that a quantitative vector-based analysis of the illumination and observational geometries can be used to determine if the main bus structure or Sun-tracking solar arrays are responsible for the observed glints. From these results, a further analysis could have been conducted to determine the orientation of the particular facet responsible for the faint glint feature. Using an analysis technique similar to this will allow similar satellite surfaces to be compared which will be of benefit when attempting to measure the effects of the space environment on satellite materials.

2.3.1 Summary of Light Curve Analysis

The objectives of this section were to demonstrate that active GEO satellites with similar, or identical, buses can exhibit similar and repeatable light curves and that the reflecting surfaces responsible for the observed light curve features can be identified with a quantitative analysis. Payne *et al.* demonstrated that similar active GEO satellites do exhibit similar light curves. This was verified by Jolley. Hall *et al.* demonstrated that a quantitative analysis can be used to determine if the observed light curve features originate from

the solar arrays or main bus structure. These results show that it is possible to compare photometric measurements for multiple satellites with similar bus types. Furthermore, determining the source of the observed light curve features allows similar materials to be compared.

2.4 Summary of Contribution to this Research

This chapter has described the previous work that is relevant to the aim of this thesis. In addition, the requirements to successfully accomplish this have been considered. The specific contributions to the field of SSA from the work presented in this thesis include:

- The capability to measure the effects of the space environment on active GEO satellites with identical bus types using multicolour broadband photometry in the visible regime.
- An analysis of the seasonal light curve and colour index variations for similar active GEO satellites.
- Modeling of specular reflection vectors from the solar arrays and main body structure to constrain the physical origin of the observed light curve features.

3 Experimental Setup and Procedures

The main effort of this thesis was a satellite observation campaign that was conducted between late June and late October 2015. A small-aperture telescope, CCD detector, and optical photometric filters were used to obtain multicolour broadband photometric measurements of five active GEO satellites.

3.1 Experimental Objectives

1. **Obtain multicolour broadband photometric measurements of active GEO satellites of similar bus type and different launch date:** From these measurements it was possible to determine if the effects of the space environment on satellite materials can be inferred with multicolour broadband photometry. Ideally, satellites with an identical bus and different launch date were concurrently observed. This approach ensured that the atmosphere and the illumination and observational geometries had a similar influence on the photometric brightness and colour indices.
2. **Obtain multicolour broadband photometric measurements of active GEO satellites in seasonally varying illumination geometries:** The second experimental objective allowed for the seasonal changes in the satellites' light curves and colour indices to be observed. Continuous observation of the satellites between late June and late October provided the full range of seasonal geometries possible in the summer. These results were used to determine if active GEO satellites, with a similar bus, exhibit similar seasonal light curve and colour index variations.

3.2 Equipment Description

This section provides a description of the equipment used for this experiment. The limiting factors and considerations are also discussed.

3.2.1 Telescope

All data were collected using a Meade LX-200 small-aperture telescope with a 0.3 m aperture and f/10 focal ratio. Initially, there were concerns that long exposure times would be required to achieve a suitable SNR. The small-aperture telescope was the primary reason for these concerns. However, initial evaluations showed that exposures between 5 - 20 seconds were sufficient, with the shorter exposures occurring when the brightest light curve features were observed. This experimental setup had a FOV that allowed multiple satellites to be observed concurrently.

Each night, the telescope was mounted on its field tripod and aligned using its internal algorithm. After the initial alignment, the telescope was controlled in situ with *TheSkyX* software, which had the capability to track stars and GEO satellites. The latest two-line element sets (TLEs) of the satellites being observed were obtained prior to each observation from *Space-Track* [26].

3.2.2 CCD Detector

The CCD detector used for all data collection was the Quantum Scientific Imaging 690ws [27]. From Figure 3.1, a quantum efficiency (QE) between 60 and 75% is typical in the visible regime. The integrated Johnson-Cousins optical filters allowed the CCD detector to be mounted directly to the telescope without the need for an external filter wheel. The CCD detector and filters were also controlled with *TheSkyX*.

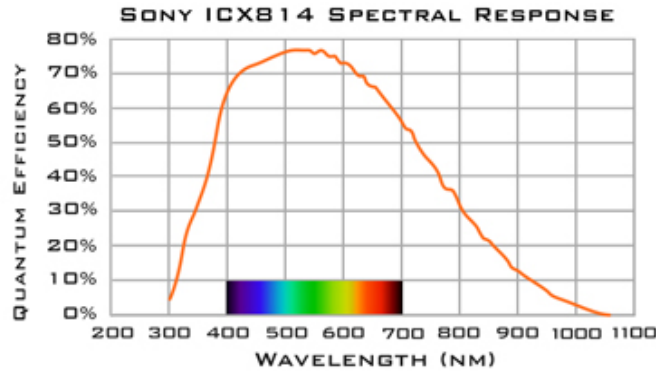


Figure 3.1: Quantum efficiency for the QSI-690ws CCD camera [27].

Pixel binning is the process where the accumulated charge in adjacent pixels is summed, or binned, into a single pixel [28]. This is typically done to achieve the optimal combination of ADU level and FWHM for all observed objects. Similar to stars, GEO satellites appear as unresolved point sources of light which means that no further detail can be seen by using smaller pixels. A FWHM value between two and four pixels provides an optimal trade off in terms of SNR, error rejection, and data reduction [28].

The highest possible ADU level is achieved when an object's flux is incident on the fewest possible pixels. However, care has to be taken to ensure that the object does not become undersampled. In this case, its FWHM becomes smaller than a single pixel which can cause photometric errors during the data reduction process. On the contrary, an oversampled object requires longer exposure times to achieve a sufficient ADU level and, since the object's flux is spread over more pixels, the likelihood of encountering a bad pixel during the data reduction process increases greatly. Another consideration is the CCD readout speed. As the binning is increased, the total number of pixels decreases which results in a faster readout speed.

Figure 3.2 shows several pixel binning schemes, where the red circle represents the FWHM of the image of a GEO satellite or star, and the squares represent individual pixels. Figure 3.2a shows the situation where the image is slightly oversampled. Figure 3.2b shows a critically-sampled image where the object's FWHM occupies slightly less than two pixels. Finally, Figure 3.2c shows an undersampled image where the object occupies less than one pixel.

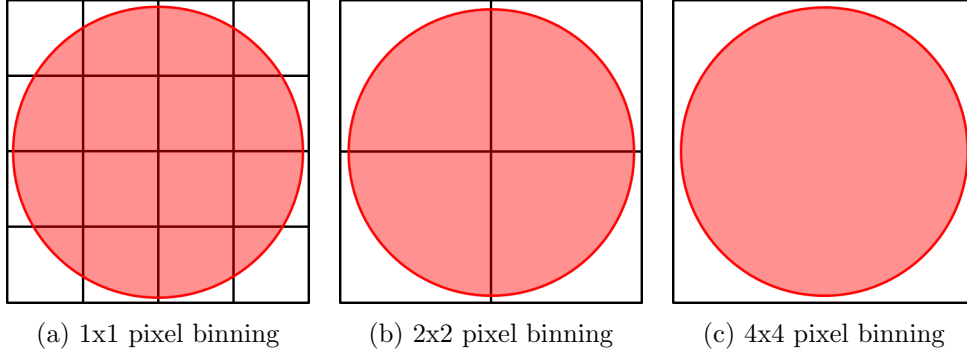


Figure 3.2: Illustration of CCD pixel binning schemes.

The first step to determining the optimal binning scheme was calculating the experimental setup's FOV. It was calculated with the following expression:

$$FOV = 2 \arctan \left(\frac{d}{2f} \right) \quad (3.1)$$

where d is the CCD's width (12.48 mm) and f is the telescope's focal length (3048 mm) [27]. The FOV for this experimental setup was calculated to be 14×11 arcminutes. Next, the image scale (s) was calculated. It is the angular distance of the sky corresponding to a unit linear distance on the CCD. It is expressed mathematically as:

$$s = \frac{FOV}{d} \quad (3.2)$$

The image scale was calculated to be 1.13 arcminutes/mm. The pixel scale, which is the angular distance of the sky corresponding to a single pixel, was then calculated for 1×1 to 4×4 pixel binning schemes. It was calculated by multiplying the pixel width, which was determined by the binning scheme, by the image scale. A single unbinned pixel had a width of $3.69 \mu\text{m}$ [27]. This width increased in proportion to the binning scheme used (ie. $7.38 \mu\text{m}$ for 2×2 , $11.07 \mu\text{m}$ for 3×3). From the pixel scale, an estimation of the number of pixels required for the satellite's FWHM in each binning scheme was calculated from an approximate satellite FWHM of 3.5 arcseconds. Table 3.1 shows the results of these calculations.

For this experiment it was found that a 3×3 pixel binning scheme provided the optimal trade between sampling, exposure times, and readout speed. It

also ensured that the observed satellites would not be undersampled on nights where the atmospheric conditions resulted in smaller FWHM values.

Binning Scheme	Pixel Scale (arcsec/pixel)	FWHM (pixels)
1×1	0.25	12
2×2	0.50	6
3×3	0.75	4
4×4	1.00	3

Table 3.1: Pixel scale and FWHM for increasing pixel binning schemes.

3.3 Experimental Subjects

GEO satellites are generally positioned in clusters where 3 - 4 satellites are within a detector's FOV. The bus type and age of all satellites within each cluster were first identified in an effort to find satellites with identical buses. Nine possible clusters met this initial criteria. However, the satellites within many of these clusters had a different variant of the same bus, which meant that the external payload and solar array configuration were different. Given that a satellite's solar arrays are its largest reflecting surface, it was deemed that a change in the solar array configuration would significantly influence a satellite's overall reflectance. As such, only satellites of the same bus type and similar solar array configuration were considered. Two clusters of satellites met this final criterion.

Within these two clusters, a total of five satellites were observed during the campaign. They each had variants of the Boeing 702-HP bus which has been operational since 1997 with 28 units launched as of June 2015 [11]. All Boeing 702-HP variants have a box-wing configuration with the solar arrays and payload configuration tailored to meet the requirements of each mission. Table 3.2 provides a summary of the properties of the five GEO satellites that were observed. For illustration purposes, Figures 3.5 - 3.3 show artist renditions and diagrams of these satellites.

Satellite	Year Launched	Longitude	Bus Type	Length
Galaxy-3C	2002	95°W	BSS-702HP B	48 m
Spaceway-1	2005	103°W	BSS-702HP A	41 m
Spaceway-3	2007	95°W	BSS-702HP A	41 m
DirecTV-10	2007	103°W	BSS-702HP C	48 m
DirecTV-12	2009	103°W	BSS-702HP C	48 m

Table 3.2: Properties of the observed satellites.

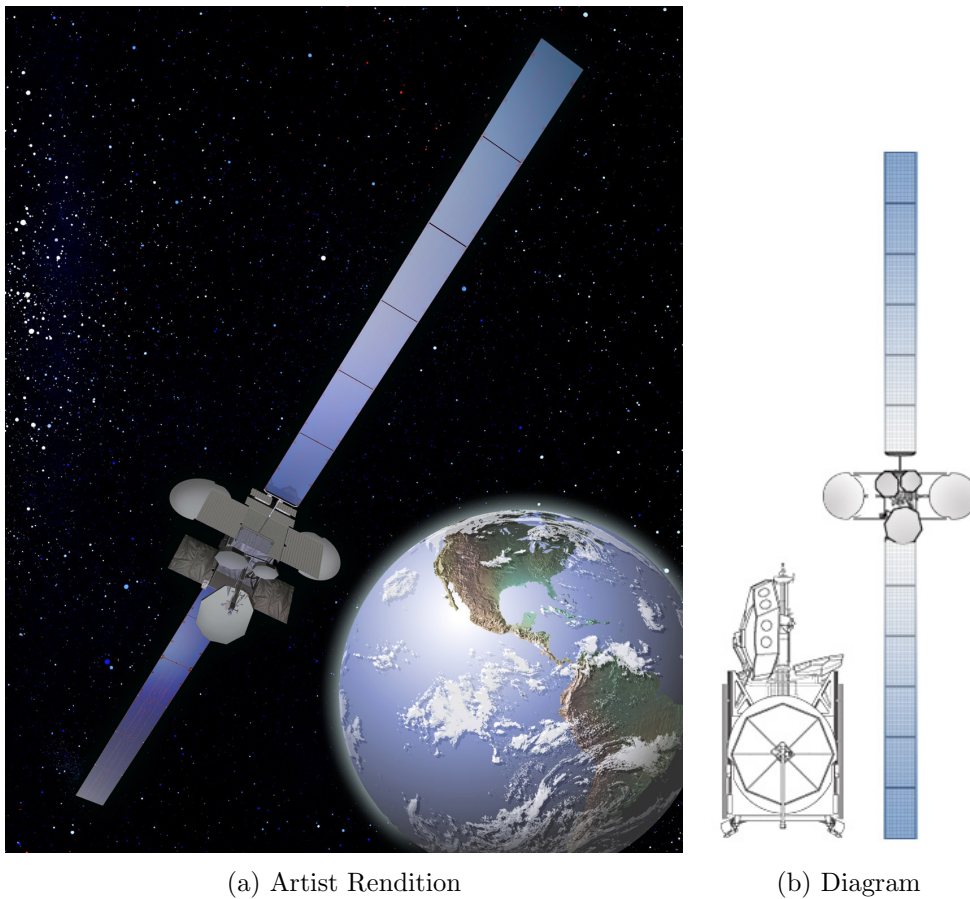
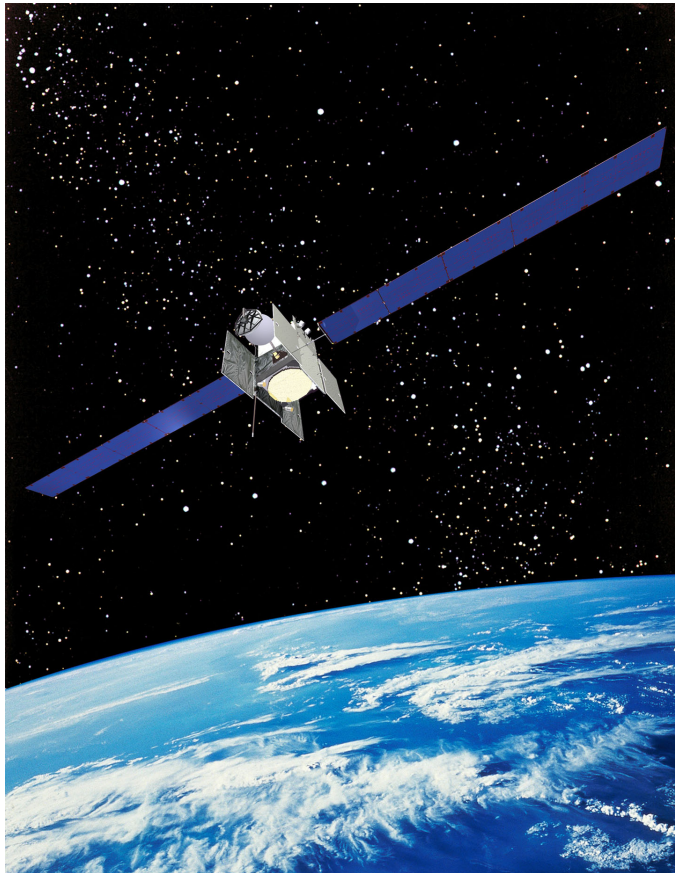
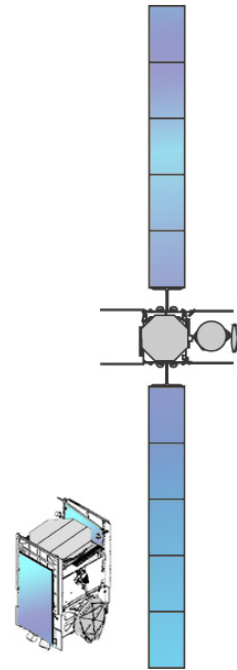


Figure 3.3: Galaxy-3C [11].



(a) Artist Rendition



(b) Diagram

Figure 3.4: Spaceway-1 and Spaceway-3 [11].

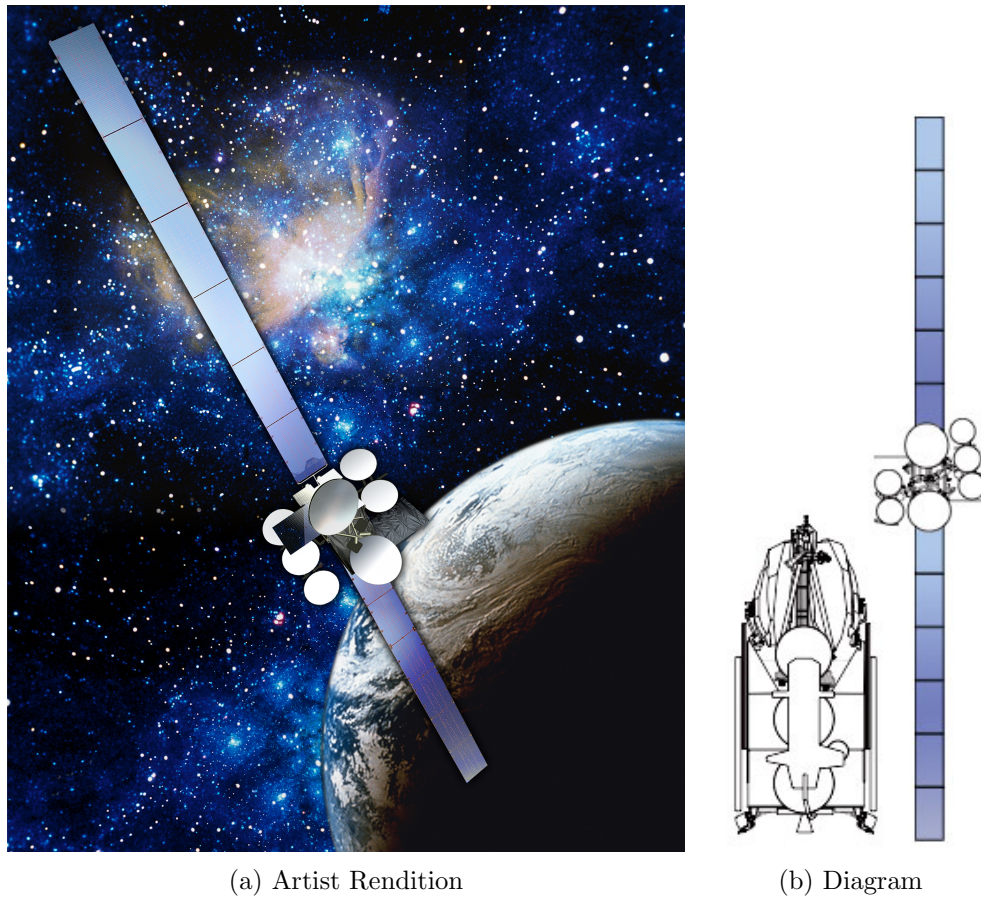


Figure 3.5: DirecTV-10 and DirecTV-12 [11].

The key properties of the five satellites are as follows:

- Galaxy-3C: This satellite has a length of 48 m. It has two large elements attached symmetrically to the body. Its large reflectors are similar to Spaceway-1 and Spaceway-3.
- Spaceway-1 and Spaceway-3: These two satellites have a length of 41 m. There is a single large nadir-facing element with two smaller elements extending off the body. Two large reflectors are attached to two of the body surfaces.
- DirecTV-10 and DirecTV-12: These two satellites also have a length of 48 m. They have a total of seven elements attached to the body at

varying angles. The reflectors are smaller than the other Boeing 702-HP bus variants.

3.4 Data Collection Procedures

This section describes the data collection procedures that were used throughout the observation campaign. The objective was to establish a consistent and repeatable procedure that would reduce the likelihood of systematic errors.

3.4.1 Daily Planning and Location

All data was collected on the RMCC campus in Kingston, Ontario. Observations were conducted from a temporary facility and all equipment had to be assembled each night prior to observations. This location provided a nearly unobstructed view of the entire sky which reduced the time required for telescope alignment. However, the minimal protection meant that the equipment was susceptible to wind and other elements when in use. In order to meet the experimental objectives, data was collected on most photometric nights. Figure 3.6 shows the experimental setup at Point Frederick, RMCC Kingston.



Figure 3.6: Experimental setup at RMCC Kingston.

The three factors considered prior to conducting observations were cloud cover, atmospheric transparency, and atmospheric seeing. A clear sky for the duration of an observation period was the basic meteorological requirement. Atmospheric transparency is a measure of the total amount of water vapour in the air. Lower transparency nights required longer exposure times. In addition, low atmospheric transparency was typically associated with high humidity levels which made it difficult to keep the optics free from moisture. The temperature-dew point spread was monitored throughout the night to ensure humidity levels were acceptable.

Finally, atmospheric seeing occurs when the reflected light from the satellite travels through turbulent regions of air with varying indices of refraction. This causes the photons to strike slightly different regions of the focal plane. The resulting image, which is known as a seeing disk, limits the resolving power of the telescope [4]. There were several instances where the meteorological conditions deteriorated during the night and observations had to be suspended. Increased cloudiness near the FOV or high humidity was usually the cause of these deteriorating conditions.

3.4.2 Bias, Dark, and Flat Field Images

A bias image is a zero-duration exposure that is used to measure the floor level of signal present in each pixel. CCDs are designed so that each pixel has a bias level between several hundred and several thousand ADUs. The exact value varies by manufacturer. If this bias was not used then a zero-duration exposure would have a value distributed about a mean of zero. The purpose of the bias is to avoid the possibility of negative pixel values in an image by introducing an offset to each pixel. Although the mean bias level of a CCD can drift slowly over many months, it is known to remain stable on a night-to-night basis [28]. Thus, a master bias frame was created near the beginning of the observation campaign and used for all data reduction.

Dark current results from thermal noise and is dependent on temperature. To reduce the dark current to a manageable level most CCDs are cooled during operation. As such, the CCD was cooled to a temperature of -10°C during all observations. At this temperature the dark current was predicted to be < 0.002 electrons per second per pixel [27]. Each night, after the equipment was aligned, a series of ten 60 second dark exposures were taken. This exposure time was selected because it was longer than the exposure times required for

standard star and satellite images. A master dark image was created from the ten exposures and used during data reduction.

Flat field images were used to remove pixel-to-pixel variations, optical aberrations, and small dust particles present in the optical system. When taking the flat field images the objective was to uniformly illuminate each pixel with a source that had similar spectral properties as the object being observed. In this case, the objects are the night sky, stars, and satellites. Exposure times were selected so that pixels were filled to half of their full well capacity, which was between 20,000 and 30,000 ADUs [27].

Twilight flats were used for all data reduction. Each evening there was a short period after the Sun had set where no stars were visible. It was also dark enough during this period that the CCD wasn't saturated with the sky background. The flat field images were taken during this period with the telescope pointed in the opposite direction of the sunset at an elevation of approximately 70° . This region of the sky was generally the most uniform during the twilight period. A minimum of 10 exposures per filter were taken while ensuring the background level remained between 20,000 and 30,000 ADUs. A master flat was created for each filter for use during data reduction. Figure 3.7 shows an example of a master flat image. The large concentric rings were caused by optical aberrations and the smaller rings were caused by unfocused dust particles.

3.4.3 Standard Star Exposures

Photometric measurements of several standard stars were taken for the purpose of calculating the nightly zero points for all colour bands. These zero points were used to convert the instrumental magnitudes to apparent magnitudes in the Johnson system. During a night of observations, the airmass through which each satellite cluster was observed remained constant at 1.71 and 1.85, where 1 airmass is at zenith. Standard star observations were planned so that each star was observed through the same airmass as the satellite group being observed that night. This was done by selecting standard stars that were in the same region of the sky as the satellites and then using *TheSkyX* software to determine the precise time when they would be at the desired airmass.

Normally, 2 - 5 standard stars were observed during the 1 - 2 hours prior to satellite observations. It was preferred to observe the standard stars just prior

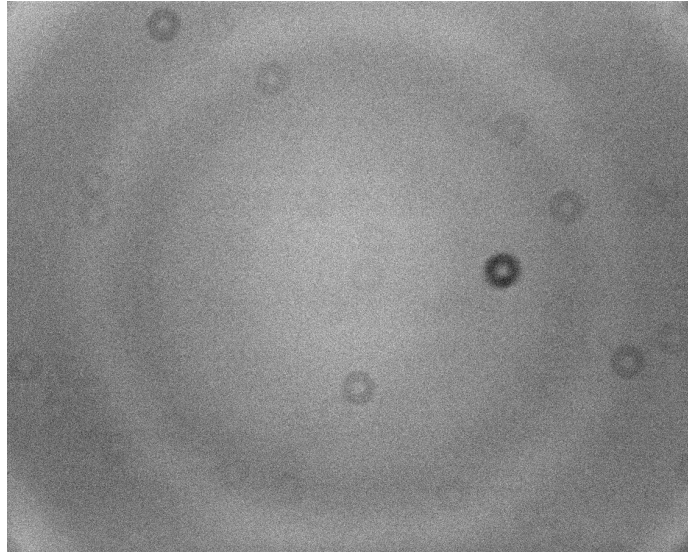


Figure 3.7: Example of a twilight flat raw image.

to the beginning of satellite observations because atmospheric seeing made any observations difficult during the hour after sunset. When the standard star was at the desired airmass several exposures with each filter were taken while the telescope was operating in sidereal tracking mode. In most cases, it was possible to take all exposures when the standard star was within ± 0.01 of the desired airmass. All standard stars were selected from Landolt's *UBVRI Photometric Standard Stars Around the Celestial Equator* [29]. Landolt's measurements are widely-used to convert instrumental magnitudes to the Johnson standard system.

3.4.4 Satellite Exposures

The two groups of satellites were observed on a rotating schedule unless poor meteorological conditions were encountered. The TLEs, which were obtained prior to observations, were used to locate the satellites. After standard star observations were complete, the telescope was slewed to the predicted location of the satellites and they were manually centered in the detector's FOV. The telescope then remained at a fixed azimuth and elevation for the duration of satellite observations. Although several of the satellites moved within the field of view during observations, they always remained in it. Simple algorithms were developed to track the location of all the satellites within an image.

Maintaining a suitable SNR was the primary task during satellite observations. This was done by manually controlling the CCD's exposure times, which varied by optical filter. An effort was made to obtain the best possible temporal resolution by keeping the exposure times as short as possible. Monitoring the SNR for each satellite was initially a challenge during short exposures. A script was written to monitor peak signal and instrumental magnitude of the observed satellites. The magnitude was plotted during satellite observations and proved to be a useful tool for monitoring the satellites' light curves. This script was also used to identify stellar streaks near the observed satellites. Figure 3.8 shows a screen capture of the monitoring script. It was used alongside the raw images to monitor the data during satellite observations.

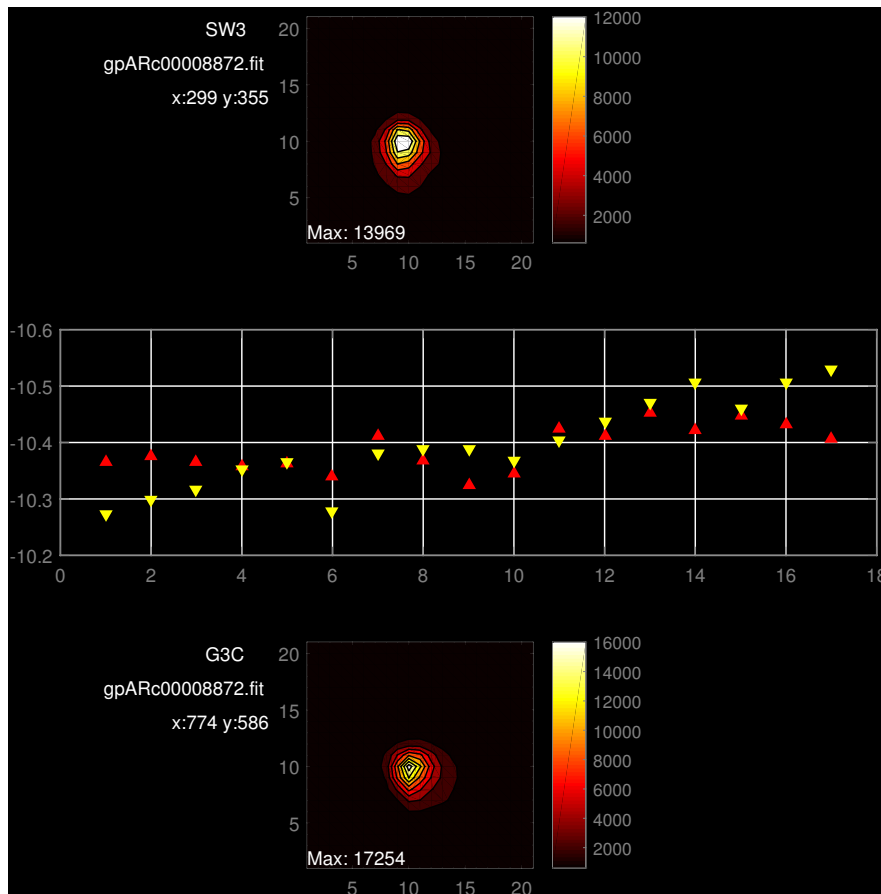


Figure 3.8: Screen capture of the data monitoring script.

4 Data Reduction Procedures

This chapter explains the procedures necessary to extract usable data from a raw image. Initially, the instrumental signature from the telescope and CCD detector are removed from each image. Next, an instrumental magnitude is calculated for each object of interest. Finally, the instrumental magnitude is converted to a standard system through the use of calibration stars. This chapter also addresses the sources of uncertainty associated with each measurement.

4.1 Image Pre-Processing

The objective of image pre-processing was to remove the instrumental signature from all standard star and satellite images. The National Optical Astronomy Observatories' (NOAO) Image Reduction and Analysis Facility IRAF software package was used for all image pre-processing. At the start of the observation campaign a master bias image was created from 100 bias images using IRAF's *zerocombine* task which was used during all image pre-processing. Figure 4.1 shows the distribution of the master bias image used for all data processing. The mean value of this distribution was subtracted from all images using IRAF's *ccdproc* task.

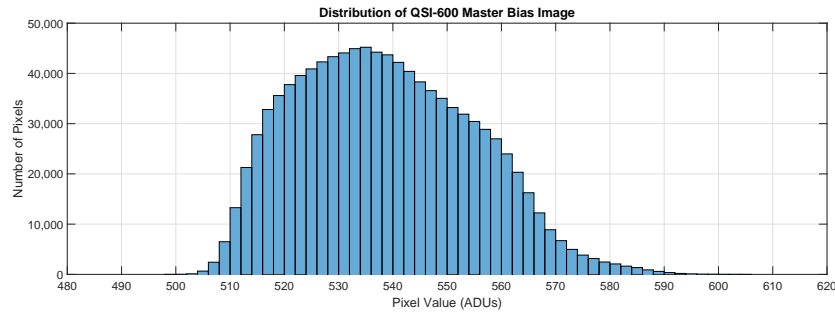


Figure 4.1: Histogram of the master bias image used for data reduction.

IRAF's *darkcombine* task was used to create a master dark image from the 10 dark exposures taken each night. The dark current was then removed from each image using *ccdproc*. All dark images were exposed for 60 seconds, which was longer than any standard star or satellite image. The master dark image, as shown in Figure 4.2, was automatically scaled to the exposure time of each image using *ccdproc*.

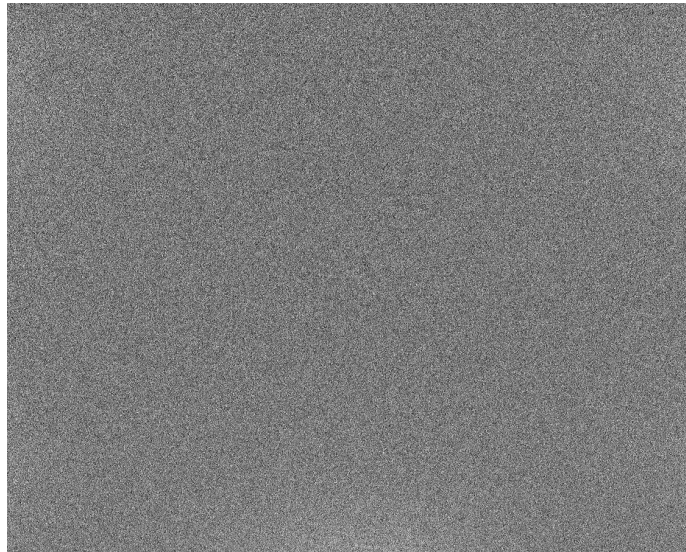


Figure 4.2: Sample dark image.

A minimum of 10 flat field images were taken with each filter on all nights where meteorological conditions permitted. There were several nights where conditions did not improve until after twilight. In these cases, the master flat images from the closest date were used. Figure 4.3 shows a surface plot

of a master flat image. The circular pattern present in the image is caused by spherical aberrations of the telescope optical system. The resulting gradient can clearly be seen in some regions of the image. The small rings in the image are unfocussed dust particles present on the CCD or filter. The spherical aberrations and dust particles caused a range of over 2500 ADUs, which was approximately 10% of the maximum range obtained for standard stars and satellites. Each night a master flat image for each filter was created using *flatcombine*. All standard star and satellite images were divided by the appropriate master flat image using *ccdproc*.

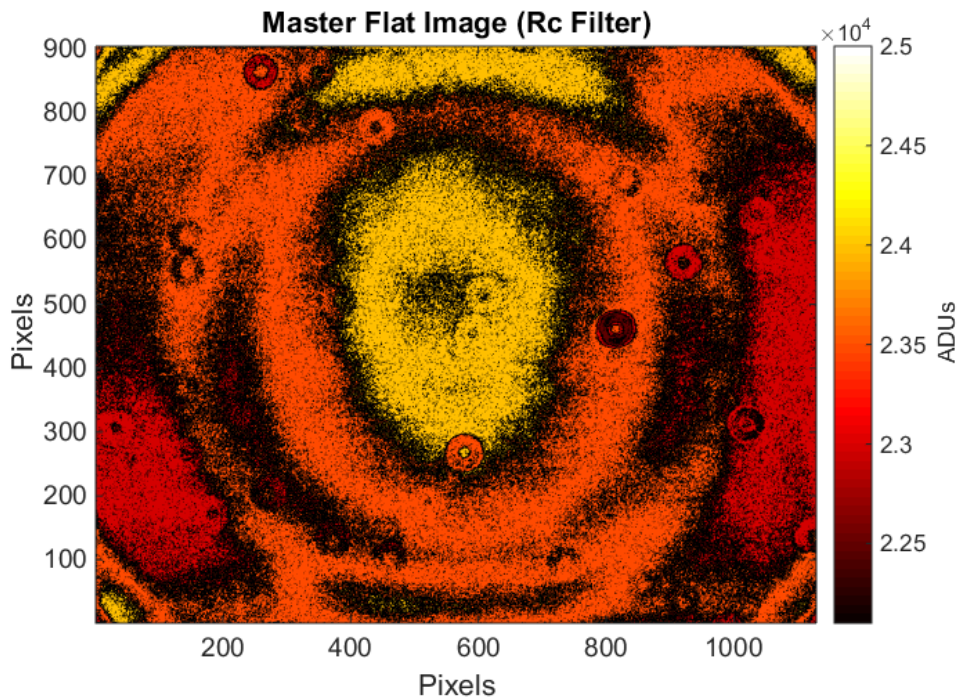


Figure 4.3: Master flat image used during data reduction.

4.2 Magnitude Extraction

Extracting instrumental magnitudes for all standard stars and satellites involved multiple steps. Initially, the standard deviation of the background sky was estimated from the raw images. This value was used during object detection and magnitude extraction. The FWHM of all objects, which was

influenced by atmospheric seeing conditions, typically varied between 3 and 5 pixels.

Once the standard deviation and FWHM were determined for each filter, IRAF's *daofind* task was used to find all satellites and standard stars within the individual images. The detection threshold was optimized to minimize the detection of faint objects that were not of interest.

IRAF's *phot* task was used to calculate the instrumental magnitudes of all detected objects. The majority of the task's parameters remained unchanged for all data processing. However, the width of the aperture and inner sky annulus were determined by the FWHM on a given night. Figure 4.4 shows a diagram of the aperture used for the instrumental magnitude extraction of all objects. The objective when selecting the aperture size was to ensure a minimum diameter of twice the FWHM. It was found that the likelihood of a bad pixel increased greatly with apertures larger than this. The inner radius of the sky annulus was 5 pixels larger than the aperture. The sky annulus, which was used to determine the background sky signal, had a radius of 5 pixels.

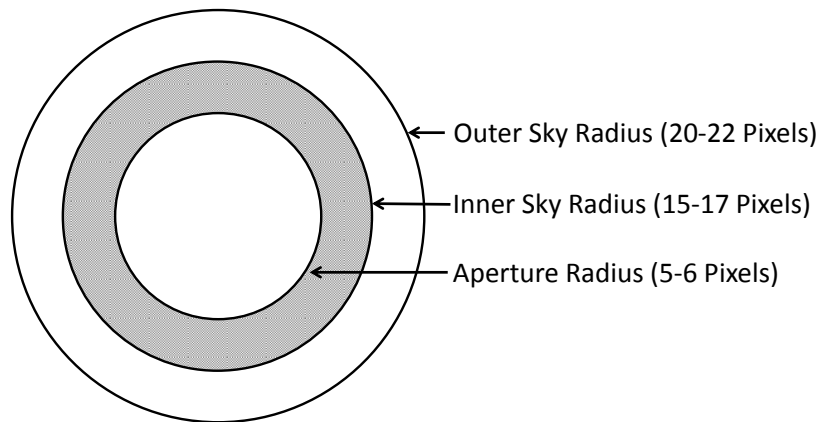


Figure 4.4: Aperture and background sky annulus used for data reduction.

The instrumental magnitude (m_{inst}) of a detected object, as calculated by IRAF, is expressed mathematically as:

$$m_{inst} = zmag - 2.5 \log_{10} \left(\frac{N_{ap} - A_{ap} C_{sky}}{t_{exp}} \right) \quad (4.1)$$

where N_{ap} is the number of counts within the aperture, A_{ap} is the area of the aperture in pixels, C_{sky} is the background sky signal in counts per pixel per second, and t_{exp} is the exposure time in seconds. The nightly zero point is represented by $zmag$. If the instrumental magnitude is all that is required then a value of zero is used for $zmag$. Otherwise, the instrumental magnitude is converted to apparent magnitude using photometric standard stars.

4.3 Photometric Standard Stars

Stars for which high-accuracy flux measurements exist in several bands are known as standard stars. They are often used as calibration sources to convert an instrumental magnitude to an apparent magnitude. The widely-accepted Landolt photometric standard stars were used during all data collection [29]. Appendix A shows the complete list of Landolt photometric standard stars observed and the dates for which they were used. It was preferred to select stars with a magnitude brighter than 10 so that all exposures could be taken within the 1 - 2 minute period when they were at an azimuth and elevation equal to the satellite group being observed that night. This ensured that they were being observed through a similar airmass. Each night, between 1 and 5 stars were used for zero point calculations. A minimum of 3 exposures per star were taken with each filter. The nightly zero point was calculated for each band taking the mean value of the differences between the instrumental and published magnitudes for each standard star. The standard deviation of these same values represented the uncertainty in the zero point. The nightly zeropoint, or $zmag$, was calculated for each band using:

$$zmag_{(B,V,Rc,Ic)} = \frac{(m_{Landolt_1} - m_{Inst_1}) + \dots + (m_{Landolt_n} - m_{Inst_n})}{n} \quad (4.2)$$

where $m_{Landolt}$ is the published magnitude, m_{Inst} is the instrumental magnitude, and n is the measurement under consideration.

Figure 4.5 shows all calculated zero points and their associated standard deviation for all bands. The uncertainty of each zero point was typically less than ± 0.05 magnitude. Larger uncertainties mostly resulted from poor seeing conditions which made instrumental magnitude extraction more difficult. There were also instances early in the observation campaign where low SNR values resulted in a greater uncertainty. The apparent magnitude was then calculated by using the results from Equation 4.2 with Equation 4.1.

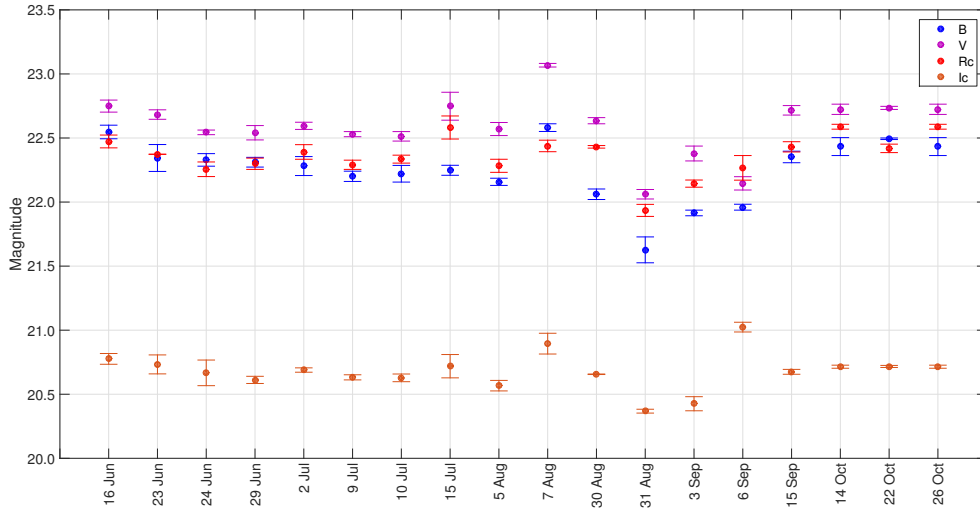


Figure 4.5: Nightly zero points for all bands.

4.4 Colour Indices

A colour index is the difference between the apparent magnitudes, or the ratio of flux, measured in two colour bands. When multiple colour indices are calculated they can be used to give an indication of the shape of an object's spectrum [4]. Within the Johnson-Cousins photometric system, the B-V, B-R, B-I, V-R, V-I, and R-I colour indices are commonly used. By convention, the longer wavelength band is subtracted from shorter wavelength band. As a result, a larger colour index value indicates a greater relative intensity at longer wavelengths and a smaller value indicates a greater relative intensity at shorter wavelengths. If the colour indices are plotted alongside a satellite's light curve then it is possible to correlate colour index variations with significant light curve features. Alternatively, the entire population of colour indices for a given night can be examined to determine statistical trends.

All satellite and photometric standard star images were taken while continuously cycling through the colour filters which meant that there was always a time difference between the images for the different colour bands. As a consequence, calculating a colour index at a discrete time required interpolation. Matlab’s Piecewise Cubic Hermite Interpolating Polynomial (PCHIP) function was used for this purpose. The objects in the images taken in the B-band typically had lowest SNR, especially during the beginning of the night and, as a result, most datasets had fewer B-band images. When calculating the nightly colour indices for each satellite all data were interpolated to the B-band time axis.

To illustrate how individual measurements were interpolated, Table 4.1 shows typical exposure times at the beginning of the night when the satellites were their faintest. The elapsed time represents the interpolation time. As an example, the Rc-band data point is interpolated 10 seconds backwards to the time that the B-band exposure was finished to calculate the B-R colour index at a discrete point. PCHIP interpolated to the previous or to the next B-band data point to obtain the best fit.

	B	V	Rc	Ic
Exposure Time (s)	12	6	4	10
Elapsed Time (s)	12	18	22	32

Table 4.1: Example exposure and elapsed times.

When exposure times were short data points were interpolated by several seconds. However, when the satellites were fainter over 30 seconds was required to cycle through all four filters. Figure 4.6 shows V-band, Rc-band, and Ic-band data points interpolated to the B-band time. The time offset between each band’s interpolated and non-interpolated data can be seen. Fortunately, when the significant light curve features were being observed the exposure times were much shorter, in many cases less than a second, which greatly reduced the interpolation times.

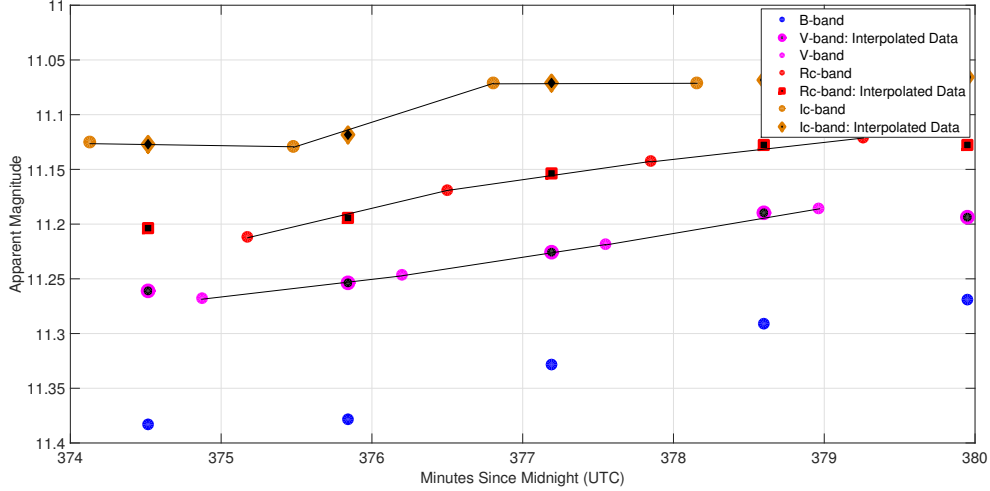


Figure 4.6: Raw and interpolated data points for all bands.

4.5 Error Analysis

This section summarizes the errors present in all data presented in this thesis. CCD measurement errors and nightly zero point uncertainties constitute the total error.

4.5.1 Instrumental Magnitude Uncertainty

The instrumental magnitude uncertainty is a function of the SNR of each photometric measurement made using a CCD. The SNR for each measurement is calculated with the following expression:

$$SNR = \frac{N_*}{\sqrt{N_* + n_{pix}(N_S + N_D + N_R^2)}} \quad (4.3)$$

where N_* is the number of photons collected from the object of interest (satellites in this case), n_{pix} is the number of pixels upon which the object's photons are incident, N_S is the total number of photons per pixel from the background sky, N_D is the total number of dark current electrons per pixel, and N_R is the total number of electrons per pixel resulting from readout noise [28]. The total signal is expressed by N_* , which is the product of the CCD's gain and measured ADUs, whereas the noise, or uncertainty, is expressed by the terms in the denominator of Equation 4.3. The rate at which photons impinge upon the CCD detector is described by the Poisson distribution. Therefore,

the uncertainty associated with a single measurement of N_* is its standard deviation, which is $\sqrt{N_*}$ [4]. If N_* is the dominant source of uncertainty then Equation 4.3 simplifies to:

$$SNR \cong \sqrt{N_*} \quad (4.4)$$

Equation 4.3 proved to be a valid approximation of SNR for the data collected for this thesis. While the SNR gives an indication of the quality of a measurement, it does not address uncertainty. The uncertainty for a photometric measurement, where N_* is the dominant source of uncertainty, is expressed mathematically as:

$$\sigma_{phot} \cong \frac{1.0857}{\sqrt{N_*}} \quad (4.5)$$

where σ_{phot} is the standard deviation of the measurement after it has been converted to a magnitude. The constant in the numerator is a correction term which allows the error to be expressed in magnitude rather than flux. Equation 4.5 was used to calculate the uncertainty associated with all photometric measurements.

4.5.2 Combined Uncertainty

The total uncertainty present in each apparent magnitude presented in this thesis is the sum of the photometric uncertainty (σ_{phot}) and standard deviation of the calculated nightly zero point (σ_{zmag}). This total uncertainty (σ_{ap}) is expressed as:

$$\sigma_{ap} \cong \sigma_{phot} + \sigma_{zmag} \quad (4.6)$$

Finally, the uncertainty present in each colour index is simply the root mean square of the errors for the two bands being considered. For example, the uncertainty for the B-V colour index is expressed as:

$$\sigma_{B-V} \cong \sqrt{\sigma_{apB}^2 + \sigma_{apV}^2} \quad (4.7)$$

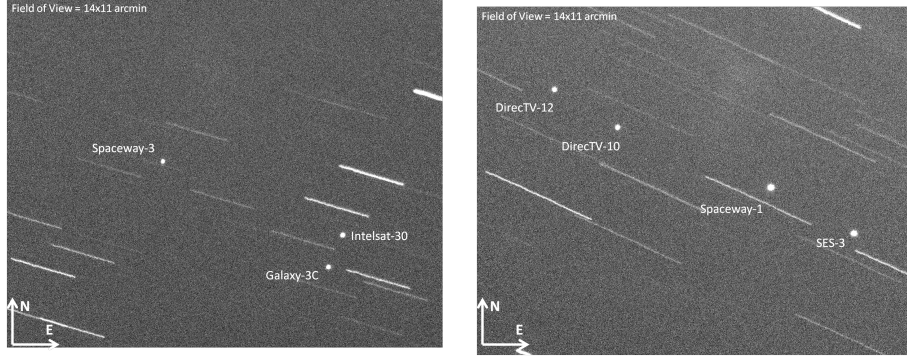
where σ_{B-V} is the total uncertainty for the B-V colour index, and σ_{apB} and σ_{apV} are the total errors for the B and V-bands.

All photometric, zero point, and colour index uncertainties are shown in Appendix B.

5 Seasonal Light Curve Variations and Specular Reflection Analysis

This chapter examines the seasonal variations of the satellites' light curves. The main effort is to determine if identical satellites exhibit similar light curve variations. Initially, the light curves for the entire season are shown together for each satellite. The purpose of this is to highlight the variations in brightness and structure as the seasonal illumination geometry changes. Next, an analysis of the specular reflections from specific satellite surfaces is presented in an effort to understand the causes of the seasonal light curve variations.

The two groups of GEO satellites were observed on a rotating schedule on most photometric nights between late June and late October 2015. Figure 5.1 shows raw images of the two groups of satellites observed for this thesis. The satellites appear as point sources and the background stars appear as streaks. This is because GEO satellites are nearly motionless, relative to a ground-based observer, and stars move through the sky as the Earth rotates. It is not possible to obtain resolved images of GEO satellites because of their high altitude. Thus, photometry measures the sum of the reflected light from all satellite surfaces that is incident upon the CCD at a given time.



(a) Group A satellites located at a longitude of $95^{\circ}W$, azimuth of 205° , and elevation of 36° .

(b) Group B satellites located at a longitude of $103^{\circ}W$, azimuth of 215° , and elevation of 33° .

Figure 5.1: Raw images of Group A and Group B satellites.

5.1 Seasonal Light Curve Variations

Figures 5.2 - 5.6 show the seasonal light curves for Spaceway-3, Spaceway-1, Galaxy-3C, DirecTV-10, and DirecTV-12. They are presented as a function of minutes since midnight (MSM) in coordinated universal time (UTC) to allow for a reconstruction of illumination and observational geometries. The large gaps in data seen in September and October were due to seasonal eclipses. From Table B.1, the average total error present in each V-band measurement was between 0.015 and 0.060 magnitude which is smaller than the individual data points presented here. Thus, error bars are not shown.

When examining the light curves, the trends to consider are the seasonal variations in structure and brightness, the evolution of light curve features, and the time when these features occurred. Spaceway-1 and Spaceway-3 have identical buses but Spaceway-1 was located at a more westerly longitude. As a result, it is expected that its significant light curve features will be observed later at night. This is because the Sun's easterly track, within the the satellite-centered coordinate system, causes similar illumination geometries to occur later at night for more westerly-positioned satellites. DirecTV-10 and DirecTV-12 also have identical buses but were co-located at the same orbital longitude. As such, any differences in their respective light curves are not caused by illumination geometry. Galaxy-3C had a different bus variant than the previously mentioned satellites and was co-located with Spaceway-3.

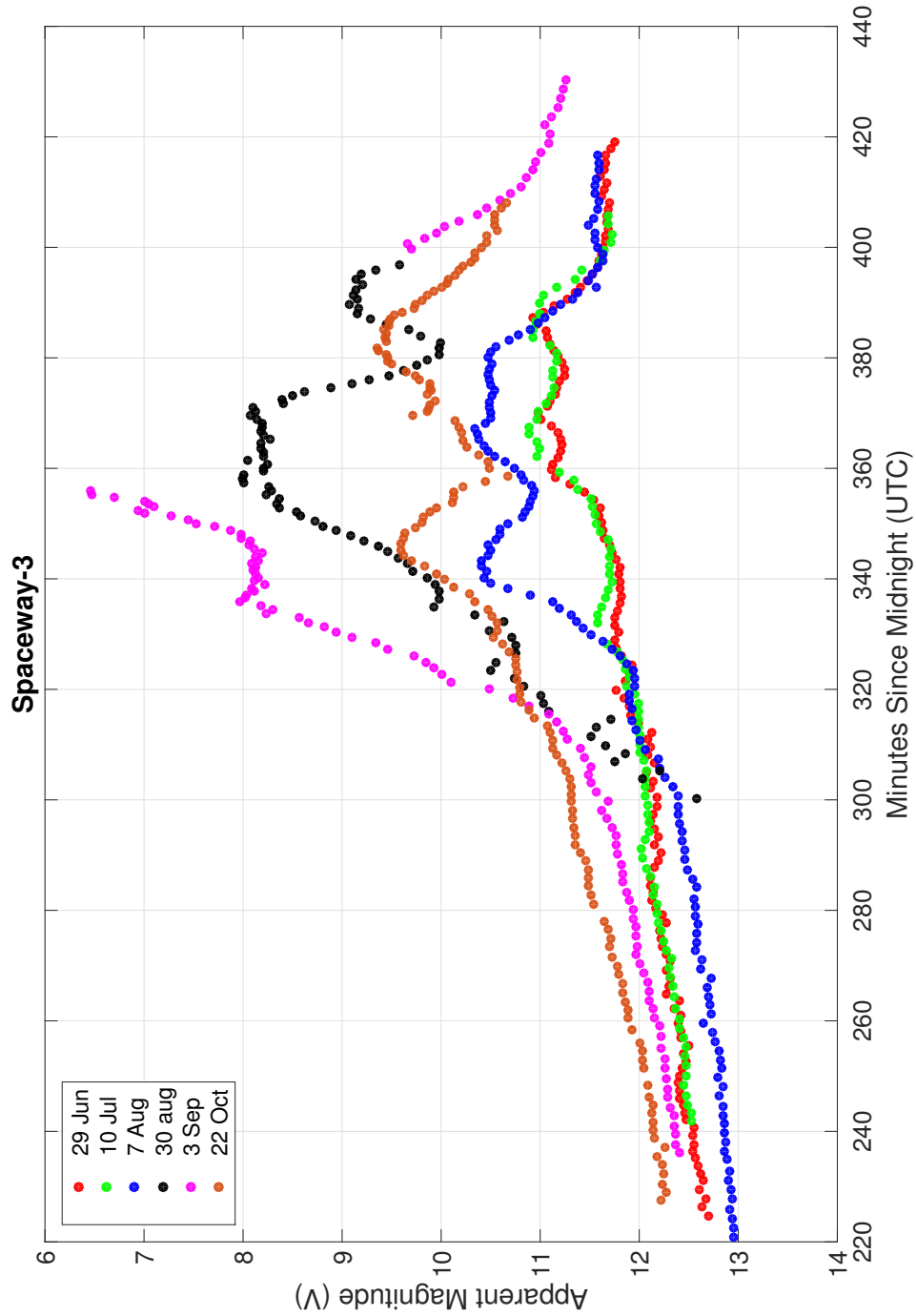


Figure 5.2: Seasonal V-band light curves for Spaceway-3.

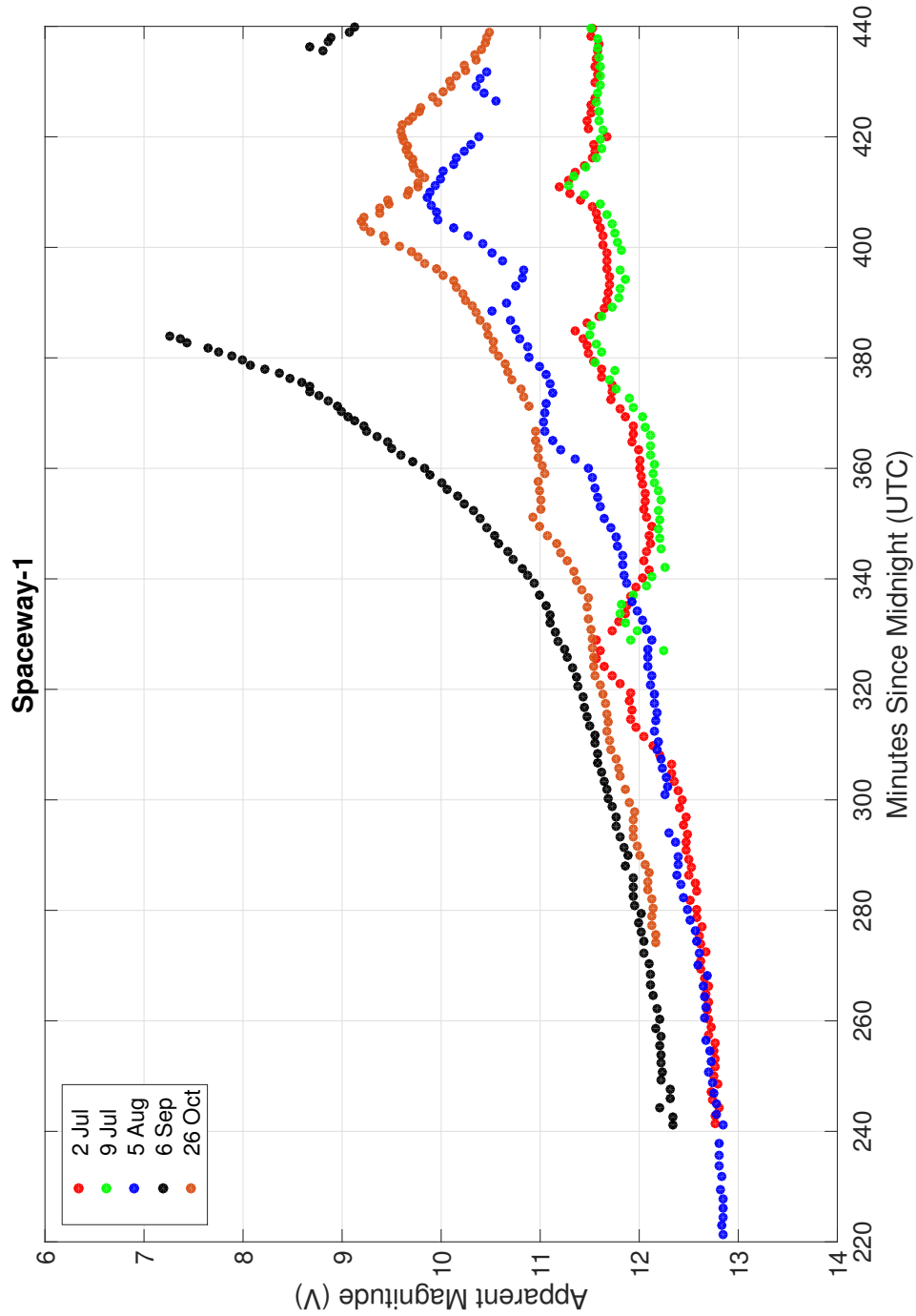


Figure 5.3: Seasonal V-band light curves for Spaceway-1.

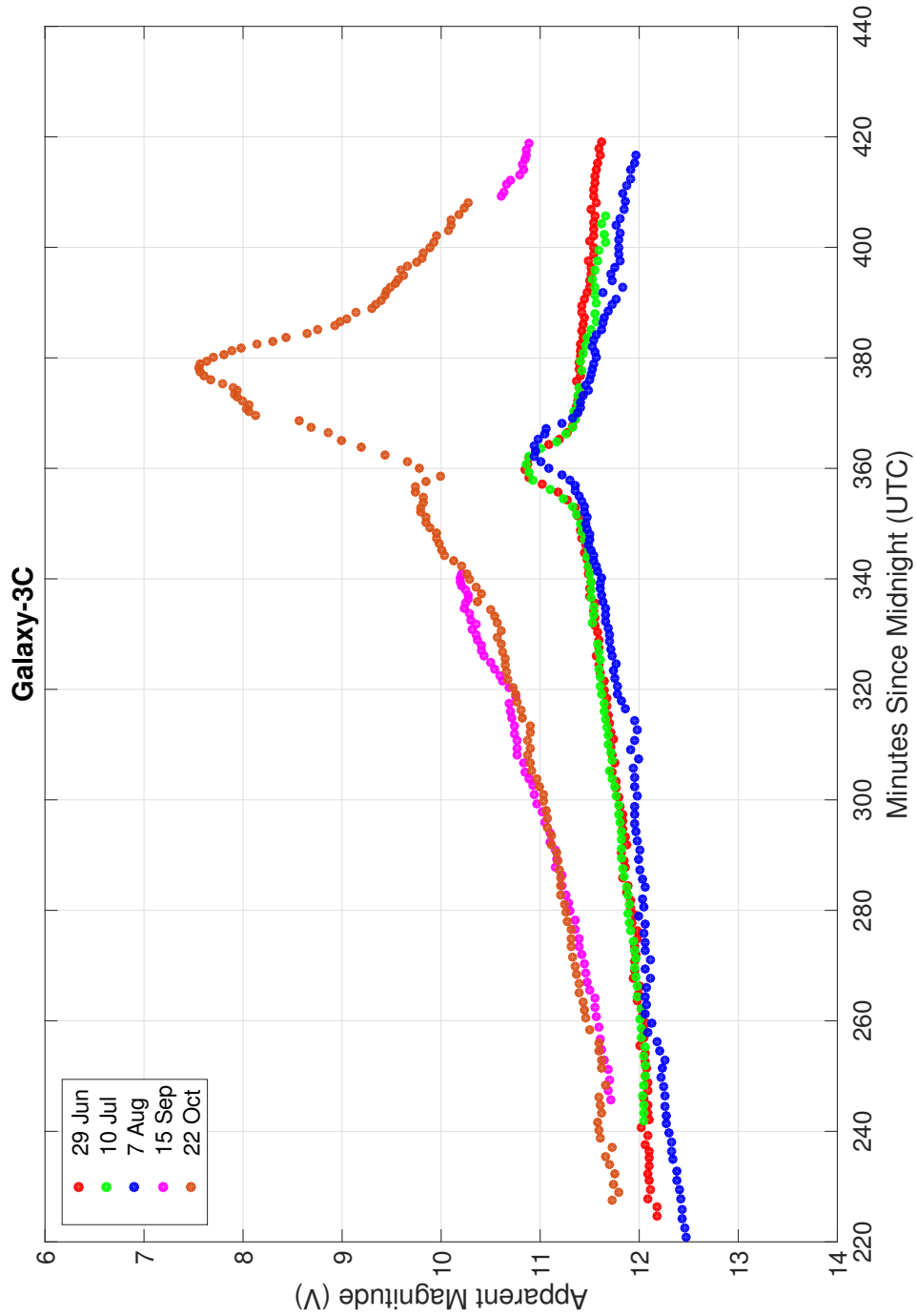


Figure 5.4: Seasonal light curves for Galaxy-3C.

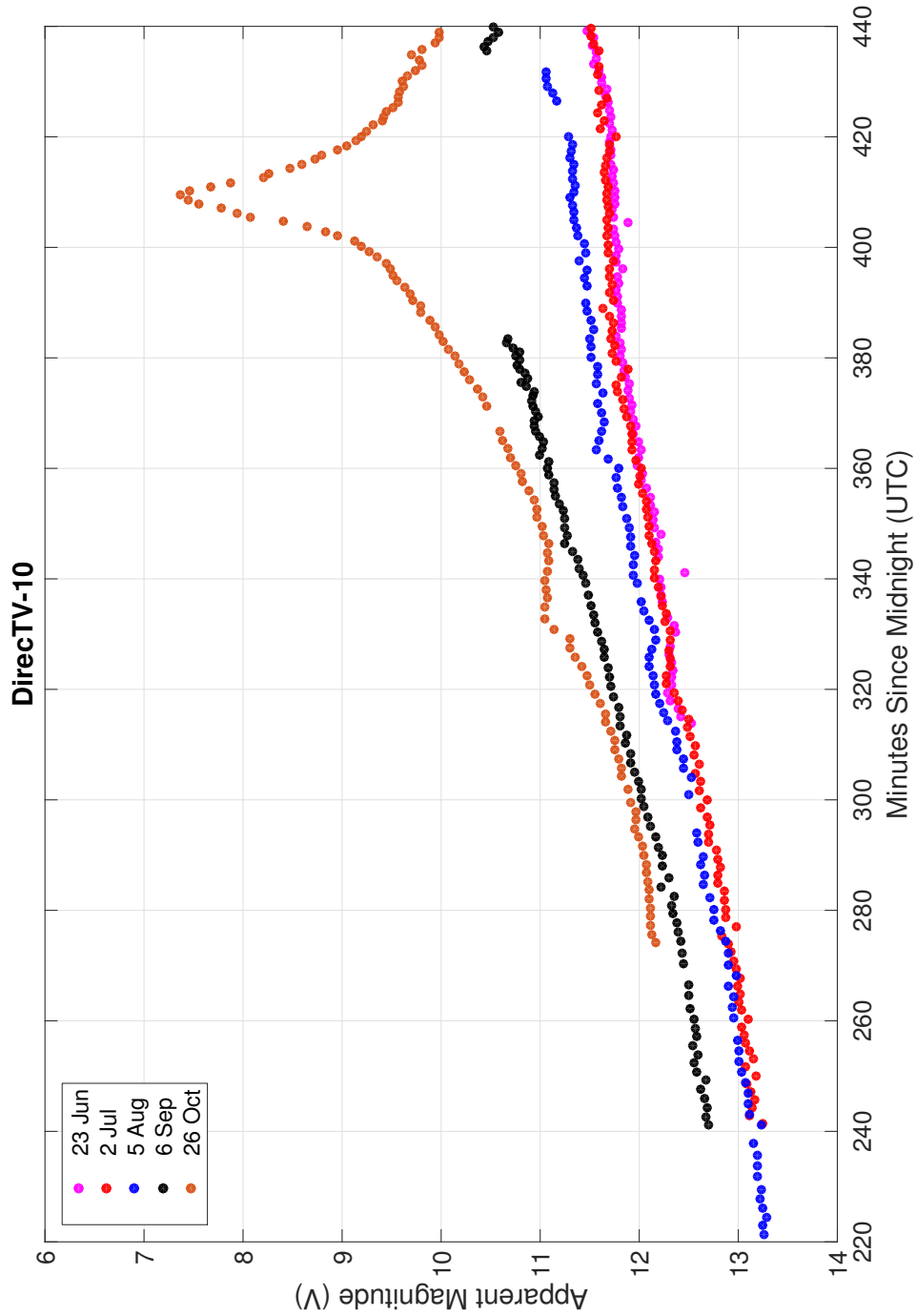


Figure 5.5: Seasonal light curves for DirecTV-10.

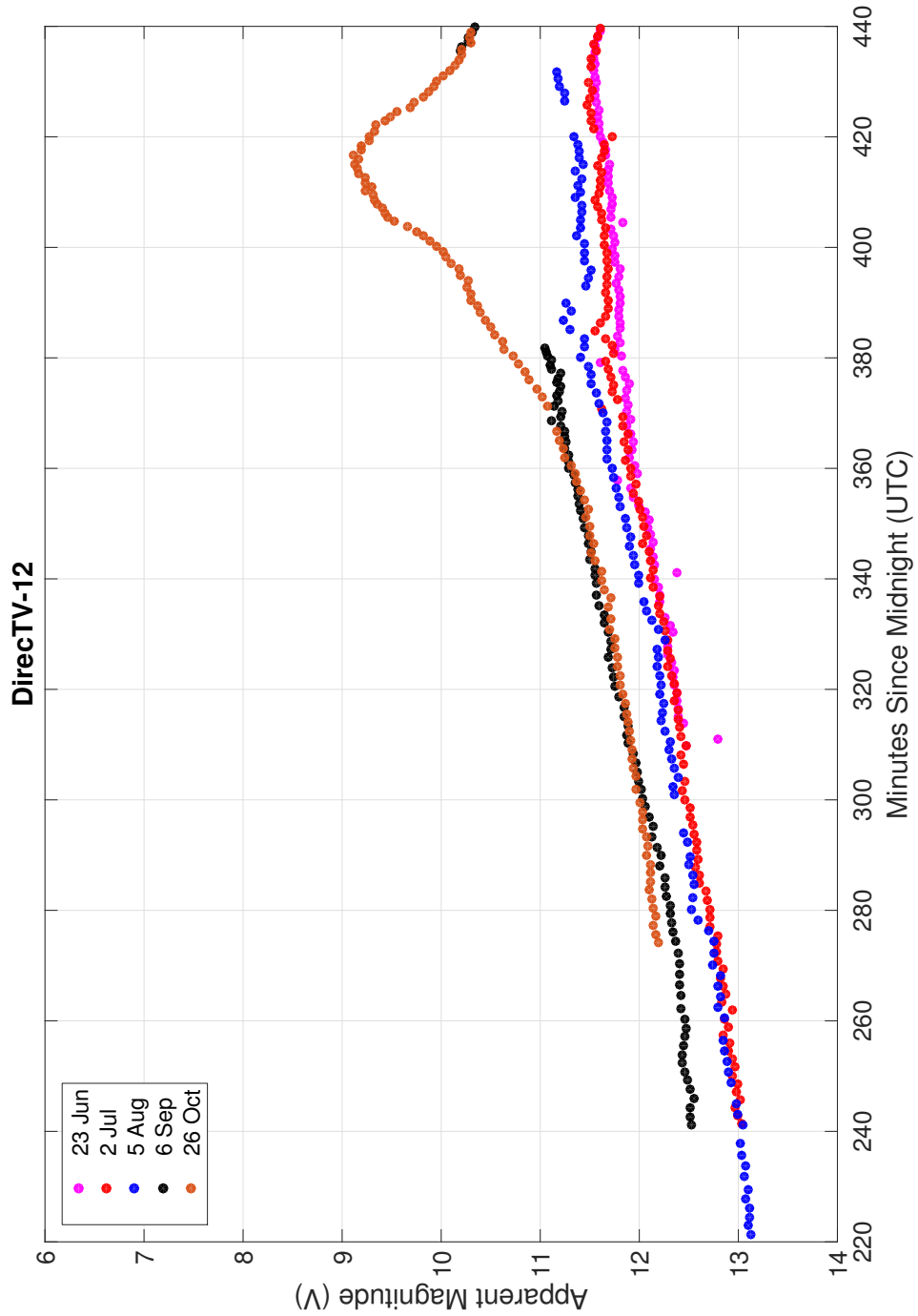


Figure 5.6: Seasonal V-band light curves for DirecTV-12.

Between late June and mid September a gradual increase in peak brightness was observed for most satellites. This was due to the Sun's decreasing elevation which resulted in smaller phase angles. In September some of the observed satellites reached their maximum seasonal brightness when they were entering or exiting eclipse periods. Other satellites reached their maximum brightness in October.

Spaceway-1 and Spaceway-3: Boeing 702-HP Type A

Significant differences were observed between the light curves of Spaceway-1 (Figure 5.3) and Spaceway-3 (Figure 5.2). In late June and early July both satellites' light curves had a multiple peak structure. However, Spaceway-1's was nearly one-half magnitude fainter and the structure was observed over a greater period. In August, a multiple-peak structure was again observed for both satellites but their overall structure was different. In early September both satellites reached their maximum seasonal brightness. The most significant difference between the two light curves was the feature observed at 340 MSM for Spaceway-3 as it steadily increased in brightness. A similar feature was not observed for Spaceway-1. In late October each satellite again exhibited a multiple peak structure that was brighter than had been observed between June and August. Although each satellite's light curves were similar in peak brightness in October, their overall structure was different.

DirecTV-10 and DirecTV-12: Boeing 702-HP Type C

Despite having the same basic bus type as the Spaceway satellites, DirecTV-10 (Figure 5.5) and DirecTV-12 (Figure 5.6) had very different light curves. Prior to October, DirecTV-10 and DirecTV-12 exhibited featureless light curves that steadily increased in brightness each night. Throughout this period both satellites were similar in brightness. After autumnal equinox, in late October, a single bright peak was observed for each satellite. DirecTV-10's single peak was nearly two magnitude brighter and occurred several minutes earlier. It also had a more distinct shape. In addition, a small feature was observed at 330 MSM for DirecTV-10 that was not observed for DirecTV-12.

Galaxy-3C: Boeing 702-HP Type B

Although Galaxy-3C (Figure 5.4) has a different variant of the Boeing 702-HP bus than the Spaceway and DirecTV satellites, its light curves are presented here as a comparison. Galaxy-3C's light curves were unchanging in brightness

and structure between late June and early August. However, by early August the single peak was observed to occur approximately five minutes later. Galaxy-3C was also much brighter in late October and its single peak occurred later. A sudden decrease in intensity was observed at 360 MSM, which was when the single peak occurred prior to October.

From the small sample presented here it is possible to conclude that identical GEO satellites do not exhibit the same seasonal light curve variations. However, the light curves for identical GEO satellites do share similar broad characteristics. For example, the Spaceway satellites both exhibited a multiple-peak structure while the DirecTV satellites exhibited a featureless light curve prior to autumnal equinox and a single bright peak thereafter.

The broad similarities observed for the light curves of identical satellites indicate that the same reflecting surfaces may be responsible for the significant light curve features. However, this is purely a qualitative assessment. Many of the light curves presented here had complex structures comprised of several bright features which were likely caused by specular reflections from various satellite surfaces and components. If the source of the various light curve features can be determined then it may be possible to compare results for similar surfaces and materials for two different satellites. This approach will be used to measure the effects of the space environment on satellite materials. Accordingly, the next section focuses on constraining the physical origin of the observed light curve features.

5.2 Specular Reflection Analysis

This section considers the specular reflections from specific satellite surfaces. The objective is to determine if the sources of significant light curve features can be constrained to reflections from either the Sun-tracking solar arrays or surfaces associated with the main body structure. The previously shown light curves indicated that the observed variations had a strong seasonal dependence. The changing illumination geometry was likely the primary reason for these seasonal variations. To illustrate this, Figure 5.7 shows the Sun's azimuth and elevation for the duration of this observation campaign. These plots are essentially the nightly tracks of the Sun within the satellite-centered coordinate system. Within this coordinate system, the Sun tracks eastward which results in a decreasing azimuth angle as the night progresses. The decreasing elevation from June until September is also evident from these plots.

Between late August and early September, the Sun's elevation decreased to an angle where nightly eclipses occurred as the Sun passed behind the Earth. After autumnal equinox, and for the remainder of the fall and winter, the Sun's elevation was negative.

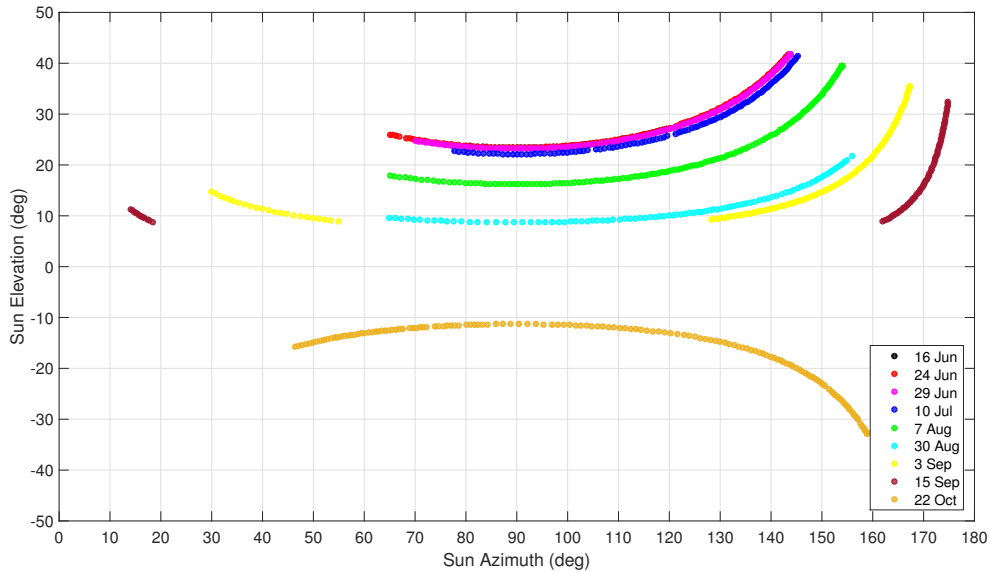


Figure 5.7: Seasonal Sun azimuth and elevation angles.

The reflections from the +Z (Nadir Pointing) body surface and the Sun-tracking solar arrays are analyzed in this section. Systems Tool Kit (STK) was used to model Sun reflection vectors from the +Z body surface and the Sun-tracking solar arrays. It was assumed that the +Z body surface was flat and that its surface normal vector pointed to the center of the Earth. External antennas, reflectors, and other elements were not considered. It was also assumed that the satellite's attitude placed the solar arrays in a North-South configuration, as seen in Figures 5.8 and 5.9, and that both solar arrays actively tracked the Sun. Figure 5.8 shows the surface normal vectors for the +Z Body and solar array surfaces. The solar arrays' movement is constrained in such a way that they can only rotate about the Y-axis. The illumination geometry shown here was typical for mid August.

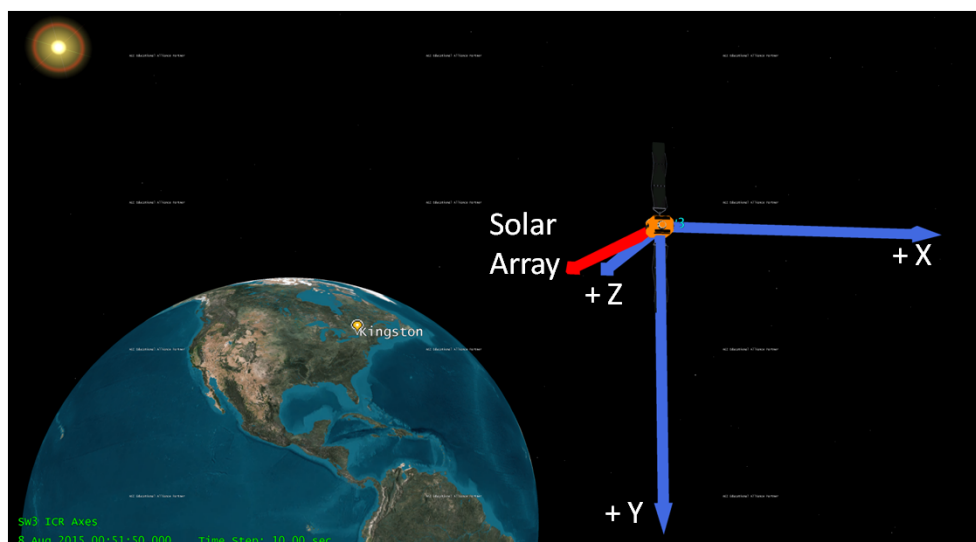


Figure 5.8: Surface normal vectors for the Sun-tracking solar arrays and satellite +Z body surface on 8 August 2015.

Sun specular reflection vectors were then created from the +Z body and solar array surface normal vectors. Figure 5.9 shows the specular reflection vectors from the +Z body and solar array surfaces. Sun and Kingston position vectors have also been included for reference.



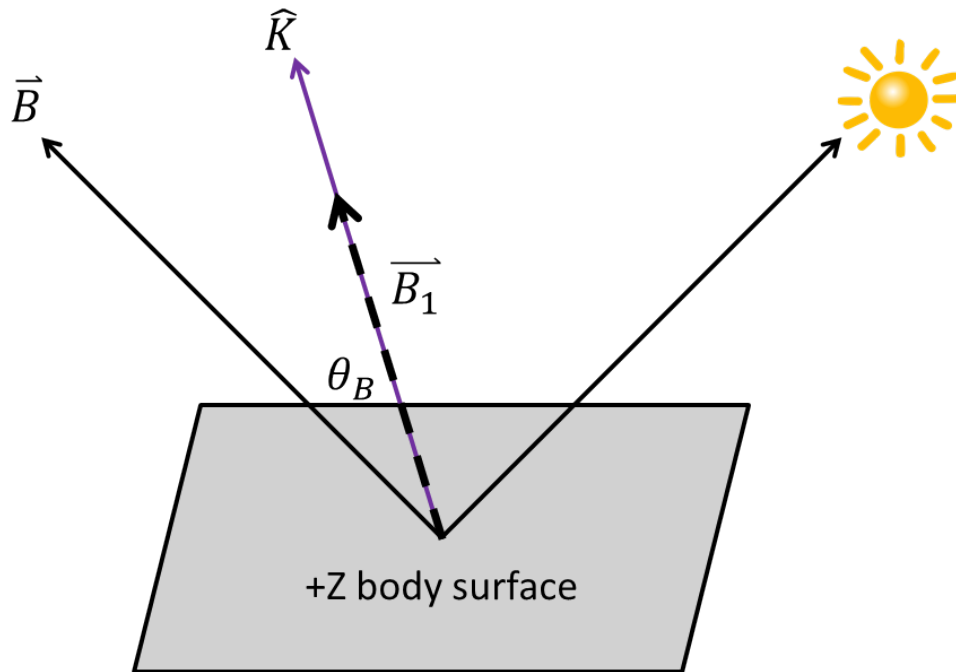
Figure 5.9: Solar array and +Z body specular reflection vectors on 8 August 2015.

A vector projection of each reflection vector onto the Kingston position vector was used to determine if the observed light curve features were caused by reflections from the +Z body surface or the solar arrays. The vector projections are expressed mathematically as:

$$\mathbf{S}_1 = (|\mathbf{S}| \cos \theta_S) \hat{\mathbf{K}} \quad (5.1)$$

$$\mathbf{B}_1 = (|\mathbf{B}| \cos \theta_B) \hat{\mathbf{K}} \quad (5.2)$$

where \mathbf{S}_1 and \mathbf{B}_1 are the solar array reflection vector (\mathbf{S}) and +Z body reflection vector (\mathbf{B}) projected onto the Kingston position unit vector ($\hat{\mathbf{K}}$). θ_S and θ_B are the angles between \mathbf{S} , \mathbf{B} , and $\hat{\mathbf{K}}$. In addition, \mathbf{S}_1 and \mathbf{B}_1 were normalized for presentation purposes. A larger magnitude for \mathbf{S}_1 and \mathbf{B}_1 indicates that θ_S and θ_B are smaller meaning that the specular reflection from the solar arrays or +Z body surface is closer to Kingston. Figure 5.10 provides a graphical representation of the +Z body surface vector projection. The solar array vector projection has similar geometry.

Figure 5.10: Diagram of the $+Z$ body surface reflection and vector projection.

5.2.1 June - August Vector Projection Analysis

Between late June and early August, the illumination geometry was such that the Sun was illuminating all observed satellites from the northern hemisphere. The peak brightness observed during this time was several magnitude fainter than what was observed in October for all satellites. Figure 5.11 shows the solar array and +Z body surface reflection vectors in early August. The illumination geometry caused the reflection vectors to point to the southern hemisphere. As autumnal equinox approached, the Sun's nightly elevation decreased which caused specular reflections closer to Kingston.

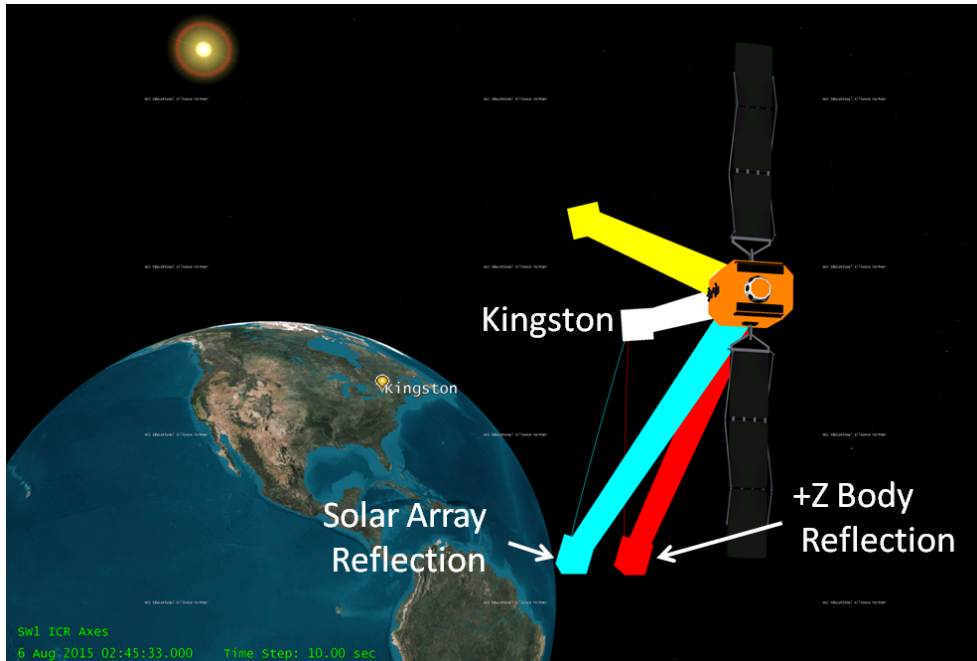
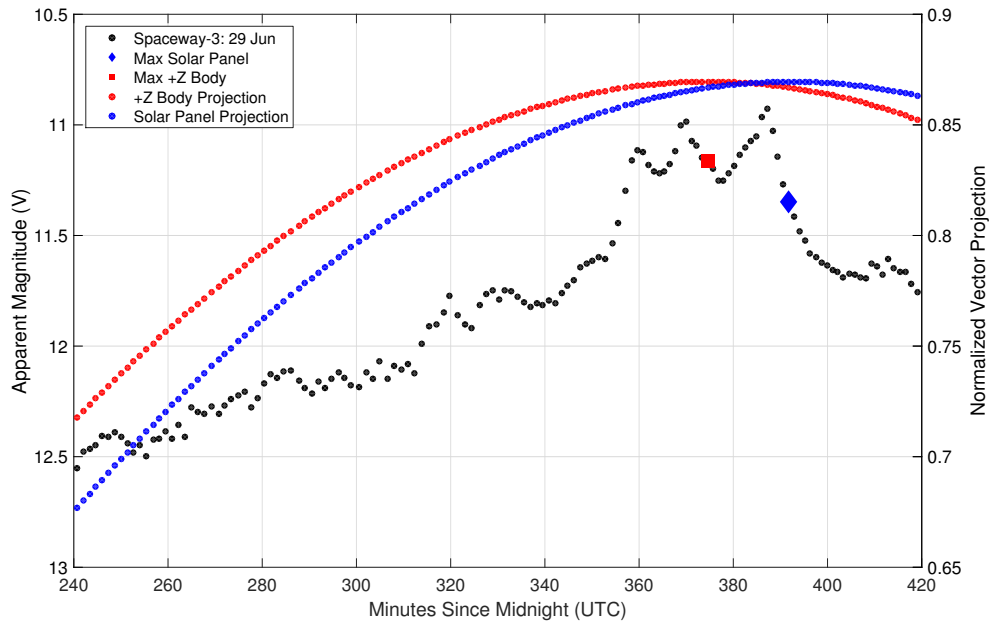


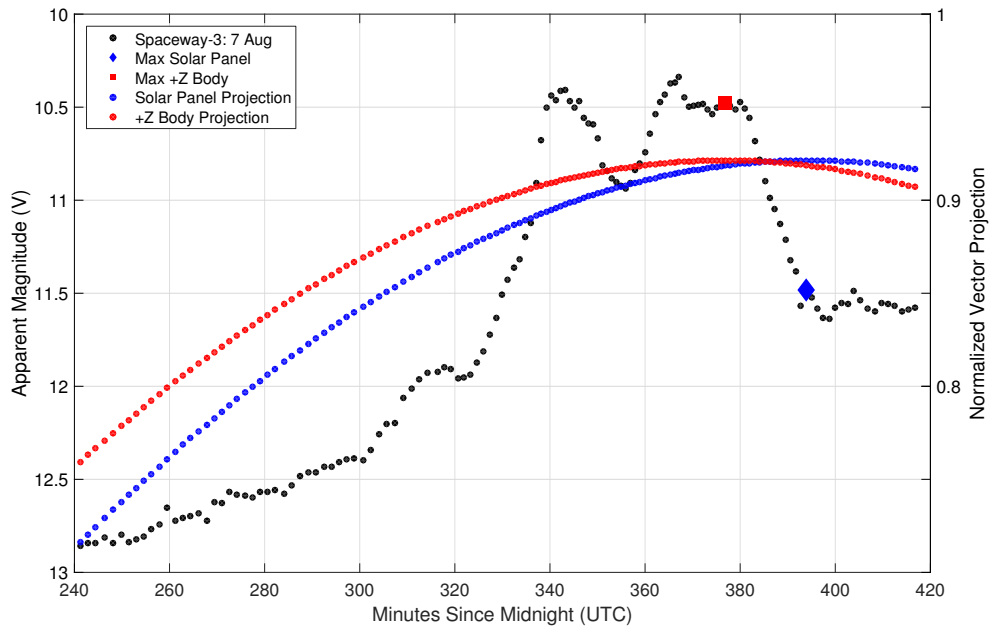
Figure 5.11: Solar array and +Z body surface reflection vectors on 8 August 2015.

Figures 5.12 - 5.14 show the normalized magnitudes of the Sun and +Z body surface projection vectors and light curves for late June and early August for Spaceway-3, Spaceway-1, and Galaxy-3C. The maximum value for each normalized projection occurred when θ_S and θ_B were at their minimum. These maximum values have been overlaid on the light curve to indicate the best modeled specular reflection from the solar arrays and +Z body surface.

5.2. Specular Reflection Analysis



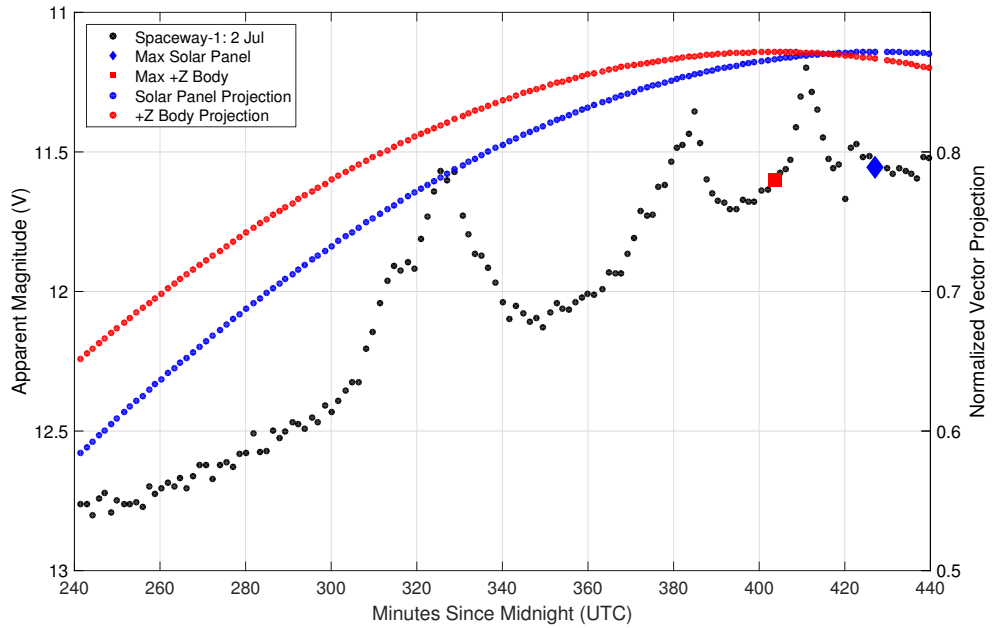
(a) Spaceway-3: 29 June 2015



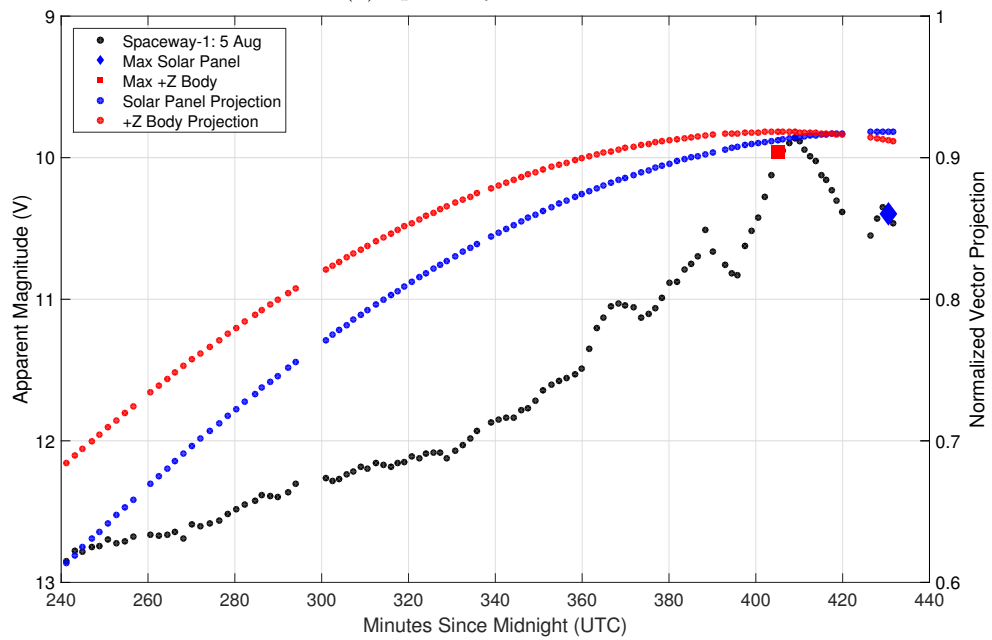
(b) Spaceway-3: 7 August 2015

Figure 5.12: Solar panel and +Z body surface vector projections for Spaceway-3 between late June and early August 2015.

5.2. Specular Reflection Analysis



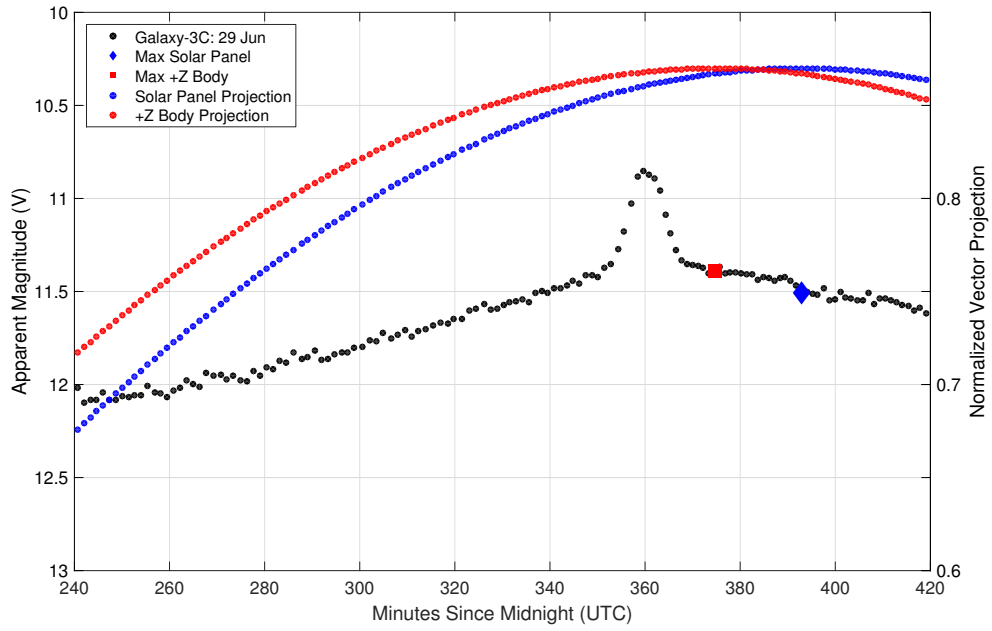
(a) Spaceway-1: 2 Jul 2015



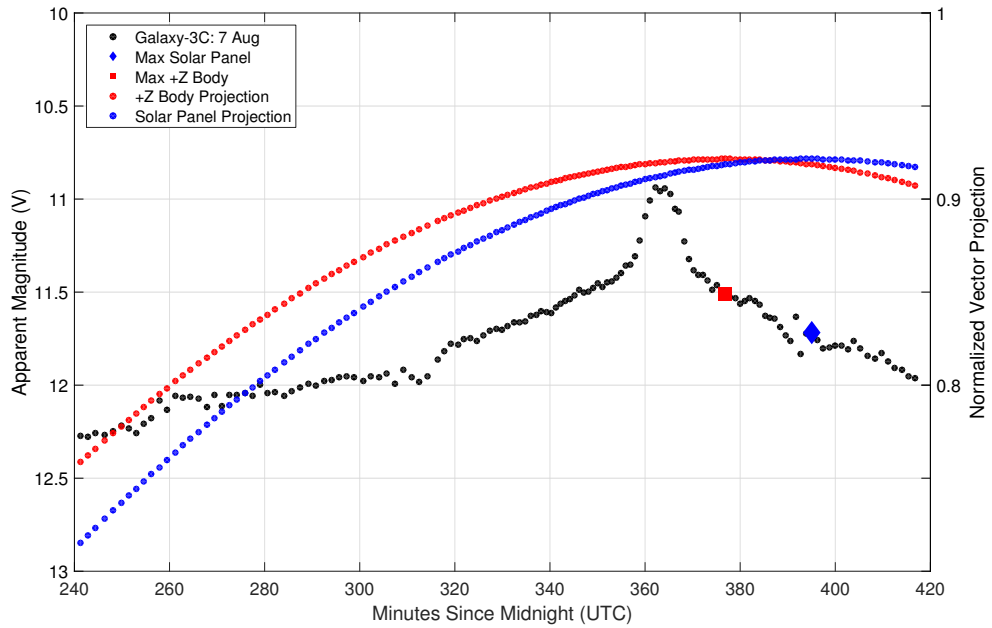
(b) Spaceway-1: 5 August 2015

Figure 5.13: Solar panel and +Z body surface vector projections for Spaceway-1 between early July and early August 2015.

5.2. Specular Reflection Analysis



(a) Galaxy-3C-1: 29 Jun 2015



(b) Galaxy-3C: 7 August 2015

Figure 5.14: Solar panel and +Z body surface vector projections for Galaxy-3C between late June and early August 2015.

5.2.2 October Vector Projection Analysis

In October the Sun was illuminating the observed satellites from the southern hemisphere. As a result, the reflection vectors from the solar arrays and +Z body surface were in the direction of the northern hemisphere. Figure 5.15 shows the solar array and +Z body reflections vectors in late October. All observed satellites were several magnitude brighter than they had been between late June and early August.

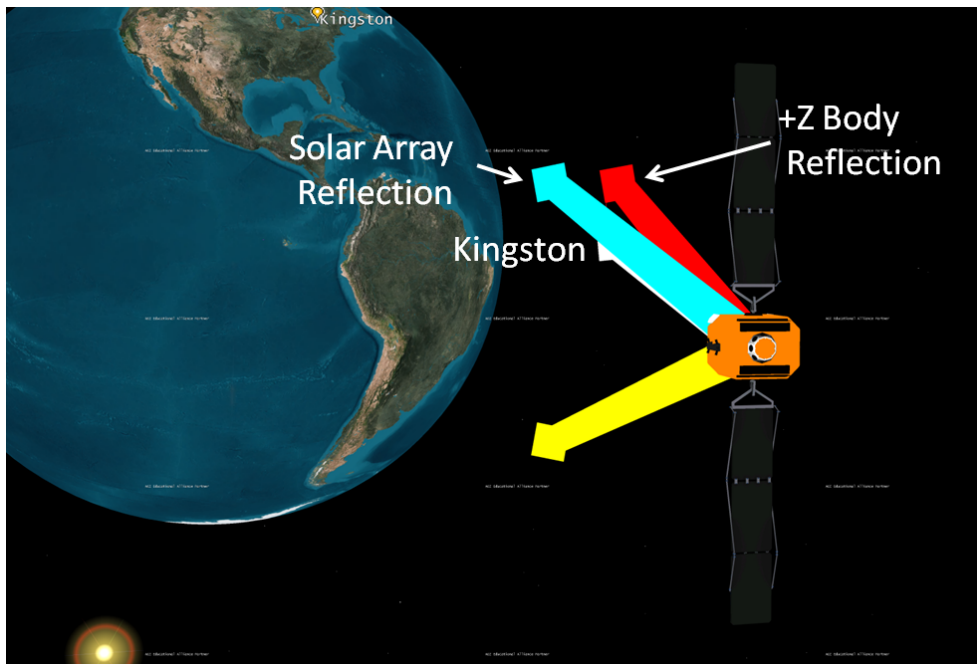
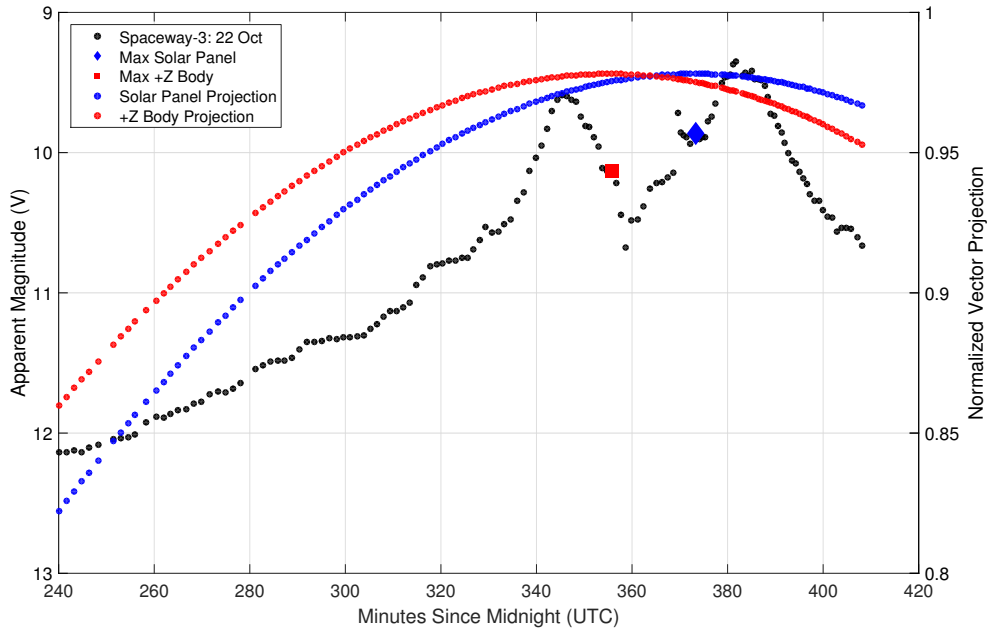


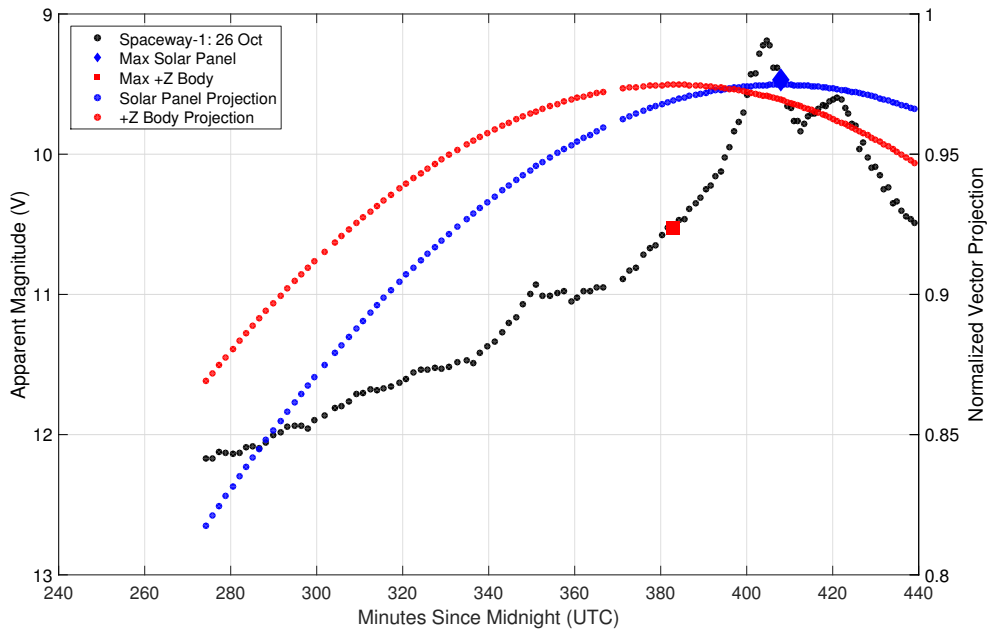
Figure 5.15: Solar array and +Z body surface reflection vectors in October.

Figures 5.16 - 5.18 show the normalized magnitudes of the Sun and +Z body surface vector projections for Spaceway-3, Spaceway-1, DirecTV-10, DirecTV-12, and Galaxy-3C in late October. This was the first time that significant light curve features were observed for DirecTV-10 and DirecTV-12. Previously, their featureless light curves gradually increased in brightness during a night of observations. The change in illumination geometry after autumnal equinox had the greatest impact on these two satellites.

5.2. Specular Reflection Analysis



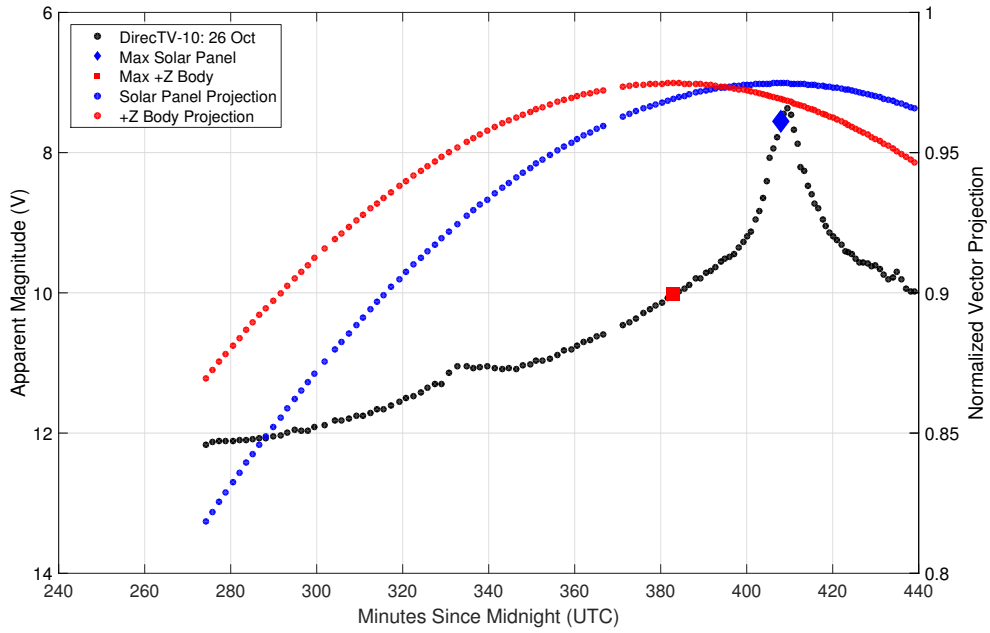
(a) Spaceway-3: 22 Oct 2015



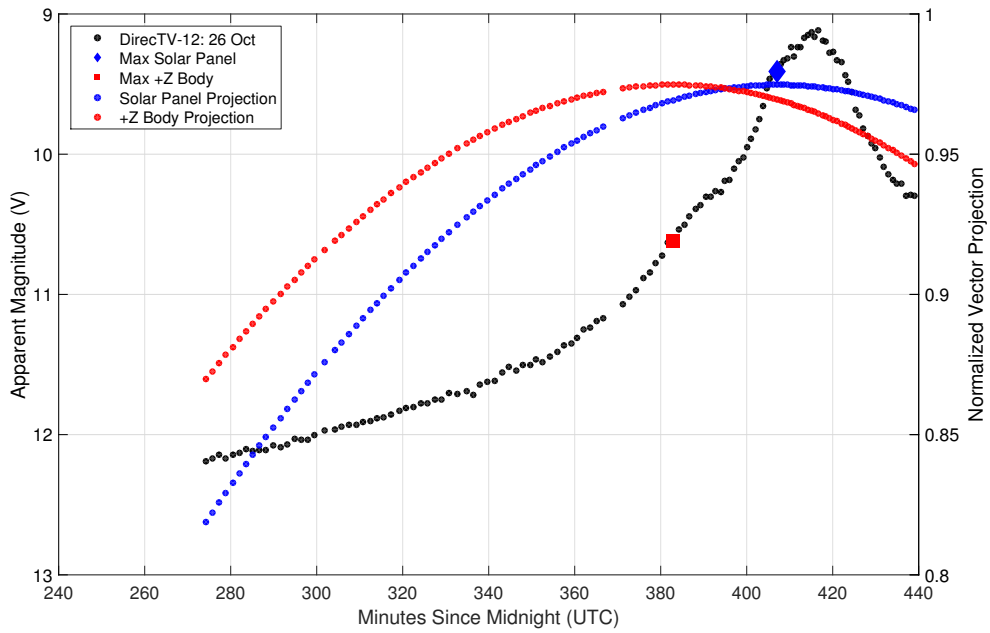
(b) Spaceway-1: 26 Oct 2015

Figure 5.16: Solar panel and +Z body surface vector projections for Spaceway-3 and Spaceway-1 in late October 2015.

5.2. Specular Reflection Analysis



(a) DirecTV-10: 26 Oct 2015



(b) DirecTV-12: 26 Oct 2015

Figure 5.17: Solar panel and +Z body surface vector projections for DirecTV-10 and DirecTV-12 in late October 2015.

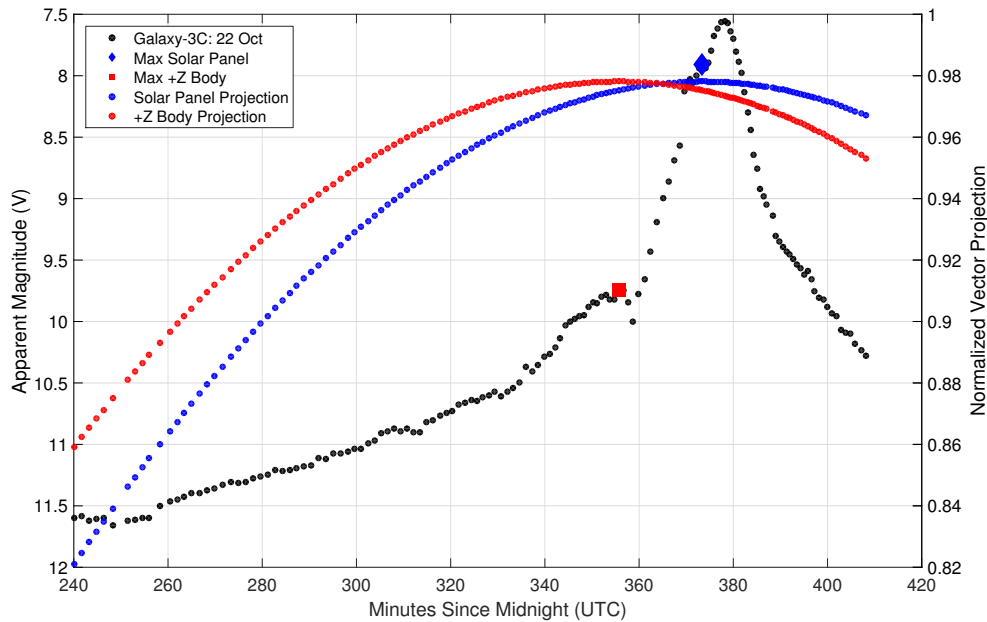


Figure 5.18: Solar array and +Z body surface vector projections for Galaxy-3C in late October 2015.

Late June to early August Vector Projection Results

The vector projection analysis between late June and early August for Spaceway-3 showed that significant light curve features occurred when the +Z body surface vector projection magnitude was at, or near, its maximum value. There were also features, such as the bright peak at 340 MSM on 7 August (Figure 5.12b) that were not associated with the maximum +Z body surface vector projection. No significant features were observed when the solar array vector projection magnitude was at its maximum value. The results for Spaceway-1 during this same period were less conclusive. In early July, none of the significant lightcurve features were associated with either maximum vector projection magnitude. However, on 5 August the brightest peak at 410 MSM (Figure 5.13b) was associated with the maximum +Z body surface vector projection magnitude.

The results for Spaceway-1 and Spaceway-3 suggest that multiple reflective surfaces, with offset angles from the +Z body surface, were responsible for their multi-peak light curve structures. To illustrate this possibility, Figure 5.19 shows a closeup view Spaceway-1 and Spaceway-3's main bus structure.

It is possible that the light curve features that did not occur at the +Z body or solar array vector projection maximum were caused by reflections from the offset antennas or secondary reflections from the thermal reflectors positioned at right angles to the solar arrays.



Figure 5.19: Spaceway-1 and Spaceway-3 main bus structure [11].

The different illumination and observational geometries, caused by their different orbital longitudes, was previously presented as the possible reason for Spaceway-1 and Spaceway-3's different light curve structure. An additional explanation may be that their antennas are not pointing in the same direction. To illustrate this possibility, Figure 5.20 shows the coverage footprints for Spaceway-1 and Spaceway-3 [30]. The key difference between the two satellites' footprints is that Spaceway-1's has spot beams servicing South America. This suggests that antenna elements, for these two satellites, may have offset angles relative to one another which could cause differences in their light curve structures.

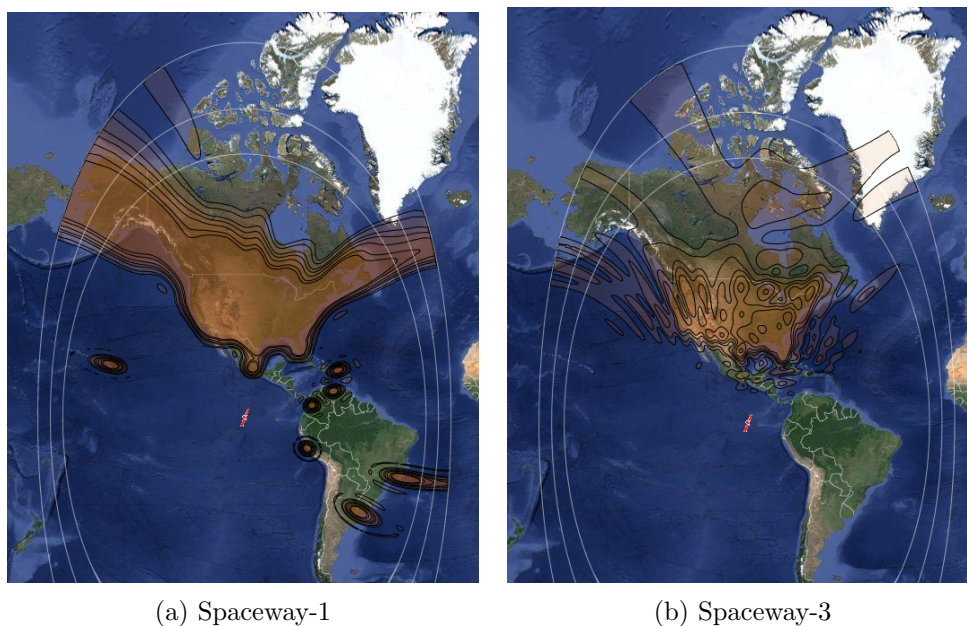


Figure 5.20: Coverage footprints for Spaceway-1 and Spaceway-3 [30].

The single feature observed for Galaxy-3C at 360 MSM during this period was not associated with either maximum vector projection magnitude. A possible explanation is that the particular surface responsible for this feature has an offset angle from the $+Z$ body surface. From Figure 5.21, Galaxy-3C has several large antennas with offset angles from the $+Z$ body surface. It is possible that the single feature is caused by a reflection from these antennas or a secondary reflection from the thermal reflectors.



Figure 5.21: Galaxy-3C main bus structure [11].

Late October Vector Projection Results

The +Z body surface and solar array vector projections in late October suggested that the solar arrays were responsible for the brightest light curve features. Spaceway-3 was the only satellite where the maximum solar array vector projection magnitude was not associated with the brightest light curve features. However, from Figure 5.16a, a sudden increase in brightness at 370 MSM was observed when the maximum solar array vector projection magnitude occurs which suggests that a surface associated with the Sun-tracking solar arrays was responsible this small feature.

In most cases, there was a time offset of several minutes between the maximum solar array vector projection magnitude and the observed maximum brightness. As previous studies have suggested [25], it is possible that these satellites' solar arrays have an offset angle and do not point directly at the Sun. This was possibly the case with DirecTV-10 and DirecTV-12 on 26 October. From Figure 5.17, DirecTV-10's single peak, which was two magnitude

brighter, occurred near the maximum solar array vector projection magnitude while DirecTV-12's peak occurred approximately 10 minutes after the maximum vector projection magnitude.

5.3 Summary of Seasonal Light Curve and Reflection Vector Analysis

The seasonal light curves presented in this chapter showed that GEO satellites having a similar bus do not exhibit the same seasonal variations. However, they do share similar characteristics. For example, Spaceway-1 and Spaceway-3 consistently exhibited a multiple peak structure while DirecTV-10 and DirecTV-12's light curves were featureless prior to October and exhibited a single bright peak afterwards. Galaxy-3C, a third bus variant, exhibited light curve features that were different in structure and magnitude than the Spaceway and DirecTV satellites.

This chapter also used modeled and observational data to determine if the cause of significant light curve features could be constrained to reflections from the solar arrays or +Z body surface. Reflections from surfaces offset from the solar arrays or +Z body surface, such as antennas and thermal reflectors, were not considered. Also, it was assumed that the satellite was in a stable attitude with the surface normal vector from the +Z body surface pointing to the center of the Earth and the solar arrays actively tracking the Sun.

The features associated with the +Z body surface reflections generally occurred between late June and early August. There were instances where a distinct peak was observed, but in most cases, several smaller features were observed when the +Z body surface vector projection magnitude was at, or near, at its maximum. However, there were also instances when significant light curve features were not associated with either the +Z body surface or solar array vector projection maximum. This was observed for Spaceway-1, Spaceway-3, and Galaxy-3C and was attributed to the limitations of the model and the complexity of each of the observed satellites. There was an association between many of the bright light curve features observed in late October and the maximum solar array vector projection. This suggested that these peaks originated from the solar arrays. In many cases, the maximum observed brightness and vector projection magnitude did not occur simultaneously which was attributed a possible offset angle between the solar array surface normal vector and the Sun.

6 Colour Index Variations and Analysis

The objective of this chapter is to determine if multicolour broadband photometry can be used to measure the effects of the space environment on satellite materials. First, time-resolved colour indices are presented for each satellite to show the effects of changing nightly and seasonal illumination geometry. The maximum +Z body surface and solar array vector projections, along with the minimum phase angle, are also included for reference. Next, the colour indices of the features associated with +Z body surface and solar array reflections are compared for different satellites. Comparing the results in this manner ensures that the same types of materials are being compared for multiple satellites.

The seasonal colour indices are presented for each satellite in late June/early July, mid August, and late October. They are presented alongside the light curves to more easily allow identification of any relationship to significant light curve features. As stated, an increasing colour index indicates an increase in the relative intensity of longer wavelengths and a decreasing colour index indicates a increase in the relative intensity of shorter wavelengths. Colour index variations imply a change in the spectral reflectance of the satellite being observed. Figures 6.1 - 6.4 show the seasonal colour indices for Spaceway-3, Spaceway-1, Galaxy-3C, DirecTV-10 and DirecTV-12.

The mean nightly errors associated with each colour index can be seen in Table B.3. In most cases, the errors were smaller than individual colour index data points but, as a reference, the smallest and largest mean errors are presented alongside each plot.

6.1 Seasonal Colour Index Variations

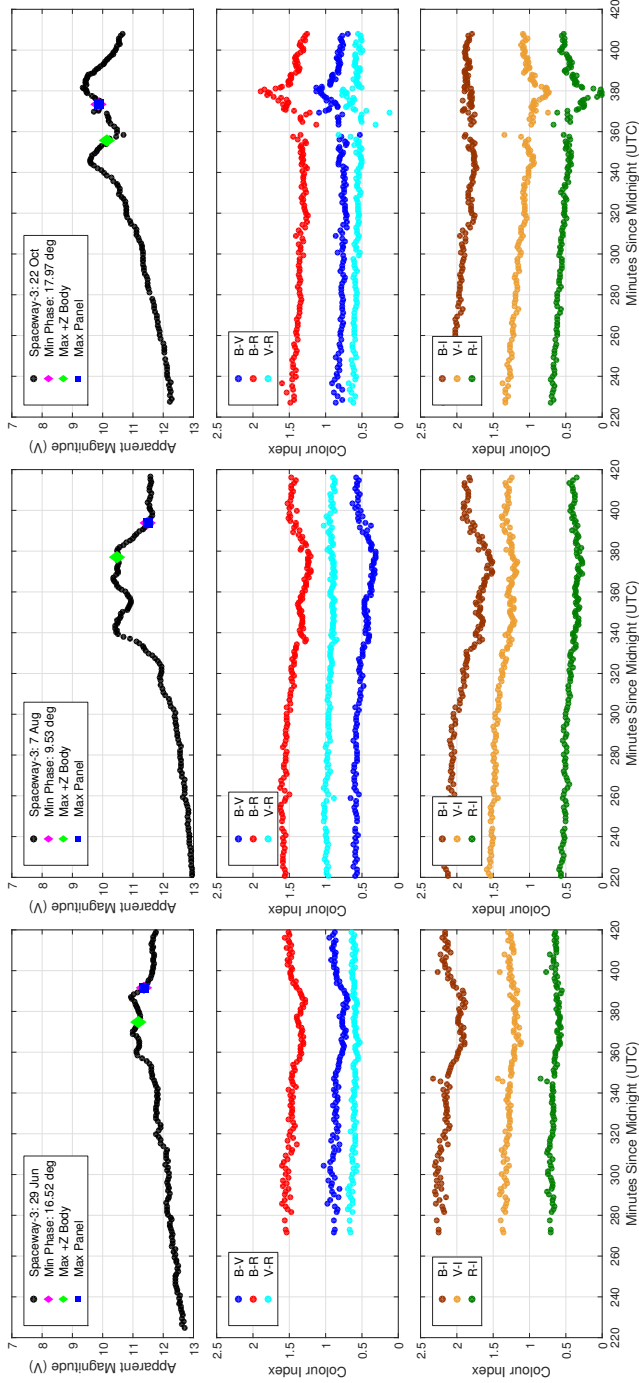
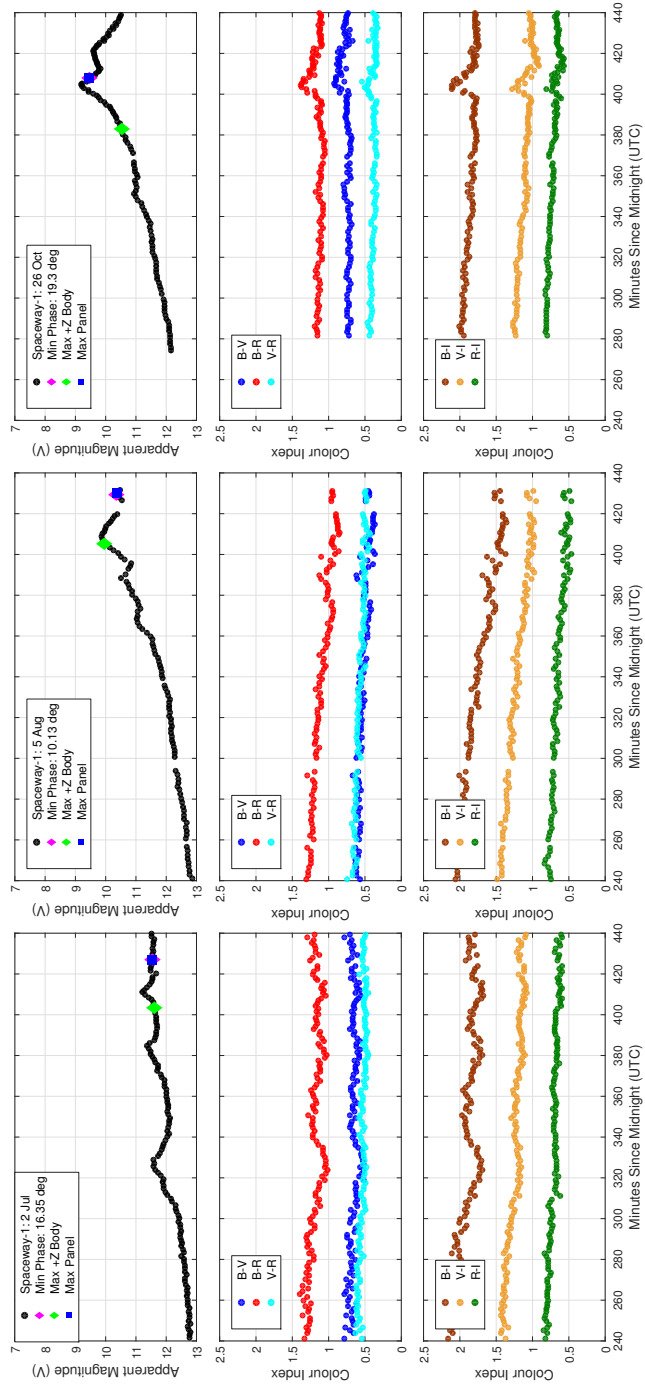


Figure 6.1: Seasonal colour indices for Spaceway-3. Average colour index uncertainties between 0.015 and 0.098.



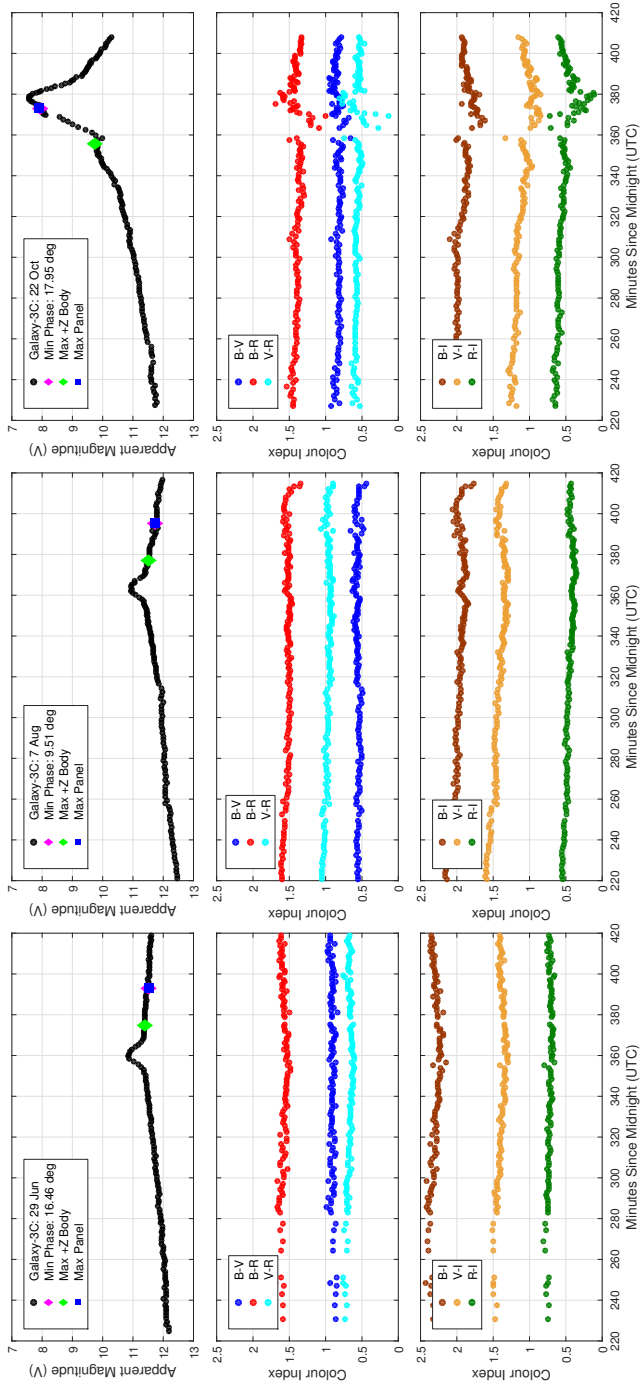
c: 26 October

b: 5 August

a: 2 July

Figure 6.2: Seasonal colour indices for Spaceway-1. Average colour index uncertainties between 0.026 and 0.101.

6.1. Seasonal Colour Index Variations

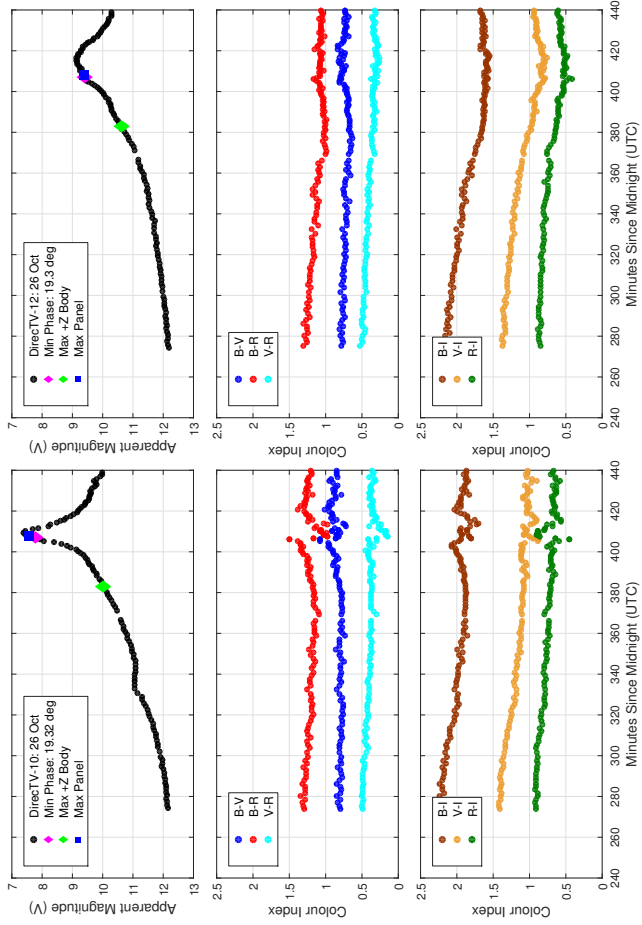


a: 29 June

b: 7 August

c: 22 October

Figure 6-3: Seasonal colour indices for Galaxy-3C. Average colour index uncertainties between 0.015 and 0.098.



a: DirecTV-10: 26 October

b: DirecTV-12: 26 October

Figure 6.4: Colour indices for DirecTV-10 and DirecTV-12 in late October 2015. Average colour index uncertainties between 0.026 and 0.083.

Spaceway-1 and Spaceway-3

On 29 June the three distinct peaks that were observed for Spaceway-3 between 360 - 390 MSM occurred prior to the minimum phase angle and maximum solar array projection. The maximum +Z body projection occurred during the three-peak structure. Overall, the decrease in B-V, B-R, and B-I colour indices between 360 - 390 MSM indicates an increased reflectance at shorter wavelengths. However, at the exact time when maximum +Z body projection occurred the B-V, B-R, and B-I colour indices increased slightly indicating an increased reflectance at longer wavelengths. Three distinct peaks were also observed for Spaceway-1 on 2 July but they occurred over a greater time span. It is important to restate the fact that Spaceway-1 and Spaceway-3 were located at different orbital longitudes, meaning that their illumination geometries were not the same, and they had different coverage footprints. This may explain the different changes in the light curve structure of these two satellites. Spaceway-1's three peaks also occurred prior to the minimum phase angle and maximum solar array projection. The maximum +Z body projection occurred just prior to the brightest peak. Spaceway-1's B-V, B-R, and B-I colour indices also showed an increase in reflectance at shorter wavelengths when the bright peaks were observed. These results suggest that similar materials are responsible for the three peaks observed for both of these satellites.

The overall structure of Spaceway-3's light curve had changed since 29 June with additional features observed between 330 - 390 MSM. The maximum brightness also increased by nearly one magnitude. In August, the Sun was still illuminating the satellites from the northern hemisphere but its elevation had decreased to a point where phase angles of approximately 10° were reached. The result was an increased peak brightness for both satellites. During the significant light curve features, Spaceway-3's colour indices again indicated an increased reflectance at shorter wavelengths. Spaceway-1's overall light curve structure had also changed since early July. Most notably, the bright feature that had occurred at 325 MSM was not observed in August. The maximum brightness of the feature at 410 MSM had also increased by over one magnitude. Unlike early July, an increase in the relative intensity of longer wavelengths was observed during a significant light curve feature. At 390 MSM, the B-V, B-R, and B-I colour indices increased which indicated an increase in reflectance at longer wavelengths. This was the first time increased reflectance at longer wavelengths was observed for either Spaceway-1 or Spaceway-3. Other than this specific occurrence, all colour indices de-

creased gradually.

By late October the Sun's elevation had decreased to an angle where nightly eclipse periods were no longer occurring. The satellites were now being illuminated from the southern hemisphere which created different illumination geometries than had previously been seen and, as a result, specular reflections from the solar arrays were in the direction of the northern hemisphere. Consequently, both Spaceway-1 and Spaceway-3 had significant light curve features associated with their maximum solar array vector projections. Just prior to the brightest feature at 380 MSM Spaceway-3's B-V, B-R, and V-R colour indices increased in relative intensity at longer wavelengths and the V-I and R-I indices increased in relative intensity at shorter wavelengths. This indicated an overall increase in reflectance at mid-band wavelengths just prior to bright feature associated with a solar array reflection at 380 MSM. A similar increase in mid-band reflectance was not observed for Spaceway-1 as all colour indices increased when the bright feature at 405 MSM was observed

Between late June and early August the colour indices indicated that similar materials may be responsible for the significant light curve features. When the features associated with the solar array reflections were observed in October several of the colour indices were not in agreement. It is possible that the satellites' different illumination geometries were responsible for this.

Galaxy-3C

On 29 June the single peak observed at 360 MSM for Galaxy-3C occurred prior to the minimum phase angle and maximum +Z body and solar array projections. The symmetrical shape of the light curve was much simpler than what was observed for Spaceway-1 and Spaceway-3. Also, none of the colour indices showed significant variations during the single peak at 360 MSM, or at any other point during the night. The late June and early August light curves were similar in both structure and brightness. Similar to late June, the single bright peak at 360 MSM occurred approximately 20 minutes prior to the minimum phase angle and Sun elevation.

In late October, the overall light curve structure was similar to what was observed in late June and early August but the peak brightness had increased by three magnitudes. Also, the single bright peak had previously been observed at 360 MSM. On this night, a small feature was observed at 360 MSM and the bright peak occurred at 380 MSM, just after the minimum phase an-

gle. Just prior to the bright peak, the colour indices indicated an increase in mid-band reflectance similar to Spaceway-3.

Galaxy-3C and Spaceway-3 both exhibited similar colour index variations when the bright features associated with a solar array reflection were observed in late October. Also, the fact that they were concurrently observed means that their illumination geometries were very similar making this an ideal scenario to compare colour indices for two satellites.

DirecTV-10 and DirecTV-12

The only continuous observations of DirecTV-10 and DirecTV-12 that showed significant light curve features occurred on 26 October. On this night, DirecTV-10 and DirecTV-12's light curves exhibited a single bright peak. However, DirecTV-10's peak was two magnitude brighter and occurred near the minimum phase angle. DirecTV-12's colour indices generally indicated an increase in reflectance at shorter wavelengths but there was no significant variations during the bright peak. Conversely, DirecTV-10's colour indices varied significantly during its bright peak. Just prior to the peak, an increased reflectance at longer wavelengths was observed and during the peak and increased reflectance at shorter wavelengths was observed.

6.2 Colour Index Analysis during +Z Body and Solar Array Features

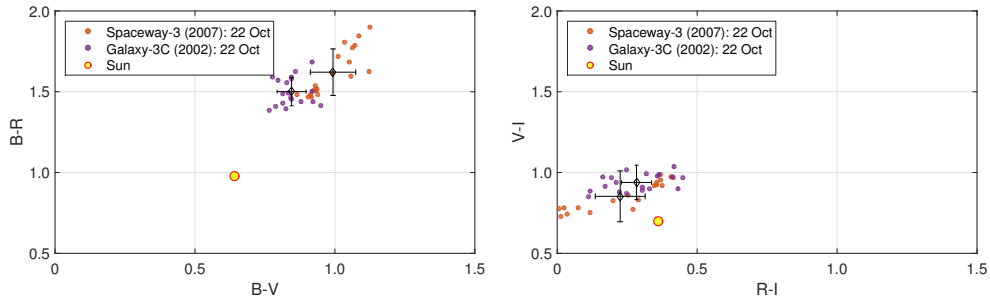
This section compares the colour indices for the observed satellites to determine if the effects of the space environment can be measured with multicolour broadband photometry. The modeled specular reflection analysis from Chapter 5 is used to identify the possible source of significant light curve features. The colour indices from these specific times are compared for multiple satellites with similar buses. The objective is to determine if the effects of the space environment have changed the properties of the satellite's surfaces, such as surface roughness, in such a way that their spectral reflective properties are altered. Colour indices are used to measure these changes.

The colour indices are compared for DirecTV-10, DirecTV-12, and Spaceway-1 during the late October solar array reflections. Spaceway-3 and Galaxy-3C are also compared for this same period. Although they were at different orbital longitudes, Spaceway-1 and Spaceway-3's colour indices are also compared between late June and early July when features associated with the +Z body surface were observed.

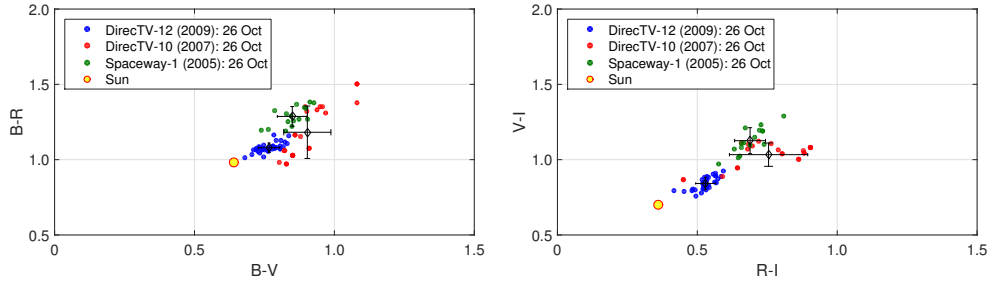
The light curves and colour indices have previously been presented with their average nightly uncertainties. Since smaller samples of data are being presented in this section, the uncertainty associated with each colour index measurement is used to calculate the uncertainty in the mean. Given that the modeled specular reflection vector analysis has been used to identify the light curve features of interest, the colour indices are no longer presented as a function of time. Rather, they are plotted against one another so that results for two different satellites can easily be compared. Figures 6.6 and 6.7 are included to show the regions of the light curves that were considered in this section.

Figures 6.5a and 6.5b show the colour indices for Spaceway-3, Galaxy-3C, DirecTV-10, and DirecTV-12 during the solar array reflection features in late October. These results provide a direct comparison of the colour indices from solar array reflections obtained in similar illumination and observational geometries. Figures 6.5c and 6.5d show the colour indices for Spaceway-1 and Spaceway-3's between late June and early August. The error bars represent the standard deviation of the colour index samples.

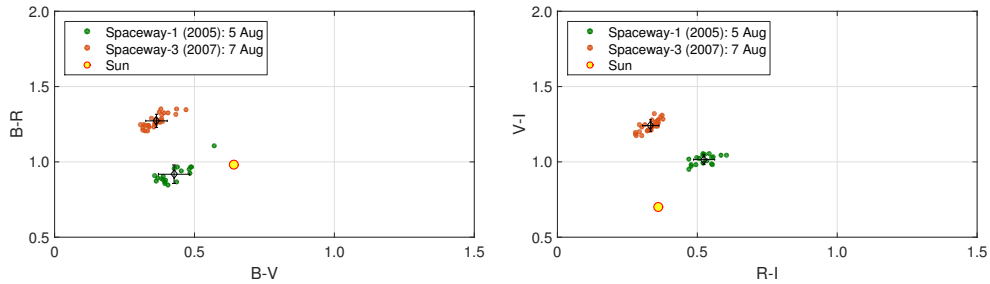
6.2. Colour Index Analysis during +Z Body and Solar Array Features



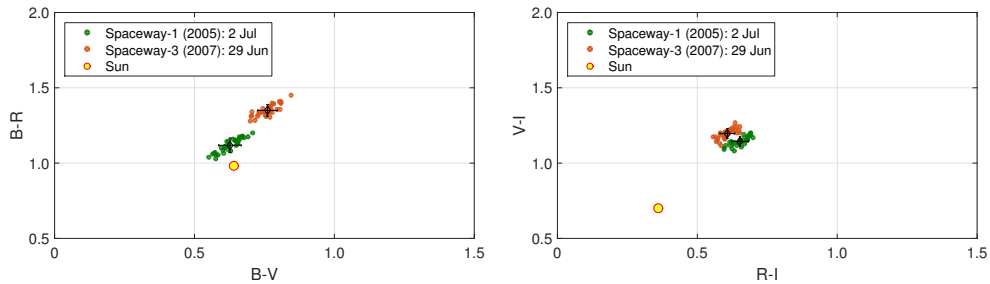
(a) Spaceway-3 and Galaxy-3C solar array colour indices on 22 October. Average colour index errors between 0.019 and 0.040.



(b) DirecTV-10 and DirecTV-12 solar array colour indices on 26 October. Average colour index errors between 0.025 and 0.083.



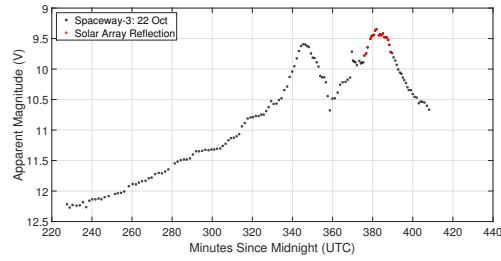
(c) Spaceway-1 and Spaceway-3 +Z body colour indices early August. Average colour index errors between 0.037 and 0.096.



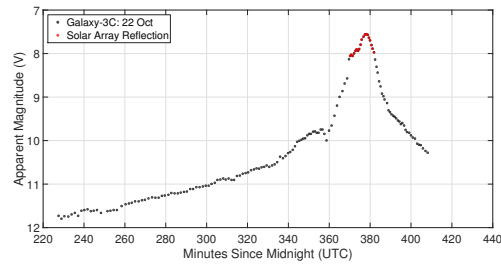
(d) Spaceway-1 and Spaceway-3 +Z body colour indices in late June and early July. Average colour index errors between 0.058 and 0.099.

Figure 6.5: Colour indices +Z body and solar array features.

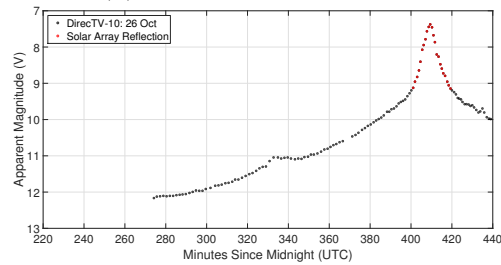
6.2. Colour Index Analysis during +Z Body and Solar Array Features



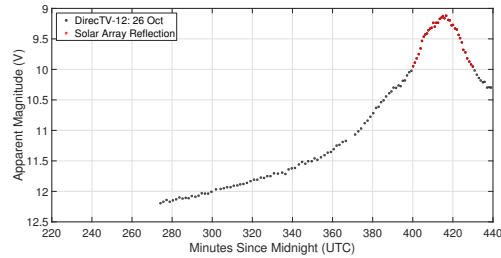
(a) Spaceway-3: 22 October



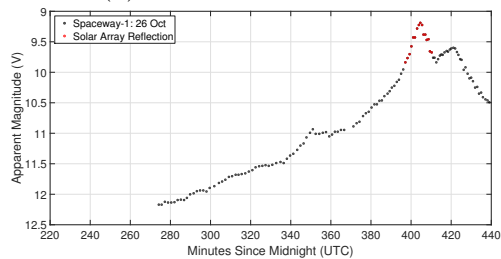
(b) Galaxy-3C: 22 October



(c) DirecTV-10: 26 October



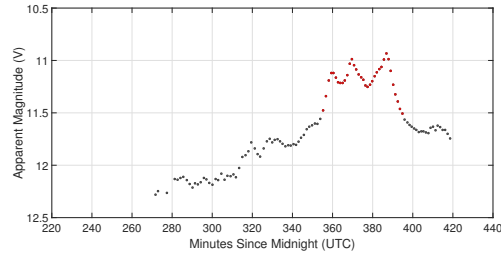
(d) DirecTV-12: 26 October



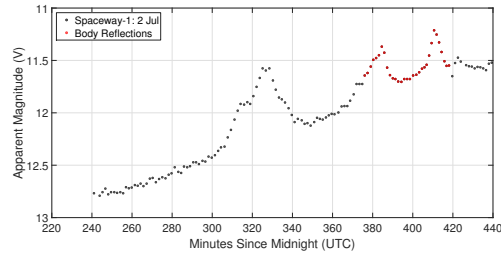
(e) Spaceway-1: 26 October

Figure 6.6: Spaceway-3, Galaxy-3C, Spaceway-1, DirecTV-10, and DirecTV-12's light curves in late-October with solar array reflections indicated.

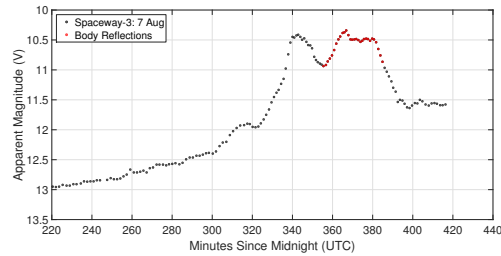
6.2. Colour Index Analysis during +Z Body and Solar Array Features



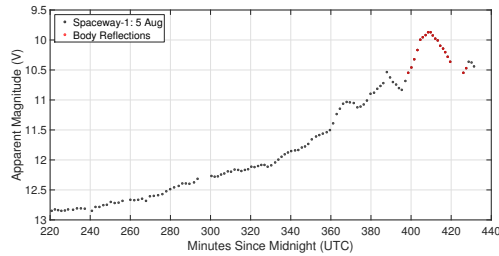
(a) Spaceway-3: 29 June



(b) Spaceway-1: 2 July



(c) Spaceway-3: 7 August



(d) Spaceway-1: 5 August

Figure 6.7: Spaceway-3 and Spaceway-1's light curves between late June and early August with +Z body surface reflections indicated.

The colour indices in Figure 6.5 are shown using color-color plots. They are commonly used in astronomy to show the spectral properties of stars. Here, they are used to provide a comparison of the colour indices which were measured during the periods when reflections from the solar arrays or main body structure were likely occurring. The colour indices of the Sun have been included on each plot to show the relative colour of the observed satellites' features.

Solar array colour indices

Several consistent trends were observed for the colour indices measured during the solar array reflections in late October. In all cases, the mean value of the V-I colour index was larger for the older satellites in the observed cluster. However, the colour indices of Spaceway-3, Galaxy-3C, and DirecTV-10 had a large variance when the brightest solar array reflections were observed. This uncertainty makes it difficult to assert that a definitive relationship between observed colour indices and relative age exists. If only DirecTV-12 and Spaceway-1 are considered within their cluster then the results are more conclusive. In all colour indices, the older satellite (Spaceway-1) showed a greater reflectivity at longer wavelengths.

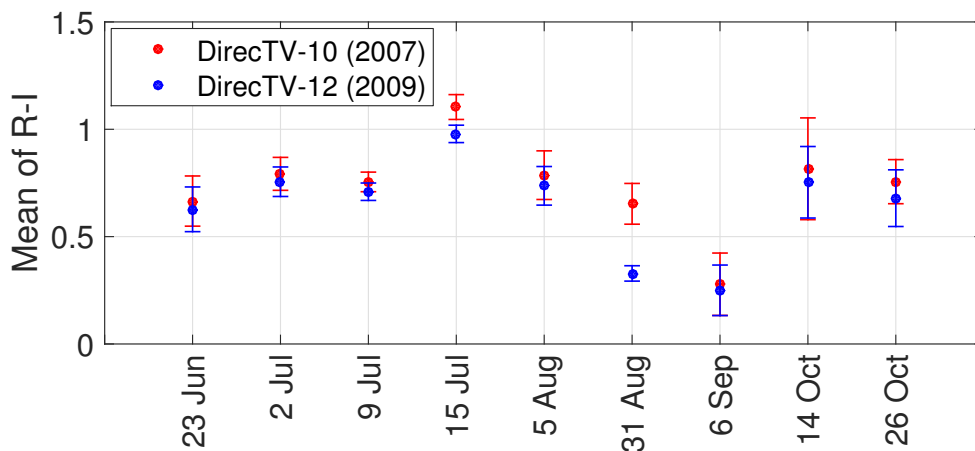
+Z body surface colour indices

Between late June and early August the colour indices showed less variance and, again, several trends were observed. In all cases, the older of the two satellites had smaller mean values for the B-R and V-I colour indices and larger mean values for the R-I colour index when features associated with the +Z body surface were being observed. The increase in I-band reflectance, in the R-I colour index, was also observed in late October.

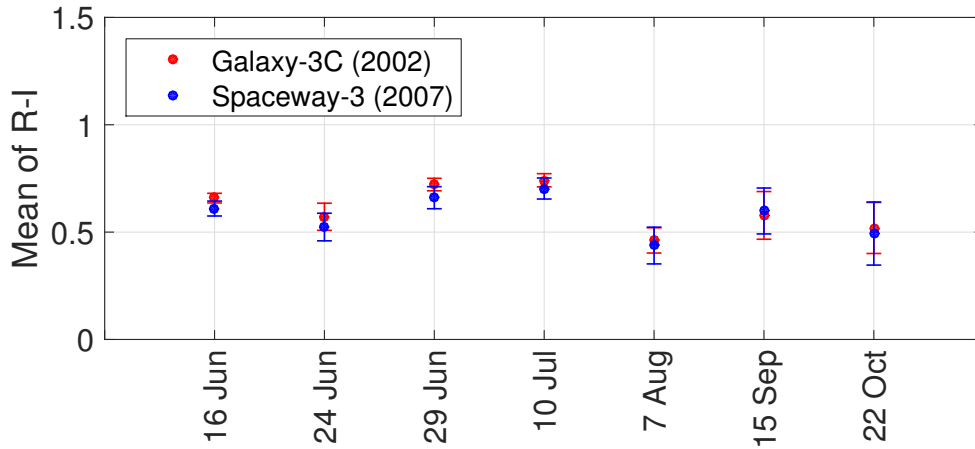
The limited results presented here showed that older satellites may have an increased reflectance at longer wavelengths in the R-I colour index. These results are in agreement with the observed relationship between increased surface roughness, caused by space weathering, and the increase in the spectral slope as previously shown by Bédard *et al.* in Figure 2.2 [19].

6.2. Colour Index Analysis during +Z Body and Solar Array Features

Because the R-I colour index of the older satellites was consistently larger for both the +Z body and solar array features, this analysis will consider data from the entire observation campaign. Rather than focusing on specific regions of the light curves, a mean value for the R-I colour index is calculated from all measurements on a given night. Figure 6.8 shows the mean values for the R-I colour index for Spaceway-3, Galaxy-3C, DirecTV-10, and DirecTV-12. The standard deviation of the nightly population of R-I colour index values is represented by the error bars.



(a) DirecTV-10 and DirecTV-12.



(b) Spaceway-3 and Galaxy-3C.

Figure 6.8: Mean values of the seasonal R-I colour indices for DirecTV-10, DirecTV-12, Spaceway-3, and Galaxy-3C.

For both comparisons, the mean R-I colour index value was larger for the older of the two satellites. The exception was 15 September when Spaceway-3's mean R-I colour index value was larger. On this night, the the satellites were eclipsed before any significant features were observed for Galaxy-3C. A consequence of analyzing the entire nightly colour index population is the larger standard deviation. In most cases, each satellite's mean R-I colour index falls within the standard deviation of the other satellite. However, the fact that mean value of the older satellite's R-I colour index is consistently larger is evident from this analysis. These results, again, agree with the laboratory results presented by Bédard *et al.* where an increased spectral slope at longer wavelengths was observed for rougher materials [19].

Based on these limited results, it is not possible to assert that multicolour broadband photometry can be used to repeatedly and definitively measure the effects of the space environment on satellite materials. However, the results presented here do illustrate that there is a trend in which older satellites have relative reflectance at longer wavelengths, specifically in the R-I colour index. Further work is required to verify the repeatability of these results.

6.3 Summary of Colour Index Results

This chapter initially examined the seasonal colour indices of all the observed satellites. It was found that the colour indices varied the most during the periods when significant light curve features were observed. Between late June and early August these variations indicated an increased reflectance at shorter wavelengths. However, there was an isolated incident where a specific feature indicated an increased reflectance at longer wavelengths. In late October, the colour indices of most satellites showed greater variation during the bright peaks. There was a notable change as the variations in the colour indices indicated an increased reflectance at longer wavelengths. Along with the specular reflection analysis provided in Chapter 5, these results indicated that different reflecting materials were likely responsible for the light curve features in October.

The main objective of this chapter was to determine if the effects of the space environment on satellite materials can be observed using multicolour broadband photometry. Initially, an analysis of the colour indices from the periods when the +Z body surface and solar array reflections were observed was provided. This helped ensure that the colour indices from similar satel-

lite materials were being compared. Between late June and early July, the results showed that the older satellites had an increased reflectance at shorter wavelengths in the B-R and V-I colour indices and an increase in reflectance at longer wavelengths in the R-I colour index. In late October it was observed that the older satellites had an increased reflectance at longer wavelengths in the V-I and R-I colour indices. Thus, the older satellites always showed an increased reflectivity at longer wavelengths, specifically in the I-band relative to the R-band.

An analysis of the entire nightly populations of the R-I colour index measurements was then carried out because previous analysis showed that this increased reflectivity in the I-band, relative to the R-band, was observed for both the +Z body and solar array reflections. The R-I colour index values for two sets of satellites were compared for the entire observation campaign. In nearly all cases, the older satellite's mean R-I colour index was larger. Combined, these results showed that, while there is a trend between the relative age of satellites and reflectance at longer wavelengths, further work is required to verify these results.

7 Conclusion

The work that has been presented focused on characterization of active GEO satellites using multicolour broadband photometry. Five active GEO satellites, each with a variant of the Boeing 702-HP bus, were observed on most photometric nights between late June and late October 2015. Their relative orbital positions allowed satellites with identical bus variants, but different launch dates, to be concurrently observed. These five satellites were located in two separate clusters that were observed on a rotating schedule. Spaceway-3 (2007) and Galaxy-3C (2002) were in the first cluster and DirecTV-10 (2007), DirecTV-12 (2009), and Spaceway-1 (2005) were in the second.

The experimental setup consisted of a 0.3 m telescope and a CCD camera with integrated Johnson-Cousins photometric filters. All data were processed to remove the instrumental signature and extract the magnitude of the satellites from the raw images. Each night, images of Landolt photometric standard stars were taken for calibration purposes. As a final step, colour indices were created from the calibrated apparent magnitudes. The variance in the nightly zeropoints and photometric errors were the primary sources of uncertainty in each measurement.

Light curves and colour indices were produced from the time-resolved magnitudes and flux ratios of each observed satellite. The observed brightness of the satellites was directly related to the illumination and observation geometries. Finally, it was concluded that the peak brightness, light curve structure, and colour indices all showed a seasonal dependence.

The remainder of this chapter summarizes the key results from this thesis and presents recommendations for future work.

7.1 Summary of Conclusions

7.1.1 Seasonal Light Curve Variations of Identical Satellites

The initial objective was to determine if similar GEO satellites exhibit the same seasonal light curve variations. To address this question, active GEO satellites with similar, or identical, bus variants were concurrently observed multiple times between late June and late October 2015. Between late June and early July, Spaceway-1 and Spaceway-3, both of which had identical variants of the Boeing 702-HP bus, exhibited light curve structures with multiple bright features. Spaceway-3's features were one half magnitude brighter and occurred within a shorter time span. After autumnal equinox, in late October, each satellite exhibited two distinct bright features that were similar in brightness but had a different overall structure. The difference in Spaceway-1 and Spaceway-3's orbital longitude created different illumination and observation geometries which may have contributed to the difference in their light curve structures.

DirecTV-10 and DirecTV-12 also had an identical variant of the Boeing 702-HP bus but, unlike the Spaceway satellites, concurrent observations were possible because they were in the same cluster. Prior to October, both satellites exhibited a featureless light curve that gradually increased in brightness during a night of observations. In late October, there was a significant change as DirecTV-10 and DirecTV-12's light curves both exhibited a single bright peak. Despite the fact that these identical satellites were co-located, DirecTV-10's peak was nearly two magnitude brighter and was more defined at its brightest point.

Galaxy-3C, built on a third variant of the Boeing 702-HP bus, was concurrently observed multiple times with Spaceway-3. Its light curve exhibited features that were different in structure and magnitude than those observed for the DirecTV and Spaceway satellites. An assumption made during this analysis was that all satellites maintained the same attitude with their solar arrays actively tracking the Sun but it is possible that one of the satellites' solar arrays were positioned at an angle slightly offset from the Sun. This may explain the difference in magnitude and light curve structure observed for the DirecTV satellites. The differences in light curve structure and magnitude observed during seasonal observations indicated that active GEO satellites, with similar bus configurations, do not exhibit the same seasonal light curve variations. However, each variant exhibited similar broad charac-

teristics. These similar broad characteristics gave confidence that comparing photometric measurements of similar satellites was a valid approach to determining if the effects of the space environment on satellite materials could be measured with multicolour broadband photometry.

7.1.2 Identification of Specular Reflections

An effort was also made to determine which satellite surfaces were responsible for the significant light curve features observed throughout the observation campaign. After the initial analysis, it was evident that the light curve variations showed a seasonal dependence. Most notably, the increase in brightness in late October suggested that a different reflecting surface was responsible for the observed light curve features. By late October, the Sun was illuminating the observed satellites from the southern hemisphere which meant that the specular reflections were in the direction of the northern hemisphere. Prior to autumnal equinox in mid September, the Sun was in the northern hemisphere and the reflections were in the directions of the southern hemisphere.

For this analysis, a specular reflection vector was modeled for the +Z body (nadir facing) and the Sun-tracking solar arrays. Each reflection vector was projected onto the observer position vector and the magnitude of those vector projections were plotted alongside the light curves. The maximum nightly value of each vector projection indicated the most ideal time for a specular reflection from either the +Z body surface or the Sun-tracking solar arrays to be observed.

Many of the significant light curve features observed between late June and early August occurred when the magnitude of the +Z body surface vector projection was at, or near, its nightly maximum. No light curve features were associated with the maximum solar array vector projection. Spaceway-1 and Spaceway-3's light curves both had multiple features near the maximum +Z body surface vector projection but, in several cases, features were observed that were not associated with either the +Z body or solar array vector projection. These results suggested that reflective surfaces with offset angles from the +Z body surface were responsible for the significant features.

In late October, the magnitude of the solar array vector projection was at its maximum when several of the bright features were observed. In most cases, no features were observed when the +Z body vector projection was at its maximum. This strongly suggested that the solar arrays were responsible

for the brightest observed features which occurred in late October. It was noted that there was usually an offset between the peak observed brightness and the maximum solar array vector projection. This was attributed to a solar array offset angle.

The primary limitation of this analysis is that only the +Z body surface and solar array specular reflection vectors were modeled. The satellite diagrams presented here showed that each bus structure has several antenna elements and reflectors positioned with offset angle from the body. Surfaces such as these may be the source of the significant peaks that were not associated with the maximum magnitude of either vector projection. Nevertheless, these results indicated that it is possible to constrain the physical origin of many of the features to the body structure or solar arrays. These results gave further confidence that measurements from multiple satellites can be compared.

7.1.3 Measuring the Effects of the Space Environment with Broadband Photometry

The primary aim of this thesis was to determine if multicolour broadband photometry could measure the effects of the space environment on satellite materials. Previous work has focused on inactive unstabilized satellites which introduced several unknown parameters, such as their attitude and rotational rates [23]. These unknown parameters made it difficult, if not impossible, to determine which surface, or combination of materials, was being observed at a given time. Hence, active GEO satellites were better suited to conduct an experiment that attempts to achieve the aim of this thesis.

Initially, the seasonal time-resolved colour indices were presented alongside the light curves. From these results, it was found that the colour indices varied when most of the significant light curve features were observed. Between late June and early August, most colour indices indicated an increased reflectivity at shorter wavelengths when significant light curve features associated with the +Z body surface were observed. In late October an increased reflectivity at mid-band and longer wavelengths was observed during the bright light curve features. These results suggested that different satellite materials were responsible for the changing light curve features.

The measured colour indices and modeled specular reflection analysis were used in conjunction to determine if the changes in reflectance could be measured. Comparing the colour indices from the +Z body surface and solar array

reflections gave confidence that similar materials, for different satellites, were being compared.

First, the colour indices for the +Z body surface reflections between late June and early July were compared for the two groups of satellites. The same approach was taken with the solar array reflections in late October. In nearly all cases the mean value of R-I colour index was larger for the older satellites. This indicated that older satellites had an increased reflectivity in the I-band, relative to the R-band, for the features associated with both the +Z body surface and solar array reflections. However, the colour indices from late October had a large variance which reduced the confidence in these results.

The first approach was limited to times when +Z body surface and solar array reflections were occurring. Since the R-I colour index was consistently larger for older satellites, a broader data set was considered. The mean values from the entire nightly populations of the R-I colour index measurements were compared for the entire observation campaign. Concurrently observed satellites were compared in this manner. In nearly all cases, the mean of the R-I colour index measurements was larger for the older of the two satellites. However, these measurements were almost always within the uncertainty. This, again, suggested that the older satellite had an increased reflectivity in the I-band, relative to the R-band. These results were in agreement with those obtained during laboratory experiments where material samples with increased surface roughness had an increased spectral slope at longer wavelengths. To conclude, the limited results presented here suggested that it is possible to measure the effects of the space environment on satellite materials using multicolour broadband photometry.

7.2 Recommendations for Future Work

Each observed satellite exhibited a distinct light curve structure that was influenced by its bus configuration and the illumination and observational geometries. The time constraints of this thesis limited satellite observations to a single season, between late June and late October in this case. During this period, the illumination geometry was such that the Sun was illuminating the observed satellites from the northern hemisphere and gradually decreasing in elevation. It would be of benefit to observe the same satellites during other seasons to fully characterize the effects of changing seasonal illumination and

observational geometries. In addition, observing the same satellites on similar dates would verify the repeatability of the observed light curves and colour indices.

The modeled specular reflection analysis presented in this thesis showed that it is possible to constrain the physical origin of many of the observed light curve features. However, this analysis was limited to the +Z body surface and solar arrays. There were several instances where significant light curve features were not associated with either of these modeled reflections. Modeling satellite-specific components, such as antenna arrays and reflectors, could explain the source of the additional light curve features. Alternatively, this technique could possibly be used to infer characteristics of an unknown satellite from its observed light curve.

The limited results obtained during this thesis indicated that there is a relationship between the relative age of similar satellites and an increased reflectance at longer wavelengths in the R-I colour index. At this point, it is not possible to conclude that this is true in all cases. Future work should focus on verifying these results with additional observations. Specifically, satellites with a wider range of relative ages should be observed to determine the rate of increase in reflectance at longer wavelengths as they are exposed to the space environment. From an SSA perspective, measuring the effects of the space environment on satellite materials has little practical utility if it is constrained to satellites with a similar bus type. Thus, future work should also focus on expanding this technique to satellites with different bus types and configurations.

Bibliography

- [1] JFCC Space. Satellite situation report. <https://www.space-track.org>, March 2016.
- [2] P.B. de Selding. Galaxy 15, still adrift, poses threat to its orbital neighbors. <http://spacenews.com/galaxy-15-still-adrift-poses-threat-its-orbital-neighbors/>, April 2010.
- [3] D. Hall and P. Kervin. Analysis of faint glints from stabilized geo satellites. In *Proceedings of the 2013 AMOS Technical Conference*, 2013.
- [4] F.R. Chromey. *To Measure the Sky: An Introduction to Observational Astronomy*. Cambridge University Press, 2010.
- [5] W. Romanishin. An introduction to astronomical photometry using ccds. http://www.physics.csbsju.edu/370/photometry/manuals/OU.edu_CCD_photometry_wrccd06.pdf, February 2016.
- [6] H. Cowardin, P. Seitzer, K. Abercromby, E. Barker, B. Buckalew, T. Cardona, P. Krisko, and S. Lederer. Observations of titan iic transtage fragmentation debris. In *Proceedings of the 2014 AMOS Technical Conference*, 2014.
- [7] W. H. Ryan and E. V. Ryan. Photometric studies of rapidly spinning decommissioned geo satellites. In *Proceedings of the 2015 AMOS Technical Conference*, 2015.
- [8] R. Jolley, A. Multicolour optical photometry of active geostationary satellites using a small aperture telescope. Master's thesis, Royal Military College of Canada, 2014.
- [9] D. Hastings and H. Garrett. *Spacecraft-Environment Interactions*. Cambridge University Press, 2004.
- [10] W.J. Larson and J.R. Wertz, editors. *Space Mission Analysis and Design*. Microsim Press, 2005.
- [11] Boeing. Defense, space and security. http://www.boeing.com/defense-space/space/bss/programs_702.html#702HP, 10 September 2015.

-
- [12] D. Bedard, G.A. Wade, D. Monin, and R. Scott. Spectrometric characterization of geostationary satellites. In *Proceedings of the 2012 AMOS Technical Conference*, 2012.
- [13] F.E. Nicodemus, J.C. Richmond, and J.J. Hsia. Geometrical considerations and nomenclature for reflectance. Technical report, Institute for Basic Standards, National Bureau of Standards, 1977.
- [14] H.L. Johnson and W.W. Morgan. Fundamental stellar photometry for standards of spectral type on the revised system of the yerkes spectral atlas. *The Astrophysical Journal*, 117:313–352, 1953.
- [15] M.S. Bessell. Standard photometric systems. *Annual Review of Astronomy and Astrophysics*, 43:293–336, 2005.
- [16] M.M. Finckenor and K.K. de Groh. A researcher’s guide to: International space station space environmental effects. Technical report, NASA, 2015.
- [17] D.R. Wilkes and J.M. Zwiener. Science data report for the optical properties monitor (opm) experiment. Technical report, NASA, 2001.
- [18] D.M. Harland and R.D. Lorenz. *Space Systems Failures*. Springer, 2005.
- [19] D. Bedard, G.A. Wade, and K. Abercromby. Laboratory characterization of homogenous spacecraft materials. *Journal of Spacecraft and Rockets*, 52:1038–1056, 2015.
- [20] J. Frith, P. Anz-Meador, B. Cowardin, H. Buckalew, and S. Lederer. Near-infrared color vs. launch date: an analysis of 20 years of space weathering effects on the boeing 376 spacecraft. In *Proceedings of the 2015 AMOS Technical Conference*, 2015.
- [21] H. Cowardin, P. Seitzer, K. Abercromby, E. Barker, and T. Schildknecht. Characterization of orbital debris photometric properties derived from laboratory-based measurements. In *Proceedings of the 2010 AMOS Technical Conference*, 2010.
- [22] H. Cowardin, K. Abercromby, E. Barker, P. Seitzer, M. Mulrooney, and T. Schildknecht. An assessment of geo orbital debris photometric properties derived from laboratory-based measurements. In *Proceedings of the 2009 AMOS Technical Conference*, 2009.
- [23] S.M. Lederer, P. Seitzer, H.M. Cowardin, E.S. Barker, K.J. Abercromby, and A. Burkhardt. Preliminary characterization of idcsp spacecrafts through a multi-analytical approach. In *Proceedings of the 2012 AMOS Technical Conference*, 2012.
- [24] D. Bedard. *Spectrometric Characterization of Artificial Earth-Orbiting Objects*. PhD thesis, Royal Military College of Canada, 2013.
- [25] T.E. Payne, S.A. Gregory, and K. Luu. Ssa analysis of geos photometric signature classifications and solar panel offsets. In *Proceedings of the 2006 AMOS Technical Conference*, 2006.

- [26] Joint Functional Component Command Space/J3. Space-track. <https://www.space-track.org>.
- [27] Quantum Scientific Imaging. *QSI 500/600 Series User Guide*, revision 3.1 edition, January 2014.
- [28] S.B. Howell. *Handbook of CCD Astronomy*. Cambridge University Press, 2006.
- [29] U. Landolt, A. Ubvri photometric standard stars around the celestial equator. *The Astronomical Journal*, 88:439–460, 1983.
- [30] Satbeams SPRL. <http://www.satbeams.com>, April 2016.

Appendices

A Standard Stars

Star	Vmag	RA(h:m:s)	Dec(deg:m:s)	Dates Used
SA 111-773	8.963	19:37:16	+00:10:58	16 June 23 June
SA 110-441	11.124	18:43:34	+00:19:41	16 June 23 June 24 June
SA 106-700	9.787	14:40:51	-00:23:37	24 June 29 June 2 July 9 July
HD 129975	8.373	14:45:38	-00:21:53	10 July 24 June 10 July 15 July
HIP 66872	10.367	13:42:19	+01:30:19	29 June 2 July
SA 112-595	11.349	20:41:18	+00:16:28	29 June
SA 112-704	11.452	20:42:02	+00:19:08	29 June
SA 112-250	12.095	20:42:26	+00:07:42	29 June
SA 105-815	11.451	13:40:02	-00:02:19	2 July 9 July
GSC 4976:391	13.758	14:10:26	+01:30:17	2 July 9 July
SA 105-505	10.270	13:35:25	+00:23:21	2 July
HD 175544	7.395	18:55:47	+00:15:55	9 July
SA 106-485	9.484	14:44:14	+00:37:07	9 July

Star	Vmag	RA(h:m:s)	Dec(deg:m:s)	Dates Used
SA 106-834	9.088	14:39:28	+00:14:56	10 July 15 July
SA 106-1250	8.123	14:41:27	+00:06:13	10 July
SA 108-1332	9.199	16:35:21	+00:04:05	5 August 7 August
HD 149382	8.944	16:34:23	-04:04:52	5 August
SA 108-1491	9.026	16:37:14	+00:02:42	5 August
SA 108-1911	8.050	16:37:46	+00:02:25	7 August
HD 170493	8.037	18:29:52	-01:49:05	30 August 6 September
SA 110-471	7.474	18:41:27	+00:33:52	30 August 6 September
HD 173637	9.375	18:46:38	-07:55:55	30 August
HD 160233	9.095	17:38:41	+04:20:10	31 August
GSC 424:1716	9.326	17:47:33	+04:50:21	31 August
HIP 87946	9.553	17:57:57	+04:14:52	31 August
HD 184914	8.170	19:36:45	-04:17:59	3 September 15 September
SA 114-272	7.737	22:42:58	+00:24:07	3 September
HD 175544	7.395	18:55:47	+00:15:55	6 September
SA 111-717	8.529	19:36:55	+00:07:32	15 September
HD 188934	9.351	19:57:38	+00:14:30	15 September
HD 5505	9.001	00:56:51	+01:40:51	14 October
HD 209796	8.933	22:06:01	+01:22:48	22 October 26 October

B Uncertainty

Date	B		V		Rc		Ic	
	\overline{SNR}	$\overline{\sigma_{phot}}$	\overline{SNR}	$\overline{\sigma_{phot}}$	\overline{SNR}	$\overline{\sigma_{phot}}$	\overline{SNR}	$\overline{\sigma_{phot}}$
29 Jun	230	0.042	258	0.060	275	0.048	206	0.033
	± 44	± 0.001	± 48	± 0.001	± 35	± 0.001	± 27	± 0.001
2 Jul	197	0.080	247	0.032	272	0.061	225	0.022
	± 39	± 0.001	± 52	± 0.001	± 47	± 0.001	± 29	± 0.001
5 Aug	203	0.033	265	0.055	299	0.055	258	0.045
	± 58	± 0.002	± 65	± 0.001	± 59	± 0.001	± 51	± 0.001
7 Aug	281	0.034	323	0.017	357	0.048	312	0.085
	± 95	± 0.002	± 69	± 0.001	± 75	± 0.001	± 85	± 0.001
22 Oct	329	0.009	323	0.015	347	0.036	305	0.012
	± 112	± 0.002	± 79	± 0.001	± 82	± 0.001	± 82	± 0.001
26 Oct	492	0.072	479	0.042	507	0.021	420	0.015
	± 266	± 0.003	± 182	± 0.001	± 176	± 0.001	± 164	± 0.002

Table B.1: Average SNR and photometric uncertainty.

Date	B		V		Rc		Ic	
	<i>zmag</i>	σ_{zmag}	<i>zmag</i>	σ_{zmag}	<i>zmag</i>	σ_{zmag}	<i>zmag</i>	σ_{zmag}
29 Jun	22.311	0.038	22.541	0.056	22.300	0.044	20.612	0.028
2 Jul	22.281	0.074	22.595	0.028	22.391	0.057	20.689	0.017
5 Aug	22.158	0.028	22.570	0.051	22.283	0.051	20.567	0.041
7 Aug	22.581	0.030	23.068	0.014	22.438	0.045	20.895	0.081
22 Oct	22.494	0.006	22.735	0.012	22.419	0.012	20.717	0.008
26 Oct	22.433	0.070	22.724	0.040	22.588	0.019	20.715	0.012

Table B.2: Nightly zero points and uncertainty.

Date	$\overline{\sigma_{B-V}}$	$\overline{\sigma_{B-R}}$	$\overline{\sigma_{B-I}}$	$\overline{\sigma_{V-R}}$	$\overline{\sigma_{V-I}}$	$\overline{\sigma_{R-I}}$
29 June 2015	0.073	0.064	0.053	0.077	0.068	0.058
2 July 2015	0.086	0.101	0.083	0.069	0.039	0.065
5 August 2015	0.064	0.064	0.056	0.078	0.071	0.071
7 August 2015	0.038	0.059	0.092	0.051	0.087	0.098
22 October 2015	0.017	0.037	0.015	0.039	0.019	0.038
26 October 2015	0.083	0.075	0.074	0.047	0.045	0.026

Table B.3: Average colour index uncertainties.

C Curriculum Vitae

Name:	Jason Shaw	
Place of birth:	Sault Ste. Marie, Ontario	
Year of birth:	1981	
Post-secondary education and degrees:	MSc. Candidate Royal Military College of Canada Kingston, Ontario	2014-2016
	BSc., Physics and Space Science Royal Military College of Canada Kingston, Ontario	2014
	Diploma of Technology, Electrical and Engineering Technology Cambrian College Sudbury, Ontario	2002
Employment: history:	Detachment Commander 2 Canadian Mechanized Brigade Group Headquarters and Signals Squadron Petawawa, Ontario	2008-2010
	Communications Technician 2 Service Battalion Petawawa, Ontario	2006-2008
	Communications Technician 2 General Support Battalion Petawawa, Ontario	2002-2006

Honours and awards:	Fourth Year Space Science Program Award Royal Military College of Canada	2014
	Third Year Award for Academic Excellence Royal Military College of Canada	2013
	Third Year Space Science Program Award Royal Military College of Canada	2013
	Second Year Space Science Program Award Royal Military College of Canada	2012